UNIVERSIDAD DE CANTABRIA

ESCUELA DE DOCTORADO DE LA UNIVERSIDAD DE CANTABRIA
DOCTORADO EN INGENIERÍA QUÍMICA, DE LA ENERGÍA Y DE PROCESOS

Numerical modeling of chemical reaction processes describing methane combustion in gas cooking burners

Modelado numérico de los procesos de reacción química que describen la combustión del metano en quemadores de cocción a gas

Memoria de Tesis Doctoral presentada para optar al título de Doctor por la Universidad de Cantabria

Presentada por:

Saúl Laguillo Revuelta

Dirigida por:

Dr. Alfredo Ortiz Sainz de Aja
Dr. José Salvador Ochoa Torres

Santander, 2020

Dedicado a
mi padre.

Programa de Doctorado en Ingeniería Química, de la Energía y de Procesos
(BOE núm. 16, de 19 de enero de 2015. RUCT: 5601000)

Agradecimientos

Me gustaría dedicar unas líneas para expresar mi agradecimiento a todas esas personas que han hecho posible el desarrollo y finalización de esta tesis doctoral.

En primer lugar, me gustaría agradecer a mis directores de tesis, Alfredo Ortiz y Salvador Ochoa, por haberme dado la oportunidad de desarrollar mi labor investigadora y haberme enseñado todo lo que he aprendido durante estos años.

Asimismo, agradecer a todos los miembros del departamento de Gas Technology de BSH Santander, donde he podido llevar a cabo la práctica totalidad de esta investigación. Un agradecimiento especial para Salva, Cristina y Adriana, mis compañeros en el equipo de simulación, quienes me han ayudado enormemente en el desarrollo de la tesis.

También quiero agradecer a Norberto Fueyo y al resto de miembros del Grupo de Fluidodinámica Numérica de la Universidad de Zaragoza, donde pude realizar una estancia predoctoral durante siete meses en los que amplié extraordinariamente mis conocimientos. En especial, a Eduardo y a Ramón, quienes me hicieron sentir como en casa.

Me gustaría agradecer también a las empresas Apria Systems, S.L. y BSH Electrodomésticos España, S.A. por la confianza que han depositado en mí, permitiéndome realizar esta tesis en el entorno de la industria.

Finalmente, un agradecimiento especial para mi familia y amigos, sin los cuales no hubiera sido posible la finalización de esta tesis doctoral.

Abstract

The development of safer and more efficient combustion technologies is motivated by the growing environmental concerns related to the global warming. The control of pollutant emissions like carbon monoxide is essential in the design of devices in which fossil fuels are burnt. In indoor environments, CO is largely produced by combustion sources such as cooking and heating appliances. Although appropriate venting installations can avoid unhealthy concentrations of pollutants, practically all the countries and manufacturers limit the production of CO from these devices.

Specifically regarding to the domestic gas cooktops, regulations impose a threshold value for this species emissions, in addition to a minimum value of efficiency and flame stability requirements. Then, the combination of the highest thermal efficiency of the burner with the lowest CO emissions is a challenging and permanent target in the design of domestic gas cooking burners. In that sense, a deep understanding of the fluid dynamics and the chemistry of the flame is essential, so the numerical predictions by computational fluid dynamics techniques are playing a fundamental role, achieving important insights and considerable savings in the product development cycle.

An accurate modeling of domestic gas cooking burners comprises complex three-dimensional geometries; besides, the description of chemistry inside the combustion process is taken into account through a set of chemical reactions and species. The combination between these two factors is translated into enormous computational requirements, often making unaffordable the simulation of real configurations with a full chemistry

description. The complexity of the computational calculations can be overcome by the combination of different strategies. On the one hand, real CAD configurations can be geometrically simplified, allowing a detailed representation of the chemistry to accurately analyze all the physical phenomena (e.g., the flame-wall interaction, heat exchange) that are taking place. On the other hand, the description of the chemistry can be performed by the use of global or reduced kinetic mechanisms to surrogate the detailed combustion reactions; naturally, this strategy entails a reduction of the accuracy of the numerical predictions, which may result into wrong values of pollutant emissions such as CO. Therefore, a balanced approach between the computational solving time and the accuracy in the prediction must be considered, mainly in innovation and development departments of industrial organizations.

In view of the above, this thesis exposes an in-depth analysis of the methane combustion process, looking into the chemistry and the main physical phenomena happening in a combustion device like a domestic gas cooking burner. Experimental and numerical studies are carried out, focusing the research on the formation of carbon monoxide.

The first part of this work is dedicated to the evaluation of the numerical performance of the methane combustion chemistry models. Three different configurations are analyzed, comparing the results of each chemical reaction mechanism to detailed chemistry and experimental values, when available. The results lead to the determination of the best options to surrogate the detailed chemistry, considering a balanced approach between the accuracy in the prediction and the associated computational load. Besides, a new skeletal mechanism has been generated, which is being used in complex simulations of domestic gas cooking burners.

Next, the formation of carbon monoxide in the methane combustion process is evaluated by a set of experimental and numerical analyses, using a geometrically simplified configuration which retain physical conditions similar to those present in a domestic gas cooking burner: a single partially premixed flame impinging perpendicularly onto the bottom wall of a water

pot. The validation of the results is based on flow field measurements of velocity, temperature and carbon monoxide emissions, under different operating conditions caused by variable burner-to-pot distance, flame thermal power, primary aeration, and inside-pot water temperature. The influence of each of these parameters on the final CO emissions is outlined.

Once the results are validated and the CO formation trends are identified, the final part of this thesis is devoted to an extensive study on how the flame-wall interaction phenomena affect the flame and subsequently the final CO emissions. A strong relationship between the internal structure of the flame and both the carbon monoxide production and the thermal efficiency of the burner has been revealed. These parameters reach their maximum value in a coincident operating point in which the inner premixed flame cone is broken by its interaction with the pot wall. The study of the premixed and diffusion zones of the flame where carbon monoxide chemically reacts reveals that the final value of CO emissions is strongly driven by the propagation of the CO-reacting premixed zone (where CO reacts with oxygen coming from the partially premixed stream), which is constrained by the presence of the pot. The analysis of the CO chemical reactions occurring inside the flame reinforces the fact that the global CO production is a consequence of the combination of the local conditions (flow, temperature, species concentration) determined by the flame structure, modifying the reaction rates and subsequently the final emissions.

On the whole, this thesis contributes in giving rigorous guidelines for an optimal design of a domestic gas cooking burner, identifying reachable principles in both performance and pollutants emission thresholds.

Resumen

El desarrollo de tecnologías de la combustión más seguras y eficientes está motivado por las crecientes preocupaciones medioambientales relacionadas con el calentamiento global. El control de las emisiones contaminantes como las de monóxido de carbono es esencial en el proceso de diseño de los aparatos en los que se queman combustibles fósiles. En el interior de un hogar, el CO es producido principalmente por electrodomésticos utilizados para cocinar o calentar la vivienda. Aunque con instalaciones de ventilación adecuadas se pueden evitar concentraciones nocivas de contaminantes, prácticamente todos los países y fabricantes limitan la producción de CO de estos aparatos.

En lo que respecta a las cocinas de gas, las normativas imponen un valor límite para las emisiones de esta especie, además de unos requisitos mínimos de eficiencia y estabilidad de la llama. Por lo tanto, la combinación de una elevada eficiencia térmica del quemador con bajas emisiones de CO es un objetivo ambicioso y permanente en el diseño de los quemadores domésticos de gas. En ese sentido, resulta imprescindible un conocimiento profundo de la fluidodinámica y de los procesos químicos que ocurren en la llama; por ello, los cálculos numéricos mediante técnicas de dinámica de fluidos computacional desempeñan un papel fundamental, logrando importantes avances y un ahorro considerable en el ciclo de desarrollo de un nuevo producto.

El modelado de un quemador doméstico de gas conlleva la utilización de geometrías tridimensionales con gran complejidad; además, la descripción de la química del proceso de combustión ha de tenerse en cuenta a través de un conjunto de especies y reacciones. La combinación de estos dos factores se

traduce en requisitos de potencia de cálculo muy elevados, lo cual hace que a menudo sea imposible llevar a cabo la simulación de configuraciones reales con una descripción completa de la química. La complejidad de los cálculos computacionales puede reducirse mediante la combinación de diferentes estrategias. Por una parte, las configuraciones reales pueden simplificarse geométricamente, lo que permite una representación detallada de la química para analizar con precisión todos los fenómenos físicos (por ejemplo, la interacción entre la llama y la pared o el intercambio de calor) que tienen lugar. Por otro lado, la descripción de la química puede realizarse mediante el uso de cinéticas globales o reducidas, sustituyendo los modelos cinéticos más detallados. Naturalmente, esta estrategia supone una reducción en la precisión de las predicciones numéricas, lo que puede dar lugar a valores erróneos de las emisiones de contaminantes como el CO. Por lo tanto, debe considerarse un equilibrio entre el tiempo computacional y la precisión de los cálculos, principalmente en los departamentos de innovación y desarrollo de organizaciones industriales.

En vista de lo anterior, esta tesis expone un análisis en profundidad del proceso de combustión del metano, examinando la química y los principales fenómenos físicos que tienen lugar durante la combustión en un aparato como un quemador doméstico de gas. Se realizan estudios experimentales y computacionales, centrando la investigación en la formación del monóxido de carbono.

La primera parte de este trabajo está dedicada a la evaluación del comportamiento numérico de los modelos cinéticos para la combustión del metano. Se analizan tres configuraciones diferentes, comparando los resultados de cada mecanismo de reacción con el modelo de química detallada y con valores experimentales, cuando se dispone de ellos. Los resultados conllevan a la determinación de las mejores opciones para sustituir el cálculo de la química detallada, teniendo en cuenta un equilibrio entre la precisión requerida y la carga computacional asociada. Además, se ha generado un nuevo mecanismo reducido que se está utilizando en simulaciones de quemadores domésticos de gas muy complejas.

A continuación, se evalúa la formación de monóxido de carbono en el proceso de combustión del metano mediante un conjunto de análisis experimentales y numéricos, utilizando una configuración geométricamente simplificada que mantiene unas condiciones físicas similares a las presentes en un quemador doméstico de gas: una llama sencilla, parcialmente premezclada, que impacta perpendicularmente en la pared inferior de un recipiente lleno de agua. La validación de los resultados se basa en mediciones del campo de flujo de la velocidad, la temperatura y las emisiones de monóxido de carbono, bajo diferentes condiciones de funcionamiento causadas por la variación de la distancia entre el quemador y el recipiente, la potencia térmica de la llama, la aireación primaria y la temperatura del agua en el interior del recipiente. Con ello, se estudia la influencia de cada uno de estos parámetros en las emisiones finales de CO.

Una vez completa la validación de los resultados, e identificadas las tendencias de formación de CO, la parte final de esta tesis está dedicada a un amplio estudio sobre cómo los fenómenos de interacción llama-pared afectan a la misma y, por consiguiente, a las emisiones finales de CO. Se ha descubierto una fuerte relación entre la estructura interna de la llama, la producción de monóxido de carbono y la eficiencia térmica del quemador. Ambos parámetros alcanzan su valor máximo en la misma condición de funcionamiento, que coincide con la ruptura del cono de premezcla interior de la llama, provocada por su interacción con la pared del recipiente. El estudio de las zonas de premezcla y difusión de la llama donde el monóxido de carbono reacciona químicamente revela que el valor final de las emisiones de CO está estrechamente relacionado con la propagación de la zona de premezcla para el CO (donde el CO reacciona con el oxígeno procedente de la corriente parcialmente premezclada), que está limitada por la presencia del recipiente. El análisis final de las reacciones químicas del CO que se producen en el interior de la llama refuerza la conclusión de que las emisiones finales de ese contaminante son consecuencia de la combinación de las condiciones locales (flujo, temperatura, concentración de especies) determinadas por la estructura de la llama, que modifican las velocidades de reacción y, por

consiguiente, la formación neta de CO.

En general, esta tesis contribuye en la generación de directrices para un diseño óptimo de un quemador doméstico de gas, identificando pautas alcanzables relacionadas con el rendimiento y con los limites de emisión de contaminantes.

Contents

List of Figures

List of Tables

Chapter 1

Introduction

1.1 Motivation

Natural gas (NG) is a resource consisting mainly of methane (> 90% vol. dry) and small traces of heavier hydrocarbons and gases such as carbon dioxide or nitrogen [1]. It is a very important energy source in the world and the fastest growing fossil fuel, accounting today for 23% of the global primary energy demand and nearly a quarter of electricity generation [2]. Its consumption has grown over the last decades (Figure 1.1), with an increase of 2.6% per year since 2000. In 2018, this value reached a maximum of +4.6%, spurred by the United States and China, which are responsible for around 70% of the additional consumption. In the U.S., gas demand grew by 10% (the highest growth seen in this country in the past 30 years), driven by the power sector (new gas-fired power plants) and buildings. In China, its coal-to-gas substitution policy in the power and heating sector led to an increase of 18%.

The residential sector utilizes NG to heat buildings and water, cooking, and drying clothes. About half of the homes in the United States use NG for these purposes [4], while 37.1% of the final energy consumption in the residential sector of Europe is covered by NG [5]. In 2018, the residential sector accounted for about 17% of total U.S. natural gas consumption (Figure 1.2). Projections to 2050 show a steady growth in NG consumption,

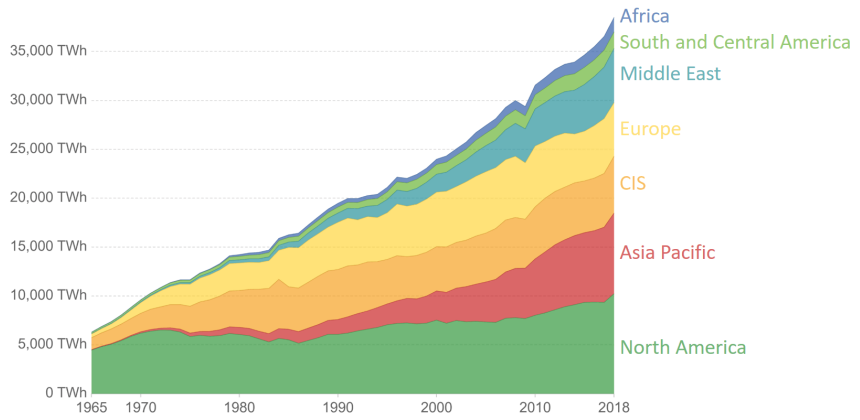

Figure 1.1: Worldwide NG consumption by region, from 1965 to 2018. [3]

particularly due to its vast resources and the persistent demand from the electric power generation and industrial sectors [6]. Therefore, NG will unanimously continue playing an important role in the energy mix for long. In that context, the design and optimization of energy efficient devices, with the lowest release of unburnt matter, pollutant emissions (e.g. CO, NOx) and greenhouse gases (GGs) such as carbon dioxide (CO_2), is essential for any energy and environment outlook.

Despite its fossil origin, NG is considered in several scenarios as the main component to moderate the dependence of oil and to mitigate the resulting GGs from its combustion, compared to other fossil fuels. The use of NG as fuel is responsible for 20% of the worldwide total CO_2 emissions, behind coal (44%) and oil (35%) [7]. Notwithstanding this fact, concerns about the global warming due to the CO_2 raising in the atmosphere, are increasing the pressure to totally cut off the use of fossil fuels, even the NG, in the short term and replace them by using renewable sources and an electrification of the consumption sector. However, a feasible step towards decarbonization of the energy sector will be only achievable if green gases such as bio-methane or synthetic methane exploit the current and modern NG infrastructures of many countries [8]. In such a scenario, all the NG (particularly the methane component) knowledge remains extremely relevant.

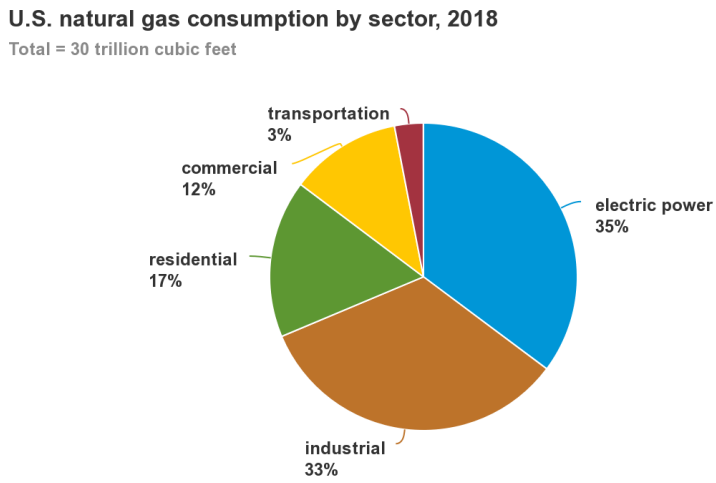

Figure 1.2: Distribution by sector of the NG consumption in the United States in 2018. [4]

Combustion is the main pathway to extract the chemical energy of methane. The process is commonly described by an oxidation reaction which greatly produces CO_2 and H_2O. However, a partial oxidation is normally produced and carbon monoxide (CO) appears in the exhaust hot gases. This gas is one of the most common and widely distributed air pollutants. It is a colorless, odorless and tasteless gas that is poorly soluble in water, with a slightly lower density than air. The amount of CO emitted, relative to the amount of carbon dioxide (CO_2) generated, is sensitive to conditions in the combustion zone. The CO production, relative to CO_2, generally decreases with any increase in fuel oxygen (O_2) content, burn temperature, or mixing time. Therefore, there is not a universal rule to determine a priori the CO emissions of an specific configuration but its final amount depends on the local design conditions.

CO is considered a poisoning pollutant due to the harmful effects on human health when exposed to prolonged inhalation of moderate concentrations of this gas. These effects could include occasional episodes of headaches, fatigue, and dizziness, till chronic heart diseases depending on the concentration and the exposure period (Table 1.1). CO intoxication can

Table 1.1: Carbon monoxide concentrations, associated symptoms and possible occurrences (adapted from [10]).

Concentration	Symptoms	Occurrence
35 ppm	Dizziness, headache within 6-8 hours of constant exposure	Smoking in bars, restaurants
100 ppm	Dizziness, headache in 2-3 hours	Exhaust from a 37kW boiler
200 ppm	Dizziness, headache within 2-3 hours; loss of judgment	Cooking inside a tent
400 ppm	Frontal headache within 1-2 hours; fatal in ≈8 hours	Running car inside a garage for 2 minutes
800 ppm	Dizziness, nausea, and convulsions within 45 minutes; insensible within 2 hours	Barbecue inside a house
1,600 ppm	Headache, increased heart rate, dizziness, nausea within 20 minutes; death in less than 2 hours	Smoldering fire
3,200 ppm	Headache, dizziness and nausea in 5-10 minutes; death within 30 minutes.	Fire
6,400 ppm	Headache, dizziness in 1-2 minutes. Convulsions, respiratory arrest; death in less than 20 minutes.	Exhaust gases of an old car
12,800 ppm	Unconsciousness after 2-3 breaths; death in less than 3 minutes.	Smoldering coal fire

be caused by single or repetitively generated high short-term peaks, and it is the leading cause of death (accidental and intentional) from poisoning [9].

In indoor environments, CO is largely produced by combustion sources such as cooking and heating appliances producing smoke. Although appropriate venting installations can avoid unhealthy concentrations of pollutants, practically all the countries and manufacturers limit the production of CO from the combustion devices. Specifically regarding to the cooking appliances, regulations like the European Standards [11, 12] impose a restrictive threshold value for carbon monoxide emissions, in addition to a minimum value of efficiency and flame stability requirements in all the operational range. Here, the combustion process is altered due to the interaction between flame and solid elements such as thermocouples, grills or pots. This phenomenon, so-called flame-wall interaction (FWI), induces perturbations and quenching of chemical reactions, which may lead to undesirable effects in pollutant emissions and heat exchange [13–15]. For hydrocarbon fuels, the CO presence in the exhaust gases tends to constrain the possibilities in the design process. Thus, the combination of the highest thermal efficiency of the burner with the lowest CO emissions is a challenging

and permanent target in the design of domestic gas cooking burners. This process entails a sort of trial-and-error engineering design workflow. Traditionally, a large number of physical prototypes and laboratory tests have been necessary, with the consequential required time and expense. Nowadays, this process is being increasingly replaced by the use of numerical simulation techniques, such as the finite element [16] or the finite volume [17] methods, embedded in software to solve and represent the physical laws of the involved phenomena. By means of them, important insights and considerable savings in the product development cycle (Figure 1.3) are achieved.

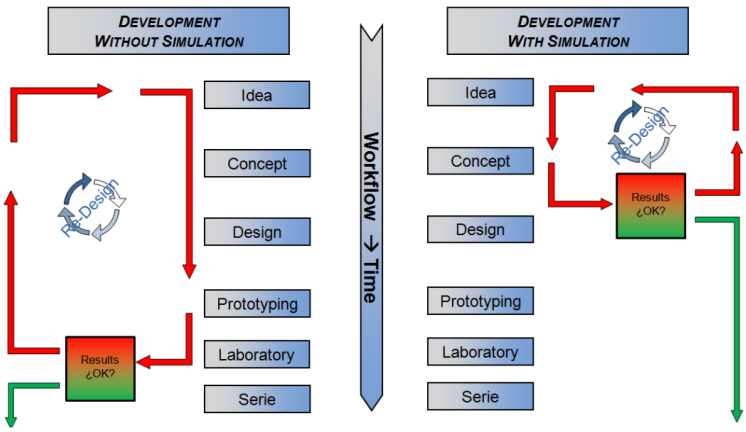

Figure 1.3: Advantages of the use of simulation in the Product Development Process. [18]

For cases where a fluid flow is involved, simulations are usually carried out by the use of computational fluid dynamics (CFD) [19] codes. These tools are being increasingly employed to solve the fluid flow and the combustion processes taking place at gas cooking burners. An accurate CFD modeling of these devices comprises complex three-dimensional computer-aided design (CAD) geometries, which need to be discretized into several millions of cells. Furthermore, the description of the chemical reaction process is taken into account through a set of chemical reactions and species, including their respective thermo-kinetic parameters, which is

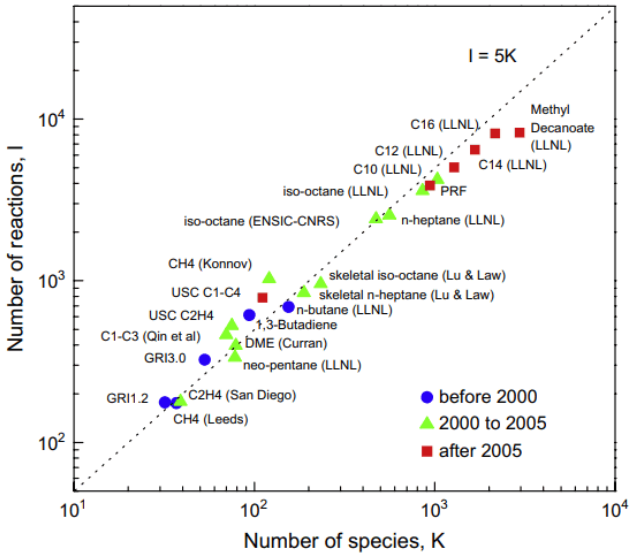

Figure 1.4: Size of chemical reaction mechanisms for some hydrocarbon fuels together with their approximate year of compilation. [20]

typically known as kinetic or chemical reaction mechanism. Depending on the fuel composition, these chemistry databases can comprise thousands of reactions involving hundreds of chemical species (Figure 1.4).

The combination between the complex geometries (e.g., [21–24]) and the high computational cost that the chemical description of the process entails often makes unaffordable the simulation of real configurations with a full chemistry description, at least without the use of high performance computers.

The complexity of the computational calculations can be overcome by the combination of different strategies. Real CAD configurations can be geometrically simplified, which allows a detailed representation of the chemistry to accurately analyze all the physical phenomena (e.g., the flame-wall interaction, heat exchange) that are taking place. The simplification can be done by assuming symmetry or periodic conditions when possible and/or neglecting flow-irrelevant geometry details (CAD cleaning process). Another possibility is the consideration of simpler but

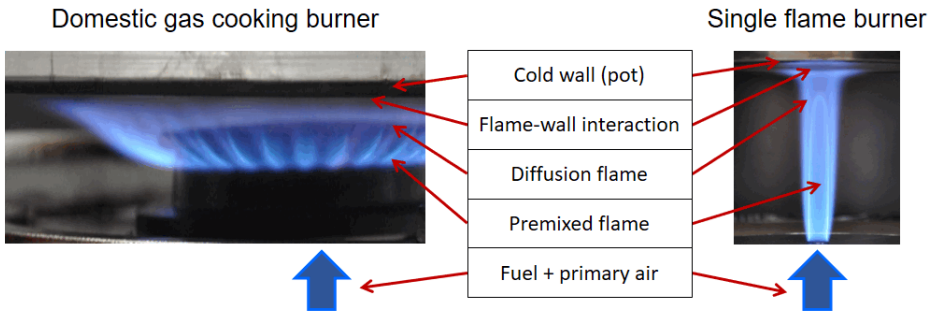

Figure 1.5: Correspondence of the main features between a domestic gas burner and a single flame burner. [18]

realistic configurations such as a single flame impinging onto a wall, allowing the reproduction of the most relevant features and similar conditions present in more complex devices like the domestic gas burners, as can be seen in Figure 1.5.

A different but also common strategy in combustion simulation is renouncing the accurate description of the chemistry by the use of global or reduced kinetics to surrogate the detailed combustion reactions. By doing so, the number of transport equations and their reaction source terms that a CFD code needs to integrate and solve is considerably lower. However, this type of analysis highly focuses on very specific operating conditions, achieving limited results such as the temperature field, the heat exchange, and the final products of the combustion like CO_2 and H_2O [25,26].

A distinct group of approaches comprises the pre-calculation and storage of all the foreseeable combustion reaction states, obtained from one-dimensional flames. Given the simplicity of these geometries, those prior prediction results are normally computed using accurate or detailed reaction mechanisms. Later on, these data are consulted by a CFD calculation, avoiding the numerical integration of the combustion reaction on the fly, and producing therefore a drastic reduction in the computational time. However, the main drawbacks of this type of strategies come from the inability of the 1-D flame configuration to fully characterize the real 3-D phenomena such

as heat losses or reaction quenching [27].

Most of the reference studies involving domestic gas cooking burners are focused on experimental analysis [22–24, 28–40]. Only a few articles containing the numerical simulation of the process have been published. In them, the description of the chemistry is handled by the use of simple global reaction mechanisms. The two-step mechanism developed by Westbrook and Dryer [25] is used by Gattei [41] in the prediction of occurrence of the flame lift instability, relying on CO value as a marker of the starting reaction. Another two-step mechanism for natural gas combustion developed by Bibrzycki et al. [42] is employed by Boggavarapu et al. [21], who do not compare experimental results with numerical predictions but only use them as a guidance for trends in order to improve the performance of the burner. There are some other published studies that involve slightly different type of methane-air burners, but either they use a similar simplistic approach for chemical kinetics [43] or the combustion is developed under turbulent regime, and therefore the turbulence-chemistry interactions determine the approach to be used [44, 45]. Regarding the pre-calculation and storage of the chemistry as an alternative to alleviate the CFD integration on the fly, the Flamelet-Generated Manifold (FGM) approach is evidenced in some studies [27, 46]. However, although the pre-calculation is carried out using simple one-dimensional flames, a reaction mechanism is needed.

The levels of carbon monoxide produced in the combustion is one of the greatest challenges during the design and therefore in the numerical simulations of domestic gas cooking burners. Thus, a suitability study of the available methane combustion mechanisms for this type of systems is of great relevance. Additionally, the laminar flow regime where the combustion takes place in these devices reinforces the need of an accurate prediction of the molecular diffusion processes and the intermediate chemical species such as carbon monoxide. These requirements stress the available computational resources, so a balanced approach between the accuracy in the prediction and the computational solving time needs to be achieved, mainly in innovation and development departments of industrial organizations.

1.2 Framework

This thesis has been carried out in the framework of a collaboration between the Department of Chemical and Biomolecular Engineering of the University of Cantabria and the company BSH Home Appliances Group. The work has been circumscribed as a part of the R+D activities carried out by the Simulation Team of the BSH Gas Competence Center, located in Santander (Cantabria, Spain). This center is fully committed to the design and manufacture of gas cooktops such as the one seen in Figure 1.6, and has the mission to support technically and worldwide the development of the gas technology for cooking applications.

Figure 1.6: Example of a gas cooktop manufactured in BSH Santander. [18]

Domestic gas cooktops are complex appliances with a large number of elements: burners, pan supports, knobs, valves, pipelines, and electronic components. All together work synchronously to assure the maximum energy efficiency with the minimum emission levels. However, the burners can be considered the core technology. In these devices, a mixture of fuel gas and oxidizer, normally ambient air, is ignited to produce a controlled flame used for cooking. The main parts in which a burner is divided are the following (Figure 1.7a):

- The injector, through which an overpressured gas fuel emerges.
- The mixing tube, engaged to mix the fuel and air.

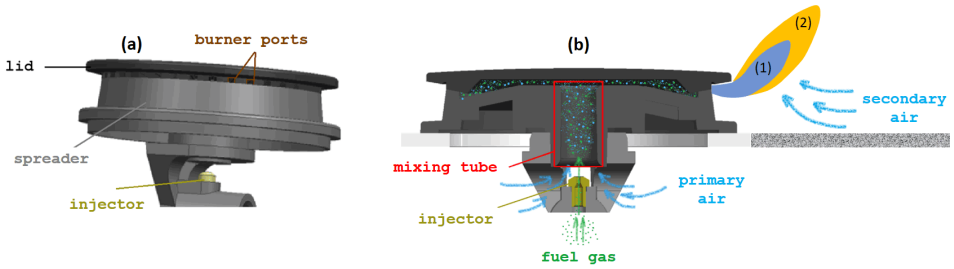

Figure 1.7: Main parts of a domestic gas burner (a) and a basic scheme of its interior (b)(adapted from [47]).

- The spreader, that redirects the gas to the ports.
- The lid, which promotes a proper flow of the mixture towards the burner ports.

Once the fuel gas leaves the injector, it joins together with the primary air by a momentum-sharing process between the gas and the ambient air. The mixture is produced through the mixing tube (Figure 1.7b), which may be shaped as a venturi tube. Then, the mixture impacts the lid and is redirected through the spreader to the burner ports. So far there is no combustion in the process; a spark is needed to initiate the reaction when the concentrations of air and fuel are within the flammability limits.

A fundamental aspect in the burner performance is the air entrainment process, because it has a considerable effect on the stability, shape, and temperature distribution of the flame. It depends mainly on the internal geometry of the burner and on the physical properties of the gas fuel and the air. If the amount of air is exactly the required to completely burn all the fuel, the mixture is stoichiometric. However, the proportions of the reactants in the mixture for these burners are normally below the stoichiometric conditions. That is the reason why these devices are classified as partially premixed (or aerated) burners. The air-fuel ratio (AFR) is defined by the composition of the mixture just before leaving the burner ports, and can be normalized for each fuel by using the corresponding stoichiometric concentrations to bring about the air-fuel equivalence ratio (lambda, λ) or

its reciprocal fuel-air equivalence ratio (Φ) as

$$\lambda = 1/\Phi = \frac{AFR}{AFR_{stoich.}} = \frac{(Y_{air}/Y_{fuel})}{(Y_{air}/Y_{fuel})_{stoich.}} \ , \tag{1.1}$$

where Y stands for the mass fraction of the mixture components. Thus, $\lambda = \Phi = 1$ means that the mixture is stoichiometric. If there is an excess of fuel in the mixture, it is called a fuel-rich mixture ($\lambda < 1$). On the contrary, if there is an excess of oxygen, it is called a fuel-lean mixture ($\lambda > 1$). Domestic gas cooking burners operate under partially premixed regime, i.e. fuel-rich conditions, typically with an air-fuel equivalence ratio in the range of $0.3 < \lambda < 0.8$. In these cases, the flame presents a structure made up of two different zones (Figure 1.7b): (1) an initial premixed fuel-rich reaction front, where there is not enough oxygen coming from the primary air to complete the chemical reactions; and (2) a subsequent region where the completeness of the combustion requires the transport by diffusion of oxygen from a secondary air stream.

One of the most technical challenges during the burner design is fitting out the appropriate mixture conditions (fuel/air proportions and homogeneity) to guarantee the structure and stability of the flame. In order to achieve it, a deep understanding of the fluid dynamics and the chemistry of the flame is essential and the simulation by CFD techniques plays a fundamental role.

1.3 Objectives of the thesis

The growing environmental concerns are pushing to develop safer and more efficient combustion technologies. The control of pollutant emissions like carbon monoxide, mainly indoors, will continue as a mandatory requirement for most of the countries, even in the cases where renewable methane may be burnt. In that sense, the numerical predictions by CFD techniques will be certainly a must-have in the design of domestic gas cooking burners.

The main goal of this thesis is to contribute in two research lines related

with the carbon monoxide prediction: (1) in the analysis of the state of the art of methane combustion chemistry models, and (2) in the comprehension of the main physical phenomena behind the CO formation in this type of systems. In order to fulfill this central target, the subsequent partial milestones have been established:

- Evaluate the numerical performance of different chemical reaction mechanisms to describe the methane combustion in a simulation process, focusing on the carbon monoxide prediction. By doing so, determine the best options to surrogate the detailed chemistry, considering a balanced approach between the accuracy and the computational time, in industrial applications such as domestic gas cooking burners.

- Design a geometrically simplified experimental configuration which retain physical conditions similar to those present in a domestic gas cooking burner: a single partially premixed methane flame impinging perpendicularly onto the bottom wall of a water pot. From this workbench, obtain flow field measurements of velocity, temperature and CO emissions for different conditions produced by the modification of the burner-to-pot distance, the flame thermal power, the primary aeration, and the inside-pot water temperature.

- Set up the simulation model of the single flame burner configuration and validate the numerical results by the comparison of variables under the same conditions.

- Study the influence of the parametric variation on the carbon monoxide emissions and the thermal efficiency of the burner in order to identify the main trends of the flame-wall interaction phenomena.

- Deeply analyze the changes in the flame structure and the carbon monoxide reaction rates to identify relationships among the evolution of the flame shape and its interaction with the wall, the overall

completeness of the combustion reaction, and the local production and consumption of CO.

By means of achieving the later objectives and milestones, the present research pretends to contribute in giving rigorous guidelines for an optimal design of a domestic gas cooking burner, minimizing the carbon monoxide emissions while maximizing the thermal efficiency.

1.4 Outline

Once the thesis is contextualized and the main objectives are established, Chapter 2 includes the performance analysis of chemical reaction mechanisms developed to numerically describe the methane combustion. For the study, the mechanisms are classified according to their size and origin as global, skeletal, and detailed. Three different configurations are utilized. Firstly, classical one-dimensional free flames are employed to obtain laminar flame speed (LFS) values. This parameter is usually considered a fundamental reference for the performance comparison of the mechanism behavior, because it globally outlines the flame shape, and therefore influences the temperature and chemical species fields. Secondly, a single, partially premixed laminar flame is used to evaluate temperature and major species profiles. Given its simplicity and the availability of experimental data, this configuration is a great candidate to be used as a reference case to validate numerical approaches. The third configuration is a realistic three-dimensional gas cooking burner, utilized to assess the mechanisms' performance in the prediction of parameters related to the certification standards, namely thermal efficiency and CO emissions. Finally, a global statistical evaluation is proposed to quantify the accuracy of the mechanisms, both with experimental and detailed chemistry data as reference, followed by some conclusions drawn from the study.

Next, Chapter 3 details the experimental and numerical analysis of the flow field of a single methane flame burner, perpendicularly impinging onto a cold wall. After a brief introduction about the flame-wall interaction

phenomena, the state of the art on this topic is reviewed, highlighting those studies which include pollutants emission data. The experimental facility, designed on purpose for this study, is then described. Subsequently, the conditions of the programmed tests are detailed, with different values of burner-to-pot distance, flame thermal power, primary aeration, and inside-pot water temperature. Once the computational setup of the configuration is specified, both experimental and numerical results are discussed, distributed in three different blocks: flow velocity features (non-reactive and reactive), temperature, and carbon monoxide emissions. The chapter ends with an statistical evaluation of the modeling and some partial conclusions.

Starting from the main results obtained in Chapter 3, Chapter 4 is devoted to the extensive study of the flame-wall interaction phenomena that occurs in the single methane flame burner configuration, and its influence on the flame structure and the carbon monoxide emissions. To do so, extra numerical calculations are carried out in order to obtain a more detailed evolution of CO emissions at intermediate values of flame thermal power. The analysis of the results leads to strong relationships between the structure of the flame resulting from its interaction with the pot wall and the net carbon monoxide formation. A list of conclusions is presented to finish the chapter.

Finally, Chapter 5 summarizes the main conclusions of this thesis and outlines possible future lines of research.

Chapter 2

Methane combustion kinetics

This chapter is devoted to the performance evaluation of the chemical reaction mechanisms for the simulation of methane combustion processes. First, the mechanisms are presented and classified as global, skeletal and detailed. Next, the configurations employed to analyze their performance are described. Three different tests are proposed: laminar flame speed calculation using a one-dimensional flame model; temperature and major species evolution in a simple, two-dimensional flame model; and pollutant emissions and thermal efficiency in a complex, three-dimensional domestic gas burner model. The following section contains the corresponding results for each configuration and the discussion, including a statistical evaluation of the accuracy of the evaluated mechanisms. Finally, main conclusions drawn from the study are presented.

The final goal of this analysis is the determination of the best mechanisms to surrogate detailed chemistry for the simulation of methane combustion in a domestic gas cooking burner, taking into account both prediction of parameters of interest such as pollutant emissions and thermal efficiency, and their computational load.

2.1 Chemical reaction mechanisms for methane combustion

For the analysis of methane-air combustion, the latest version of the mechanism developed by the Gas Research Institute (GRI), known as GRI-Mech 3.0, is widely used as the reference reaction mechanism. It is an optimized set of 325 elementary chemical reactions, associated rate coefficient expressions and thermo-chemical parameters for 53 species, including NOx formation and reburn chemistry. It was originally designed over the ranges 1000-2500 K, 1-1000 kPa, and Φ from 0.1 to 5 for premixed systems [48].

Table 2.1: Classification of the evaluated chemical reaction mechanisms suitable for methane-air combustion.

Type	Mechanism	N. Species	N. Reactions	Reference(s)
Global	1Step	5	1	[25]
	2Steps	6	2	[25]
	JL	7	4	[26]
	JL-mod	7	5	[49]
Skeletal	SL11	11	19	-
	Smooke	16	35	[50]
	Lu-sk17	17	73	[51,52]
	DRM19	21	84	[53]
	DRM22	24	104	[53]
	gfn26	26	143	[54]
	Lu-sk30	30	184	[51,55]
Detailed	GRI-Mech 1.2	32	177	[56]
	Leeds	37	351	[57]
	GRI-Mech 2.11	49	279	[58]
	GRI-Mech 3.0	53	325	[48]

Several studies have focused their efforts on the development of simpler mechanisms to surrogate detailed chemistry, and therefore reduce the high computational load that entails its use. Table 2.1 classifies the options

available in the literature that were originally created to describe the combustion process of methane, including the number of chemical species and reactions that they contain, as well as their main reference(s).

2.1.1 Global

The far side of possibilities is represented by the global reaction mechanisms, which generally reproduce essential properties of flames such as laminar flame speed, major species or temperature under certain mixing or environmental conditions. Their deduction process is based on general optimization or empirical methods. The simplest mechanisms for methane-air combustion, described by one and two reaction steps (hereinafter 1Step and 2Steps respectively), are included in this group. These mechanisms were originally developed by Westbrook and Dryer [25] and are the options normally included by default in commercial CFD codes for chemical kinetics problems. The four-step mechanism developed by Jones and Lindstedt [26] (JL) and its five-step subsequent modification by Andersen et al. [49] (JL-mod) are also classified as global mechanisms.

2.1.2 Skeletal

The skeletal mechanisms (also simply known as reduced) are those obtained by neglecting irrelevant species and reactions from a detailed mechanism in order to produce a reduced-size one. This type of reduction is based on either comprehensive consideration or a particular application. It can be achieved by several methods: Jacobian analysis [59]; detailed reduction [60]; directed relation graph [61] (DRG); DRG with error propagation [62] (DRGEP); DRG with path flux analysis [63] (DRGPFA); DRG-aided with sensitivity analysis [52,64] (DRGASA); and DRG with error propagation and sensitivity analysis [65] (DRGEPSA). Skeletal mechanisms in this work can be further classified depending on their origin. Firstly, the mechanism presented by Smooke and Giovangigli [50] (Smooke), which was directly proposed in a workshop as a skeletal methane-air reaction mechanism. Secondly,

mechanisms developed by Lu et al. [51, 52] (Lu-sk17) and Kazakov and Frenklach [53] (DRM19 and DRM22), that were originally obtained from a previous release of the GRI-Mech (version 1.2 [56]). Finally, the mechanism recently proposed by Gimeno-Escobedo et al. [54] (gfn26) and another one by Lu et al. [51,55] (Lu-sk30), which are based on the GRI-Mech 3.0 mechanism.

Apart from these options, a new skeletal mechanism has been developed within the framework of this thesis. The reduction process started from GRI-Mech 3.0, and the goal was to accurately predict temperature and carbon monoxide values, including as few species as possible. The resulting mechanism contained 11 species and 19 chemical reactions; as a final step, an optimization process was applied. Further information is included in Appendix 2.A.

2.1.3 Detailed

Apart from the GRI-Mech 3.0 mechanism, there exist two previous releases which are still suitable to be used, namely, GRI-Mech 1.2 [56] and GRI-Mech 2.11 [58]. The three versions, along with the Leeds mechanism [57], fill out the detailed mechanisms group for the study.

2.1.4 Other mechanisms

There exist in the literature some other possibilities which include detailed C1-C4 hydrocarbons chemistry (e.g. AramcoMech [66], USC Mech II [67], UCSD mechanism [68]). All these options are not normally used in CFD simulations without a prior reduction process.

Other strategies utilize a combination of skeletal reaction mechanisms and the quasi-steady state (QSS) approximation for intermediate species with short timescales that reach chemical equilibrium [69]. Thus, the integration of transport equations is replaced by solving simple algebraic expressions [51, 52, 55, 70–74]. However, this kind of approaches does not fully comply with the well-known Arrhenius formulation. These mechanisms are not directly readable and functional in commercial CFD solvers and

its implementation requires an adaptation through external programmed subroutines.

2.2 Description of the geometrical configurations for the study

The performance of the mechanisms presented previously is analyzed in terms of laminar flame speed and variables of interest like temperature, major species and heat fluxes, among others. Table 2.2 shows the geometrical configurations that are employed to asses this performance.

Table 2.2: Relationship between the assessment parameter and the geometrical configuration used to obtain it.

Studied parameter	**Configuration utilized**
Laminar flame speed	1-D laminar premixed flame
Temperature and major species	2-D laminar partially premixed flame
CO emissions and thermal efficiency	3-D gas cooking burner

Initially, a one-dimensional flame model is used to obtain laminar flame speed profiles. Subsequently, two-dimensional and three-dimensional configurations are employed to compare variables of interest like temperature, major species or heat exchange. In all the former cases, conservation equations of mass, momentum, energy and species need to be solved (see Appendix I). The final formulation of the equations naturally depends on the dimensionality of each type of configuration. The solver code addresses the specific problem in steady-state formulation. Likewise, net chemical production rate of each species are taken into account adding the specification of gas-phase reactions, thermodynamic, and transport properties data contained by means of special formatted files (Chemkin format) to the solver. These files are directly read by the software.

The approach to numerically describe the combustion process that takes place in any configuration depends on the flow regime, being laminar

Table 2.3: Maximum Reynolds number and flow regime in analyzed configurations

Configuration	**Zone**	v_{max} **(m/s)**	$\mathbf{Re}_{max}$	**Regime**
1-D	-	< 1	-	Laminar
2-D	-	0.61	150	Laminar
3-D	Mixing	96.3	3900	Turbulent
	Combustion	4.8	260	Laminar

or turbulent. Maximum Reynolds number for each studied configuration is presented in Table 2.3. Assuming that the flow is laminar when Re $<$ 2000 [75], in all the cases combustion is developed under laminar conditions, so the process is entirely governed by chemical kinetics and none turbulence-chemistry interaction is needed. However, the mixing between fuel and primary air in the 3-D gas burner configuration is developed under a turbulent environment, thus, a turbulence model needs to be enabled in these simulations.

The mixture is considered to be a multicomponent ideal gas where density depends only on temperature and composition. Kinetic theory is invoked for transport properties such as viscosity, thermal conductivity and mass diffusivity. A complete overview of the transport equations can be found in Appendix I.

2.2.1 One-dimensional laminar premixed flame

Laminar flame speed (LFS) is commonly used to characterize the combustion of various fuel-oxidizer combinations and to determine mixture flammability limits. Burner-stabilized one-dimensional laminar premixed flames are often employed to study chemical kinetics in a combustion environment and obtain LFS values. Such flames can be highly stable, facilitating detailed measurements of temperature and species profiles. LFS experiments using a methane-air flame at atmospheric pressure and an unburnt gas temperature of 298 K were reported by Taylor [76] and Vagelopoulos et. al [77], varying

the equivalence ratio between 0.5 and 1.6. These studies are selected for comparison purposes.

LFS computational values are determined using a 1-D premixed laminar flame model embedded in the software ANSYS Chemkin-Pro [78], solving the set of governing equations that describe the flame dynamics using an implicit finite difference scheme with a combination of time-dependent and steady-state methods. Temperature, pressure and equivalence ratio range values are set as in the experiments. Additionally, thermal diffusion (Soret effect) is enabled and multicomponent diffusion transport is chosen for species calculation. The used 1-D domain allows a discretization up to 500 grid points and the length of the domain is set to 22 mm.

2.2.2 Two-dimensional laminar partially premixed flame

A simplified, 2-D axisymmetric laminar partially premixed flame (frequently known as 'Yale flame') is chosen to assess the performance of the mechanisms in terms of temperature and major species prediction. The use of this flame as a validation case is motivated by its simplicity, the availability of experimental measurements, and the fact that it is representative of the processes happening in a real gas cooking burner.

The experimental setup was initially described by Santoro et al. [79] and McEnally and Pfefferle [80]. This flame has been widely studied and reported in literature [80–89]. Its configuration is similar to a Bunsen burner: the fuel enters a cylindrical combustion chamber through an axial duct, surrounded by a coaxial coflow of air (Figure 2.1). The fuel stream consists of a partially premixed mixture of methane and oxygen-enriched air. The flame presents two distinct combustion zones. A first one is located near the nozzle, where the chemistry of the rich mixture controls the reaction as a premixed combustion. Once the primary oxygen is depleted, a second zone is formed, where the diffusion of air from coaxial flow controls the combustion progress.

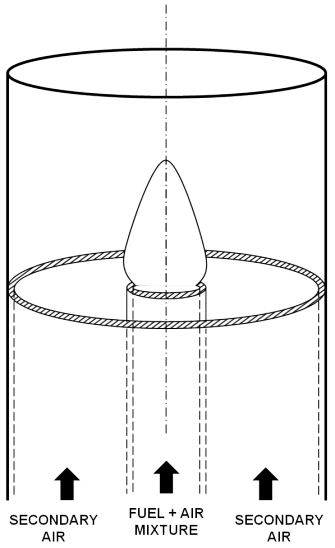

Figure 2.1: Scheme of the laboratory laminar Yale flame (adapted from [89]). For this study, a partially premixed mixture (Φ=2.5) is fed by the central tube.

The experiments reported by McEnally and Pfefferle [88] were carried out with several equivalence ratios for the fuel stream, ranging between Φ=2.5 and infinity (the latter corresponding to a purely diffusion flame). Major species (CH_4, O_2, CO_2) concentration and gas temperature profiles along the flame centerline were reported. Experimental dataset for Φ=2.5 (closest to typical values in domestic gas cooking burners) is taken as reference to compare with simulations and analyze the performance of the different reaction mechanisms.

For the computational setup, a 2-D axisymmetric domain is designed. The initial mesh was composed of 7800 quad cells and has been successively adapted and refined to 59 thousand cells, particularly focusing on the flame zone (Figure 2.2). The fictitious shape of the post-combustion zone is included to enhance the numerical convergence of the solution, keeping away the outlet boundary condition and cooling the products as they move towards the outlet. This design has shown not to alter the results in the flame zone [27].

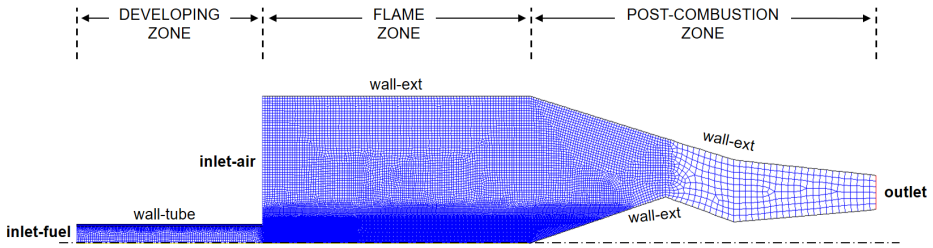

Figure 2.2: 2-D axisymmetric mesh of the Yale flame with identification of the main zones and boundaries of the computational domain.

Unlike the one-dimensional flame model previously described, this is a non-adiabatic CFD calculation where energy losses need to be taken into account. For this sake, continuity, momentum, energy and chemical species transport equations are solved in a steady-state laminar-flow regime using the software ANSYS Fluent [90]. Radiation is considered by means of the Discrete-Ordinate Model (DOM). For the Species Model option, the effect of enthalpy transport due to species diffusion in the energy equation (Diffusion Energy Source) is explicitly considered whereas multicomponent diffusion is enabled. Combustion is Arrhenius-rate governed (Laminar Finite Rate) by Direct Integration of the chemical kinetics in the Stiff Chemistry Solver of the code. Coupled Algorithm for pressure-velocity coupling with PRESTO! (PREssure STaggering Option) scheme for pressure interpolation is selected, whereas second order upwind spatial discretization is applied to the rest of transported variables.

Specific boundary conditions for the model are summed up in Table 2.4. Although inlet streams are fixed at 300 K in the experiments, previous numerical studies using this configuration [86] suggest a temperature of 420 K, given the fact that both streams are heated by radiation from the flame. The central metal tube (solid part) is also included in the computational domain (adjacent zone to wall-tube) so that it is heated up initially mainly by radiation coming from the flame zone and then by conduction to the whole tube.

Table 2.4: Specific boundary conditions set in the numerical simulation of the 2-D partially premixed Yale flame.

Zone	Type	Thermal condition	Other
inlet-fuel	mass-flow-inlet	Inlet $T = 420$ K	$\dot{m} = 2.634x10^{-05}$ kg/s; $\Phi = 2.5$
inlet-air	mass-flow-inlet	Inlet $T = 420$ K	$\dot{m} = 9.353x10^{-04}$ kg/s
outlet	pressure-outlet	Backflow $T = 300$ K	$P_{gauge} = 0$ Pa
wall-tube	wall	Adiabatic	$\epsilon = 1$
wall-ext	wall	Fixed $T = 300$ K	$\epsilon = 1$

2.2.3 Three-dimensional domestic gas cooking burner

The main motivation of this study is the assessment of reaction mechanisms to be used in domestic gas burner analysis. Thus, an actual gas cooking burner is also employed for comparison purposes. The chosen device is the so-called '2.8kW Rapid Burner' (Figure 2.3), which is currently integrated in some domestic gas cooking appliances from BSH company [91]. It is classified as a partially aerated burner, where the fuel stream (pure methane in this study) flows from an injector nozzle and entrains the surrounding fluid by a momentum-exchange process between the fuel jet and the initially stagnated air. This partially premixed mixture enters a venturi tube, designed to ensure a homogeneous mixing. Then, the flow undergoes a direction change and is finally distributed to the burner ports, where is ignited by a spark plug. The flame propagates circumferentially around the burner, until it stabilizes and finally achieves a steady state.

These type of gas burners need to fulfill the standard regulations [11, 12] regarding pollutant emissions and thermal efficiency threshold values. Therefore, all the domestic gas stoves are subject of rigorous certification tests. Experimental CO, CO_2 emissions and thermal efficiency data are directly obtained by the BSH Gas Laboratory.

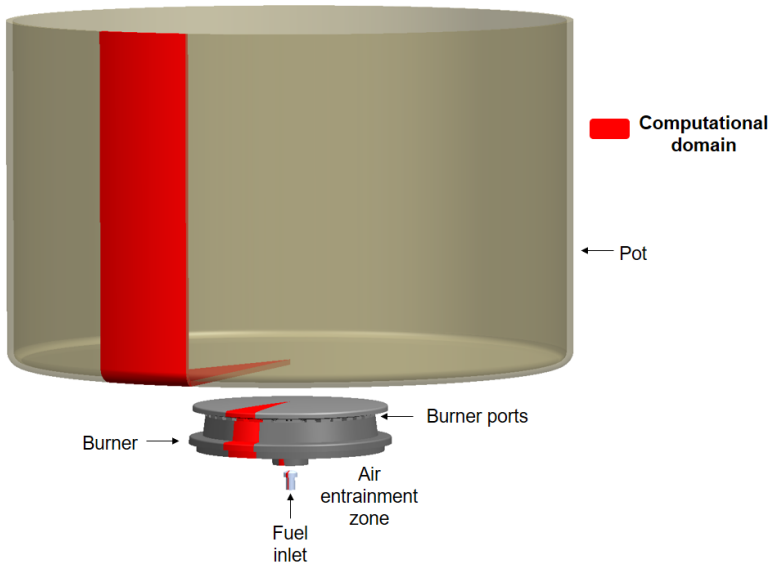

Figure 2.3: Main elements of the 2.8kW Rapid Burner geometry and the computational domain (highlighted) used in this work.

As a summary of the procedure, for this burner, the combustion test is carried out applying a thermal power of 2.8kW and with a 220mm-diameter pot on the pan support. According to the European Standard [11], a bell is placed covering the pot in order to better capture the emissions' sample in the upper part (Figure 2.4a). Combustion products are analyzed by the air-free corrected (0% oxygen) volumetric concentration of CO. This value, frequently known as CO Air Free (COAF), is given by:

$$COAF = (CO)_M * \frac{(CO_2)_N}{(CO_2)_M} \ , \tag{2.1}$$

where $(CO)_M$ and $(CO_2)_M$ are respectively the volumetric percentages of CO and CO_2 collected at the hood outlet and measured on a dry basis (after removing the water vapor from the exhaust gases stream), and $(CO_2)_N$ is the volumetric percentage of CO_2 for the dry, air-free products of the neutral stoichiometric combustion of the fuel (11.7% for methane).

According to the appropriate procedure for the burner working at full power load, the COAF threshold value is 1000 ppm.

Particularly for this burner, according to the process described in the European Standard [12], the thermal efficiency test requires a 260mm-diameter pot (Figure 2.4b), with 6.1kg of water, and adjusting the power to 2.36kW. The procedure reckons consumed gas to increase the water temperature from 20±1ºC to 90±1ºC to determine the energy balance between fed power load and absorbed heat by the pot. Thus, thermal efficiency is given by:

$$\eta = \frac{C_p * m_e * (T_{end} - T_{init})}{V_c * H_s} * 100 \ , \tag{2.2}$$

where η is the efficiency; C_p is the liquid water specific heat; m_e is the equivalent mass of the pan filled; T_{init} and T_{end} are the initial and final water temperatures of the test; V_c is the volume of dry fuel consumed during the test; H_s is the gross calorific value of the gas.

Numerically, considering a steady state assumption, this parameter is obtained relating the heat flux exchanged through the pot walls ($Q_{\rightarrow pot}$) and the fuel chemical power (Q_{fuel}):

$$\eta = \frac{Q_{\rightarrow pot}}{Q_{fuel}} * 100 \ . \tag{2.3}$$

Domestic gas cooking burners are 3-D complex geometries. Their complete discretization usually requires tens of millions of cells, which makes unaffordable the cost of simulating real configurations with full chemistry, at least under an industrial-developing environment such as those present in BSH centers. Thus, a simplified domain consisting of a 3-D slice representing 1/18 part of the full geometry (Figure 2.3) is used. After a preliminary refinement process, resulting meshes are compounded by 1.2 million and 750 thousand cells for the combustion and efficiency tests respectively, with high detail inside the injector, the mixing tube and next to the burner port (Figure 2.4c).

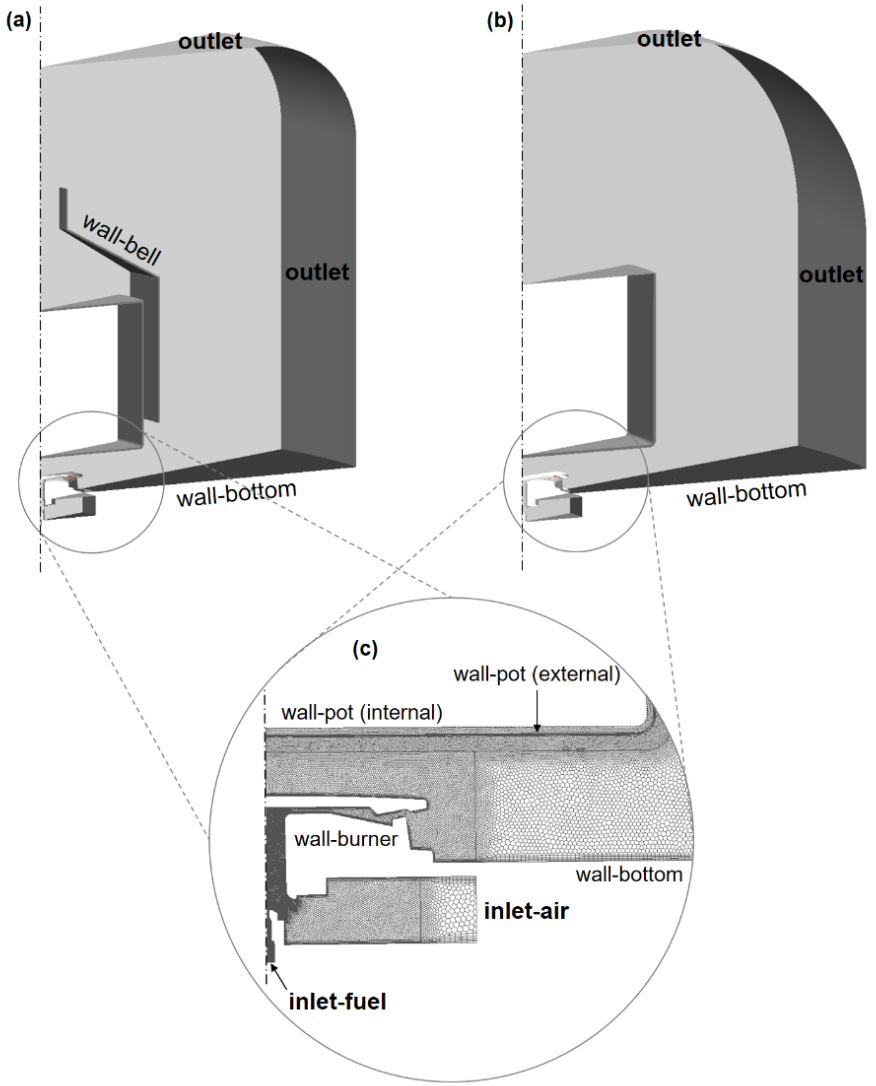

Figure 2.4: Computational domain for (a) combustion test, (b) efficiency test, and (c) mesh detail close to the burner.

Steady-state simulations are carried out with the same CFD software and basically the same numerical setup as in the two-dimensional partially premixed flame. However, in this case, the SST (shear stress transport) k-ω turbulence model is selected in order to describe the turbulent environment of the fuel jet and the air entrainment process, which takes place far from the reaction zone. For combustion modeling, small Damköhler number regime is assumed and hence no turbulence-combustion closure is enabled. There is a conjugated heat transfer due to the presence of the solid pot and water. The heat exchange towards the pot is considered by specifying convective heat transfer coefficients for both water and air surfaces on the internal zone. These and main boundary conditions set for both tests are summarized in Table 2.5.

Table 2.5: Main boundary conditions for the 2.8kW Rapid Burner in the 3-D simulations of combustion and efficiency tests. For identification of zones, see Figure 2.4.

TEST	Zone	Type	Thermal condition	Other
COMBUSTION	inlet-air	pressure-inlet	Inlet $T = 410$ K	$P_{gauge} = 0$ Pa $Y_{O_2} = 0.233$
	inlet-fuel	pressure-inlet	Inlet $T = 410$ K	$P_{gauge} = 2500$ Pa $Y_{CH_4} = 1$
	outlet	pressure-outlet	Backflow $T = 300$ K	$P_{gauge} = 0$ Pa
	wall-bell	wall	Conjugate Heat Transfer	$\epsilon = 1$
	wall-pot (int.)	wall	Convection (water)	$T_\infty = 373$ K
	wall-pot (ext.)	wall	Conjugate Heat Transfer	$\epsilon = 0.3$
	wall-burner	wall	Fixed $T = 500$ K	$\epsilon = 0.5$
	wall-bottom	wall	Convection (air)	$T_\infty = 410$ K $\epsilon = 0.5$
EFFICIENCY	inlet-air	pressure-inlet	Inlet $T = 404$ K	$P_{gauge} = 0$ Pa $Y_{O_2} = 0.233$
	inlet-fuel	pressure-inlet	Inlet $T = 404$ K	$P_{gauge} = 1421$ Pa $Y_{CH_4} = 1$
	outlet	pressure-outlet	Backflow $T = 300$ K	$P_{gauge} = 0$ Pa
	wall-pot (int.)	wall	Convection (water)	$T_\infty = 363$ K
	wall-pot (ext.)	wall	Conjugate Heat Transfer	$\epsilon = 0.3$
	wall-burner	wall	Fixed $T = 500$ K	$\epsilon = 0.5$
	wall-bottom	wall	Convection (air)	$T_\infty = 404$ K $\epsilon = 0.5$

2.3 Results and discussion

2.3.1 Laminar flame speed

Experimental and computationally obtained LFS values are compared in Figure 2.5. As for the global mechanisms, only JL-mod is able to achieve a numerical solution during the 1-D flame simulation. However, it clearly overpredicts the experimental values all over the analyzed range, with greater discrepancies on the fuel-rich mixture side.

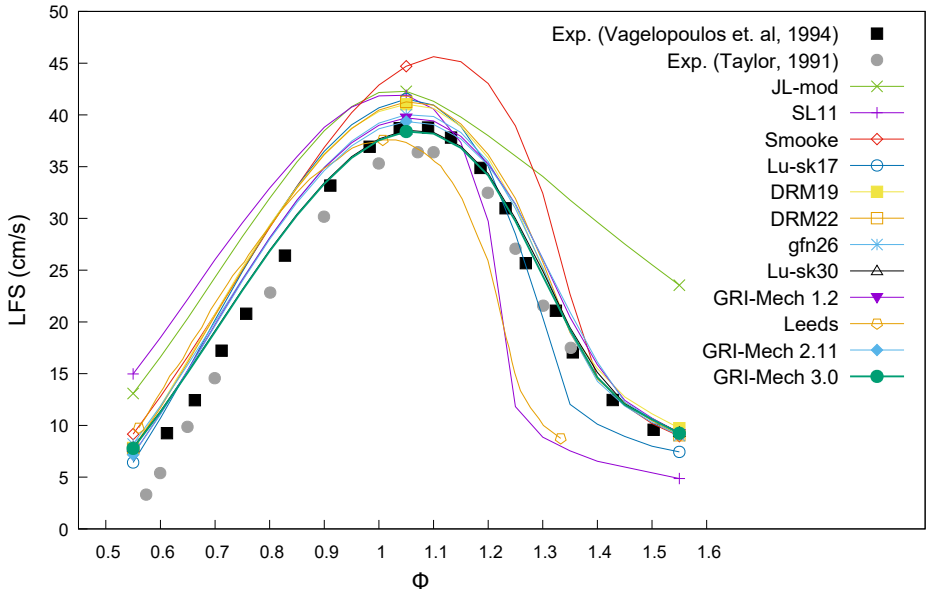

Figure 2.5: Experimental and computationally obtained LFS values at different equivalence ratios.

Apart from that, skeletal Smooke presents a wide deviation for the equivalence ratio range $1.0 < \Phi < 1.4$, while detailed Leeds (results directly obtained from [57]) underpredicts burning velocity in that range. The SL11 mechanism shows low accuracy, with an evident overprediction on the fuel-lean mixture side and the opposite behavior on the fuel-rich one. The rest of skeletal mechanisms, obtained from GRI-Mech versions (1.2 and 3.0), present good accuracy compared with detailed chemistry, however all

of them show a slight overprediction for lean mixtures in comparison with experimental data. These discrepancies may influence the flame front shape and location in CFD calculations, depending on local mixture conditions.

2.3.2 Temperature and major species in the laminar partially premixed flame

This section presents the results regarding the laminar, partially premixed Yale flame analysis. Figure 2.6 depicts the evolution of temperature and CH_4, O_2 and CO_2 concentration along the center axle of the flame (limited to flame zone, Figure 2.2). Reported experimental values of temperature have an absolute uncertainty of ± 50 K, while a 30% absolute error is expected in species concentration measurements [89].

2Steps and JL-mod mechanisms are not included in the comparison because their simulations produce a false flashback up the mixing tube. This behavior may be related to the faster propagation of the flame front as is observed for JL-mod in Figure 2.5. Detailed Leeds mechanism is also omitted since it leads to several numerical errors during its simulation and no converged solution is achieved.

As shown in Figure 2.6, global mechanisms 1Step and JL present a poor prediction both in temperature and chemical species, resulting in an incorrect location of the flame front. This fact also agrees with the findings mentioned in the previous paragraph about the fast reaction spreading predicted by this type of mechanisms. Referring to skeletal and detailed options, they properly capture the flame front, the axial slope of the temperature profile and the location of the depletion zones for O_2 and CH_4 along the centerline. Great deviations of these species concentration near the inlet (mainly O_2) might be a consequence of some experimental errors as pointed out by Bennett et. al [89]. Among these profiles, simulation results coming from Smooke and Lu-sk17 mechanisms are slightly inaccurate compared to the rest of skeletal and detailed options. This mismatching in the flame front location is again correlated with higher values of LFS close to stoichiometric conditions (Figure 2.5).

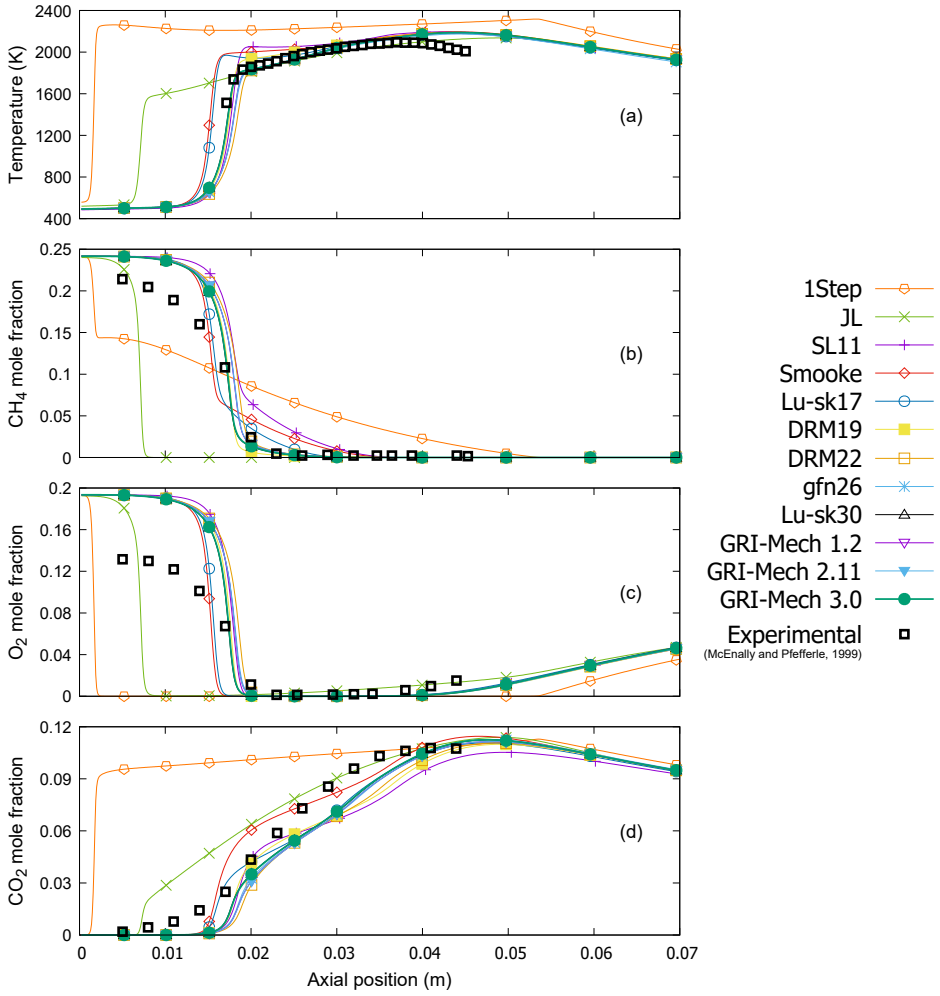

Figure 2.6: Comparison of simulation results and experimental measurements of axial (a) temperature, (b) CH_4, (c) O_2 and (d) CO_2 mole fraction.

Although there is no CO concentration available experimental data for this flame, its concentration profile along the center axle of the flame is computationally obtained and shown in Figure 2.7. Comparison with detailed chemistry shows that global mechanism JL, aside from mispredicting the flame front, greatly overpredicts CO formation, having

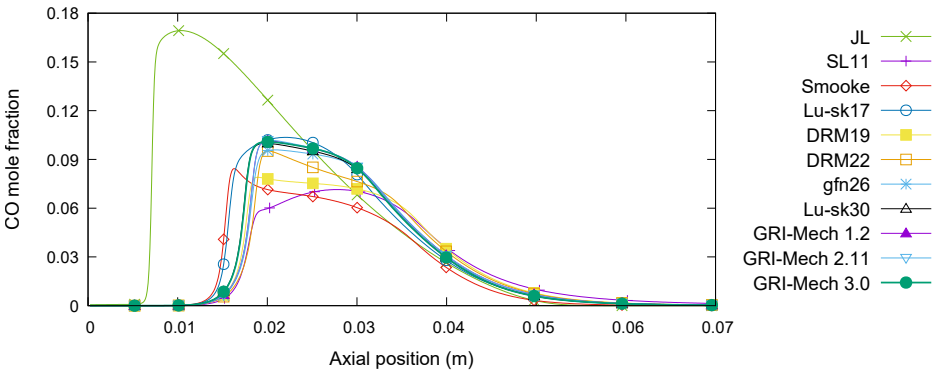

Figure 2.7: Predicted CO concentration profiles along the center axle of the Yale flame.

a faster depletion with similar levels at the end of the flame. Skeletal SL11, Smooke, DRM19, and, to a lesser extent, DRM22 and gfn26 underestimate the CO peak, whereas Lu-sk17 determines a close maximum concentration although with a slightly advanced flame front. Lu-sk30 shows a very good agreement with detailed chemistry for this and all the above parameter comparisons of this flame. In general, skeletal and detailed options adequately predict the trends and changes of reaction zones given by temperature and CO concentration, as can be observed in Figure 2.8.

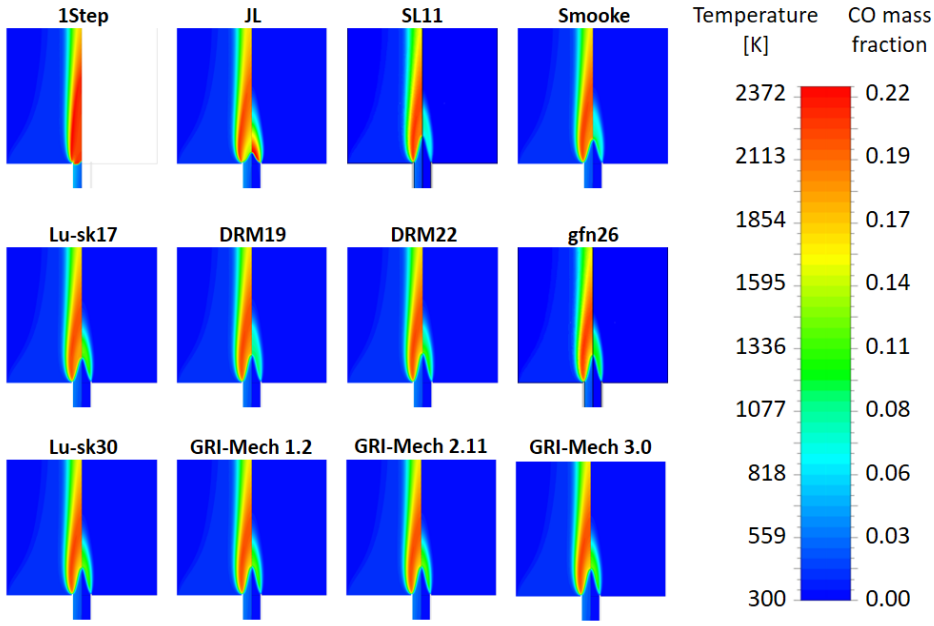

Figure 2.8: Temperature (left) and CO mass fraction (right) contours in the Yale flame.

2.3.3 Emissions and thermal efficiency of a domestic gas cooking burner

Results of the 3-D simulations of the Rapid Burner slice are presented in this section. Table 2.6 summarizes the main operational parameters of the 2.8kW Rapid Burner. For all the cases, numerically predicted mean equivalence ratio and velocity magnitude at the ports (from the combustion test) are practically on the same value. Besides, there is a good agreement between numerical and the experimental value of Φ_{port}, which means that the turbulent air entrainment process and the mixing are properly predicted when no reactions take place and only fuel and air are present in the computational domain.

Table 2.6: Overall Results of 3-D Simulations and Laboratory of the BSH 2.8 kW Rapid Burner.

Mechanism	Φ_{port}	v_{port} (m/s)	**COAF (ppm)**	**Efficiency (%)**	**Speed-up**
1Step	1.770	4.830	-	**61.68**	27.1
2Steps	1.770	4.828	**4685.5**	**59.25**	22.9
JL	1.771	4.824	**0.075**	**62.32**	15.1
SL11	1.768	4.828	**57.58**	**63.61**	10.1
Smooke	1.770	4.826	**51.36**	**63.05**	7.2
Lu-sk17	1.769	4.828	**31.12**	**63.19**	4.8
DRM19	1.770	4.827	**38.59**	**62.98**	2.9
DRM22	1.770	4.827	**42.72**	**63.03**	2.4
gfn26	1.771	4.824	**53.86**	**62.95**	2.3
Lu-sk30	1.770	4.827	**51.43**	**62.96**	2.1
GRI-Mech 1.2	1.770	4.827	**42.88**	**63.02**	2.0
GRI-Mech 2.11	1.770	4.827	**34.25**	**63.00**	1.1
GRI-Mech 3.0	1.770	4.827	**35.21**	**63.01**	-
Laboratory	1.72	-	**25.57**	**63.5**	

As for thermal efficiency values, they are computationally obtained according to Equation 2.3 and compared with the BSH laboratory data (calculated by means of Equation 2.2). Results show that there is a good

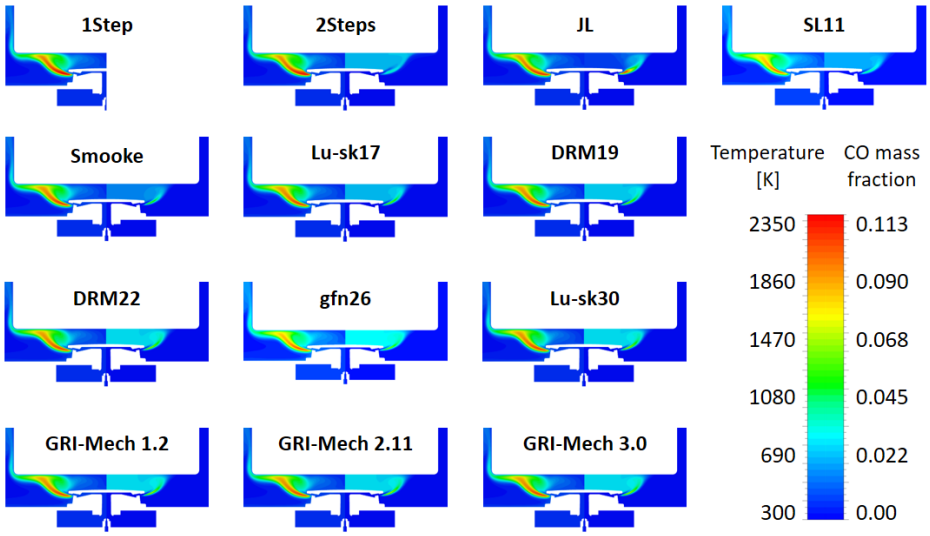

Figure 2.9: Temperature (left) and CO mass fraction (right) contours in the BSH 2.8kW Rapid Burner.

agreement among all predictions, with a slight deviation when using global mechanisms, and the experimental value. This suggests that the heat release and the later heat transfer processes are globally well predicted. Uniformity in efficiency prediction can be also corroborated when observing temperature fields in Figure 2.9, with an alike flame shape for all the cases.

Regarding COAF, calculated as in Equation 2.1, it can be observed that global mechanisms are not suitable to predict it. The rest of analyzed options are in good accordance with detailed chemistry and the experimental measurement, taking into consideration the small concentration of CO (ppm order) produced and the sensitivity of any geometrical or environmental parameter. In general, this agreement can be also reinforced when observing CO mole fraction contour distribution in Figure 2.9. It is important to remark that, for all the latest cases, COAF is far from the threshold value of 1000 ppm [11].

Further analyzing these results, it can be noted that they do not fully follow the trends from those obtained in the Yale Flame regarding CO.

Differences are specially remarkable for the Lu-sk30 mechanism, which has previously shown the best performance in the prediction of variables analyzed in the 1-D and 2-D cases (confirmed with statistical evaluation presented in the next section), but slightly deviates in this calculation. To explain this behavior, the evolution of relevant variables involved in COAF calculation is checked throughout the 3-D domain of the gas burner configuration. Three vertical and two horizontal lines (shown in Figure 2.10a) are selected to monitor Temperature and CO mole fraction for Lu-sk30 and GRI-Mech 3.0 mechanisms.

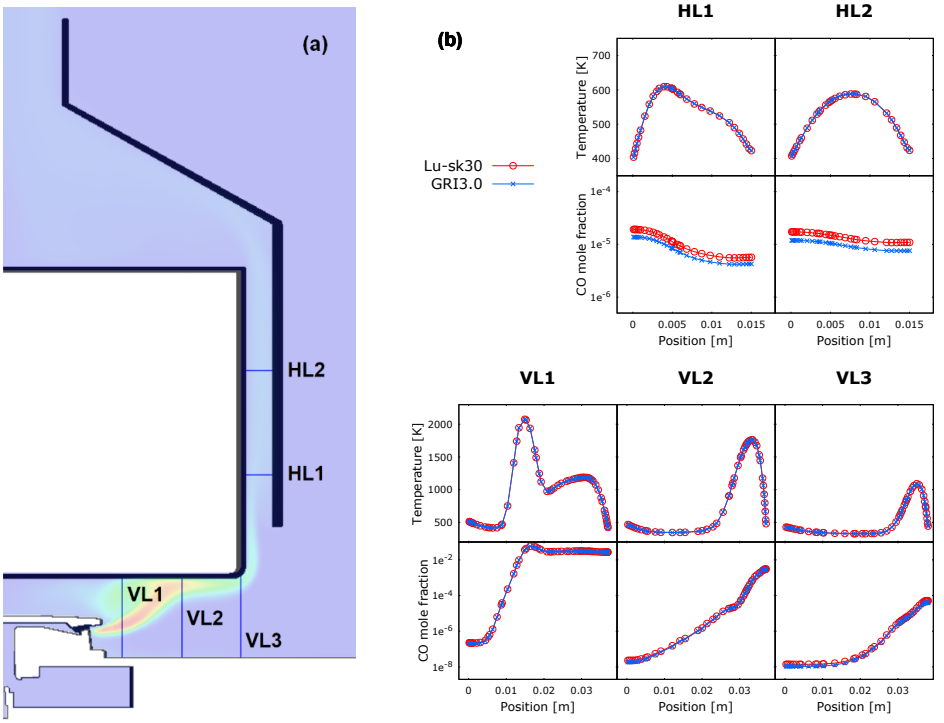

Figure 2.10: Selected vertical and horizontal lines location (a) and temperature and CO mole fraction profiles along them (b).

Figure 2.10b shows that differences in temperature fields of both mechanisms are not responsible for the COAF deviation of Lu-sk30

mechanism (in fact, a deeper analysis showed a 10 K maximum difference in the whole domain). This behavior is in accordance with temperature profiles obtained in the 2-D configuration (Figure 2.6a). Additional analysis are made using other variables which might have an influence in COAF calculation (major species mole fraction and net production, heat of reaction, mixture fraction) with similar results. Therefore, it can be concluded that the Lu-sk30 deviation in COAF calculation is not occasioned by none of these variables but differences of kinetics description itself. Figure 2.10b shows that CO production in the early and middle stages of the flame (VL1, VL2) is identically captured by both mechanisms. However, in the latter part of the flame (VL3), where most CO is consumed, there exists a slight difference that is subsequently reflected in horizontal lines (HL1, HL2) and hence in COAF measurement (at the top of the domain). These results indicate that both mechanisms agree in CO production but differ in its last stages of consumption, which might be explained by going deeper in the kinetics. The 27 CO chemical reactions present in the GRI-Mech 3.0 mechanism that were omitted in the creation of the Lu-sk30 mechanism (see Appendix 2.B) may be responsible for the differences in CO consumption and hence the deviation in COAF with reference to detailed chemistry.

The final choice of using a specific mechanism needs to be also motivated by the computational load of the selected option. Table 2.6 includes the speed-up, defined as the ratio between simulation CPU time of the calculations with GRI-Mech 3.0 and the corresponding mechanism. With these data, it can be stated that global mechanisms are fast suitable options if the analysis involves only the overall thermal efficiency, but never for COAF evaluation. If local computational resources and/or time constrains in the design process are limited, skeletal mechanisms such as SL11 or Smooke are good options to analyze trends in CO emissions, whereas Lu-sk17 shows to be an optimal choice if more accuracy is required in the prediction.

2.3.4 Statistical evaluation of accuracy

In order to quantify a global accuracy of the analyzed mechanisms, the root mean square error (RMSE, [92]) is proposed:

$$RMSE = \sqrt{\frac{1}{N}\sum_{i=1}^{N}(y_i - \hat{y}_i)^2}\ , \tag{2.4}$$

where y_i represents the reference value, $\hat{y}_i$ is the predicted value, and N is the number of sampling points. The closer to 0 this value is, the better accuracy of the analyzed mechanism.

RMSE values are obtained for LFS (1-D) and temperature and major species (2-D, 3-D) predictions, splitting the evaluation in two subsections depending on the reference data: experimental (profiles not available for the 3-D configuration) and detailed chemistry (GRI-Mech 3.0). As for major species, RMSE values are averaged in a single 'Species' ranking. Besides, calculations for the five different locations analyzed in the 3-D gas burner configuration (Figure 2.10a) are also averaged. For numerical complete values of RMSE, the reader is referred to Appendix 2.C. Finally, mechanisms are ranked from highest to lowest averaged accuracy at each column.

Table 2.7 shows the ranking of mechanisms taking experimental data as reference. It can be observed that skeletal Lu-sk30 ranks first places swapping position mainly with the detailed GRI-Mech 3.0 mechanism. In the case of temperature, it is surprising that global mechanism JL ranks the first place. This is due to the clustering of thermocouple measurements after the flame front in the experiments, with a clear lack of data in the reaction zone (Figure 2.6a), which biases the RMSE calculation. In general, ranking might be likely altered due to uncertainty and errors in experimental measurements.

Table 2.7: Ranking of mechanisms based on the accuracy with available experimental data as values of reference.

Rank	LFS	Temperature (2-D)	Species (2-D)
1	GRI-Mech 3.0	JL*	Lu-sk30
2	Lu-sk30	Lu-sk30	GRI-Mech 3.0
3	GRI-Mech 2.11	GRI-Mech 3.0	Smooke
4	gfn26	DRM19	Lu-sk17
5	GRI-Mech 1.2	Lu-sk17	DRM19
6	DRM19	GRI-Mech 1.2	gfn26
7	DRM22	GRI-Mech 2.11	GRI-Mech 1.2
8	Lu-sk17	Smooke	GRI-Mech 2.11
9	Smooke	gfn26	DRM22
10	Leeds	SL11	SL11
11	SL11	DRM22	JL
12	JL-mod	1Step	1Step

* Due to the clustering of thermocouple measurements after the flame front.

The ranking is also consistent with results from Table 2.8, where detailed chemistry data are taken as reference. Lu-sk30 fills the first position in all the cases, even over the older versions of GRI-Mech. On the other hand, global mechanisms hold the latest places in all the comparisons.

Table 2.8: Ranking of mechanisms based on the accuracy with detailed GRI-Mech 3.0 calculations as values of reference.

Rank	LFS	Temperature (2-D)	Species (2-D)	Temperature (3-D)	Species (3-D)
1	Lu-sk30	Lu-sk30	Lu-sk30	Lu-sk30	Lu-sk30
2	GRI-Mech 2.11	DRM19	DRM19	GRI-Mech 1.2	GRI-Mech 1.2
3	gfn26	GRI-Mech 1.2	GRI-Mech 1.2	GRI-Mech 2.11	DRM22
4	GRI-Mech 1.2	GRI-Mech 2.11	GRI-Mech 2.11	DRM22	GRI-Mech 2.11
5	DRM19	gfn26	gfn26	DRM19	DRM19
6	DRM22	SL11	DRM22	gfn26	gfn26
7	Lu-sk17	DRM22	Lu-sk17	Smooke	Lu-sk17
8	Smooke	Lu-sk17	SL11	Lu-sk17	Smooke
9	Leeds	Smooke	Smooke	SL11	SL11
10	SL11	JL	JL	JL	JL
11	JL-mod	1Step	1Step	1Step	2Steps
12				2Steps	1Step

These results reinforce the selection of the GRI-Mech 3.0 mechanism as a suitable reference for chemistry calculation in combustion simulations involving CH_4, and the limitations of global mechanisms to properly capture all the associated phenomena.

2.4 Conclusions

In this chapter, global, skeletal and detailed chemical reaction mechanisms for the simulation of methane-air combustion are evaluated under operating conditions such as those present in domestic gas cooking burners. Variables to be evaluated comprise laminar flame speed in a 1-D laminar premixed flame, temperature and chemical species in a 2-D partially premixed flame, and thermal efficiency and pollutant emissions in a 3-D domestic gas cooking burner, according to certification requirements for this technology. The following conclusions can be stated from this study.

1. Global mechanisms clearly show not to be suitable to compute laminar flame speed values because they give completely inaccurate results or are unable to get a numerical converged solution. JL-mod, the only one that achieves a solution, predicts greater speed values all over the mixture range analyzed. Skeletal and detailed mechanisms match well with LFS experimental profiles, with slight deviations over the mixture lean side. Greater discrepancies are shown by those mechanisms not based on GRI-Mech versions, namely, skeletal Smooke and detailed Leeds, mainly in the rich side.

2. In the 2-D partially premixed flame, global mechanisms generally tend to produce a false flashback up the mixing tube, which is in accordance with the faster upstream propagation of the flame front. Likewise, global JL overpredicts CO formation in the forward flame front, with a greater consumption in the rest of the flame zone. Skeletal and detailed mechanisms properly capture the flame features and emissions, with slight deviations of the flame front for Smooke and Lu-sk17, and small underprediction of axial CO peak for skeletal SL11, Smooke, gfn26,

and DRM mechanisms. Lu-sk30 shows an excellent agreement with detailed chemistry in temperature and species distribution for this configuration.

3. Numerical simulations of the 3-D domestic gas cooking burner show that, for thermal efficiency determination, even global mechanisms could be good options if mixture and flow characteristics at burner ports assure a numerical stability far from flashback conditions (as predictions from the rest of configurations exhibit). However, if CO emissions prediction is the target of the analysis, global mechanisms are fully inadequate. For this last purpose, skeletal mechanisms are in general good options to surrogate detailed chemistry in terms of accuracy. Yet, computational load needs to be considered in order to select one mechanism. If resources are limited, the simplest skeletal mechanisms, i.e., SL11 and Smooke mechanisms, present as good alternatives, with the greatest speed-up. If a higher accuracy is required, skeletal Lu-sk17 shows to be the optimal option to predict CO emissions in this configuration with moderate computing time. Further analysis show that the small deviation observed for skeletal Lu-sk30 in this calculation is due to kinetics itself.

4. A global statistical evaluation is proposed by means of the quantification of RMSE values. The Lu-sk30 mechanism, which was created starting from the detailed GRI-Mech 3.0, appears to be the best alternative to detailed chemistry in predicting the evolution of variables of interest (LFS, temperature and chemical species). On the other side, global mechanisms are confirmed as the worst ones. In the middle zone, the skeletal mechanism choice needs to weigh accuracy and computational load depending on the simulation resources and targets.

5. Apart from analyzing the available chemical reaction mechanisms for methane combustion, a new skeletal option is successfully created: the SL11 mechanism is obtained after a reduction and an optimization

process, and shows reasonably good results given its size. In fact, this mechanism is currently used in simulations to avoid large associated computational times, which require higher speed-ups than those obtained with other skeletal and frequently employed options such as the Smooke mechanism.

2.A SL11 mechanism

The development process of the SL11 mechanism is described in this appendix. The initial goal was to obtain a skeletal model smaller than the Smooke mechanism, which is formed by 16 species and 35 reactions [50], with a reasonable performance in temperature and carbon monoxide predictions. A reduction and an optimization process are carried out.

For the reduction process, detailed GRI-Mech 3.0 is selected as the starting mechanism, which comprises 53 species and 325 reactions [48]. First, the faster directed relation graph (DRG [61]), directed relation graph with error propagation (DRGEP [62]), and directed relation graph with path flux analysis (DRGPFA [63]) are applied, alternating between them until they do not reduce the mechanism any further. Then, the more powerful but compute-intensive DRG-aided with sensitivity analysis [52, 64] (DRGASA), DRG with error propagation and sensitivity analysis [65] (DRGEPSA), and DRG with path flux and sensitivity analysis (DRGPFASA) are employed, alternating between them and the former faster options until no further reduction is possible. Finally, a full species sensitivity analysis (FSSA) based reduction method is applied, followed by another iteration of all the techniques. The complete sequence is shown in Figure 2.11.

The selected model for the reduction is a one-dimensional, partially premixed, freely propagating flame. With it, flame speed calculations can be obtained, which is an important property for flame stability. Given that the aim of the process is to develop a mechanism suitable for methane-air combustion, pure methane is selected as the fuel composition. The calculations are carried out using 500 K as the temperature of the unburnt mixture, which is a similar value as the temperature of the gases in a domestic gas burner port. An aeration rate of $\lambda = 0.8$ is employed. Due to the importance of temperature and carbon monoxide emissions in the design and operation of domestic gas cooking burners, both are the target flame properties chosen to drive the mechanism reduction methods. Relative tolerances of 10% and 50% are selected for maximum temperature and CO mole fraction at the end of the domain (endpoint) respectively.

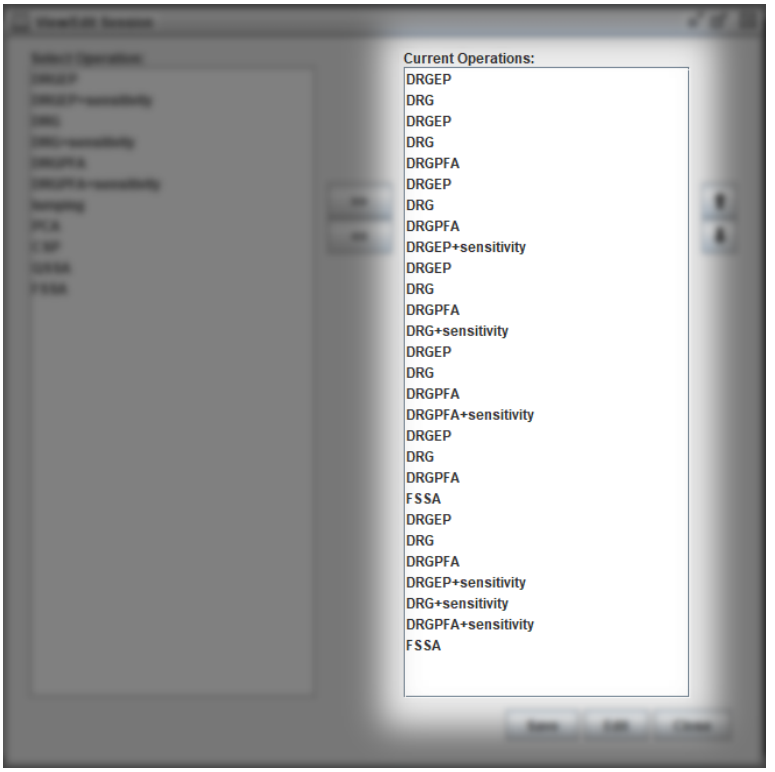

Figure 2.11: Sequence of techniques employed in the reduction process.

Table 2.9: Summary of the reduction process for the creation of the SL11 mechanism.

	No. Species	No. Reactions	Reduction technique	Error in temperature (maximum)	Error in CO mole fraction (endpoint)
Original mechanism	53	325	-	-	-
Successful step 1	20	102	DRGEP	0.02%	0.15%
Successful step 2	17	69	DRGPFA	0.25%	0.45%
Successful step 3	16	67	DRGEP	0.30%	0.50%
Successful step 4	11	19	FSSA	1.35%	0.20%

Table 2.9 shows the results for each successful reduction step. The first DRGEP operation provides the greatest reduction, producing a mechanism with 20 species. Then, DRGPFA succeeds in reducing the number of species, generating a 17 species mechanism. The next operation that decreases that number is DRGEP, removing one species. The last method that achieves a greater reduction is the FSSA, producing the final mechanism formed by 11 species and 19 reactions. Further reduction operations yield no positive results since removing additional species produces errors greater than the selected tolerances.

After the reduction, an optimization process is carried out. This step has been possible thanks to a collaboration with the *gfn* group (University of Zaragoza, Spain), headed by Prof. Norberto Fueyo. The MUM-PCE technique [93] is employed to modify reaction rate coefficients and optimize the performance of the mechanism in terms of laminar flame speed.

The final mechanism, referred to in this study as the SL11 mechanism, is shown in Table 2.10.

Table 2.10: Skeletal SL11 mechanism. Rate coefficients in the form $k_f = AT^{\beta}\exp(-E_a/RT)$. Units are: cal, mol, cm, s, K.

N.	Reaction	A	β	E_a
1.	2 O + M ⇔ O_2 + M[a]	1.21E+17	-1	0
2.	H + O + M ⇔ OH + M[b]	5.07E+17	-1	0
3.	H_2 + O ⇔ H + OH	3.24E+04	2.7	6260
4.	CH_4 + O ⇔ CH_3 + OH	7.07E+08	1.5	8600
5.	CO + O (+ M) ⇔ CO_2 (+ M)[c]	1.83E+10	0	2385
	Low pressure limit: 6.02E+14	0	3000	
6.	CO + O2 ⇔ CO_2 + O	2.50E+12	0	47800
7.	H + O2 ⇔ O + OH	4.33E+16	-0.671	17041
8.	2 H + M ⇔ H_2 + M[d]	1.01E+18	-1	0
9.	2 H + H_2 ⇔ 2 H_2	9.00E+16	-0.6	0
10.	2 H + H_2O ⇔ H_2 + H_2O	6.00E+19	-1.25	0
11.	CO_2 + 2 H ⇔ CO_2 + H_2	5.50E+20	-2	0
12.	H + OH + M ⇔ H_2O + M[e]	2.65E+22	-2	0
13.	CH_3 + H (+ M) ⇔ CH_4 (+ M)[f]	1.28E+16	-0.534	536
	Low pressure limit: 2.62E+33	-4.76	2440	
	TROE centering: 0.783 74	2941	6964	
14.	CH_4 + H ⇔ CH_3 + H_2	5.03E+08	1.62	10840
15.	H_2 + OH ⇔ H + H_2O	1.90E+08	1.51	3430
16.	2 OH ⇔ H_2O + O	3.47E+04	2.4	-2110
17.	CH_4 + OH ⇔ CH_3+ H_2O	7.18E+07	1.6	3120
18.	CO + OH ⇔ CO_2 + H	1.63E+07	1.228	70
19.	CH_3 + O ⇒ CO + H + H_2	3.71E+13	0	0

[a] Third body efficiencies: H_2=2.4; CH_4=2.0; H_2O=15.4; CO_2=3.6; CO=1.75

[b] Third body efficiencies: H_2=2.0; CH_4=2.0; H_2O=6.0; CO_2=2.0; CO=1.5

[c] Third body efficiencies: CO_2=3.5; CO=1.5; H_2=2.0; H_2O=6.0; CH_4=2.0; O2=6.0

[d] Third body efficiencies: H_2=0.0; H_2O=0.0; CO_2=0.0; CH_4=2.0

[e] Third body efficiencies: H_2=0.73; H_2O=3.65; CH_4=2.0

[f] Third body efficiencies: H_2=2.0; CH_4=3.0; H_2O=6.0; CO_2=2.0; CO=1.5

2.B Differences between Lu-sk30 and GRI-Mech 3.0 CO kinetics

Table 2.11 recapitulates the CO chemical reactions which were suppressed from the GRI-Mech 3.0 mechanism in the obtention of the Lu-sk30 mechanism.

Table 2.11: CO chemical reactions present in GRI-Mech 3.0 but not in Lu-sk30.
Rate coefficients in the form $k_f = AT^{\beta}\exp(-E_a/RT)$. Units are: cal, mol, cm, s, K.

Reaction	A	β	E_a
C + NO ⇔ **CO** + N	2.90E+13	0	0
C_2H + O_2 ⇔ HCO + **CO**	1.00E+13	0	-755
CH_3 + CH_3CHO ⇒ CH_3 + CH_4 + **CO**	2.72E+06	1.77	5920
CN + O ⇔ **CO** + N	7.70E+13	0	0
H + CH_2CO ⇔ CH_3 + **CO**	1.13E+13	0	3428
H + CH_3CHO ⇒ CH_3 + H_2 + **CO**	2.05E+09	1.16	2405
HCCO + NO ⇔ HCNO + **CO**	9.00E+12	0	0
HCN + O ⇔ NH + **CO**	5.07E+03	2.64	4980
HCN + OH ⇔ NH_2 + **CO**	1.60E+02	2.56	9000
HCNN + O ⇔ **CO** + H + N_2	2.20E+13	0	0
HCNO + H ⇔ NH_2 + **CO**	1.70E+14	-0.75	2890
HNCO + H ⇔ NH_2 + **CO**	2.25E+07	1.7	3800
HNCO + M ⇔ NH + **CO** + M	1.18E+16	0	84720
HNCO + O ⇔ HNO + **CO**	1.50E+08	1.57	44000
HO_2 + CH_3CHO ⇒ CH_3 + H_2O_2 + **CO**	3.01E+12	0	11923
N + CO_2 ⇔ NO + **CO**	3.00E+12	0	11300
NCO + H ⇔ NH + **CO**	5.40E+13	0	0
NCO + M ⇔ N + **CO** + M	3.10E+14	0	54050
NCO + N ⇔ N_2 + **CO**	2.00E+13	0	0
NCO + NO ⇔ N_2O + **CO**	1.90E+17	-1.52	740
NCO + O ⇔ NO + **CO**	2.35E+13	0	0
NCO + OH ⇔ NO + H + **CO**	2.50E+12	0	0
NH + CO_2 ⇔ HNO + **CO**	1.00E+13	0	14350
O + C_2H ⇔ CH + **CO**	5.00E+13	0	0
O + CH_3CHO ⇒ OH + CH_3 + **CO**	2.92E+12	0	1808
O_2 + CH_3CHO ⇒ HO_2 + CH_3+ **CO**	3.01E+13	0	39150
OH + CH_3CHO ⇒ CH_3 + H_2O + **CO**	2.34E+10	0.73	-1113

2.C Root Mean Square Error numerical values

Table 2.12: Numerical RMSE values taking available experimental data as values of reference (1-D and 2-D configurations).

Mechanism	LFS	Temperature	CH_4	O_2	CO_2	CO
1Step	-	2.81E+02	4.84E-02	6.78E-02	5.65E-02	-
2Steps	-	-	-	-	-	-
JL	-	6.52E+01	8.77E-02	5.87E-02	1.51E-02	-
JL-mod	9.11E+00	-	-	-	-	-
SL11	8.56E+00	1.40E+02	3.59E-02	4.17E-02	1.46E-02	-
Smooke	6.15E+00	1.38E+02	2.56E-02	3.84E-02	9.02E-03	-
Lu-sk17	3.35E+00	1.20E+02	2.48E-02	3.91E-02	9.86E-03	-
DRM19	3.15E+00	1.01E+02	2.42E-02	3.86E-02	1.30E-02	-
DRM22	3.15E+00	1.76E+02	2.85E-02	4.16E-02	1.42E-02	-
gfn26	2.51E+00	1.38E+02	2.64E-02	4.01E-02	1.27E-02	-
Lu-sk30	1.88E+00	8.05E+01	2.23E-02	3.67E-02	1.14E-02	-
GRI-Mech 1.2	2.55E+00	1.36E+02	2.64E-02	4.00E-02	1.28E-02	-
Leeds	6.85E+00	-	-	-	-	-
GRI-Mech 2.11	2.51E+00	1.38E+02	2.65E-02	4.01E-02	1.29E-02	-
GRI-Mech 3.0	1.79E+00	8.19E+01	2.25E-02	3.69E-02	1.15E-02	-

Table 2.13: Numerical RMSE values taking detailed GRI-Mech 3.0 calculations as values of reference (1-D and 2-D configurations).

Mechanism	LFS	Temperature	CH_4	O_2	CO_2	CO
1Step	-	8.80E+02	5.98E-02	9.45E-02	5.67E-02	-
2Steps	-	-	-	-	-	-
JL	-	4.30E+02	9.16E-02	7.31E-02	2.00E-02	6.61E-02
JL-mod	8.44E+00	-	-	-	-	-
SL11	7.78E+00	7.41E+01	2.19E-02	7.41E-03	5.14E-03	1.56E-02
Smooke	4.83E+00	1.95E+02	1.97E-02	2.31E-02	1.12E-02	1.72E-02
Lu-sk17	2.94E+00	1.69E+02	1.42E-02	2.00E-02	4.41E-03	9.85E-03
DRM19	1.86E+00	3.77E+01	2.65E-03	2.78E-03	3.15E-03	1.01E-02
DRM22	1.91E+00	8.77E+01	1.37E-02	1.29E-02	3.11E-03	8.87E-03
gfn26	1.12E+00	5.96E+01	8.90E-03	8.58E-03	1.58E-03	5.65E-03
Lu-sk30	1.90E-01	2.93E+00	4.86E-04	4.35E-04	1.19E-04	6.13E-04
GRI-Mech 1.2	1.13E+00	5.44E+01	8.51E-03	8.05E-03	1.88E-03	4.55E-03
Leeds	6.13E+00	-	-	-	-	-
GRI-Mech 2.11	1.04E+00	5.56E+01	8.71E-03	8.23E-03	1.92E-03	4.65E-03
GRI-Mech 3.0	-	-	-	-	-	-

Table 2.14: Temperature numerical RMSE values taking detailed GRI-Mech 3.0 calculations as values of reference (3-D configuration).

	Temperature				
Mechanism	VL1	VL2	VL3	HL1	HL2
1step	6.85E+01	3.16E+01	6.44E+00	2.38E+01	8.78E+00
2steps	1.00E+02	1.91E+01	1.66E+01	7.94E+00	5.58E+00
JL	8.56E+01	2.70E+01	4.14E+00	3.40E+00	3.88E+00
JL-mod	-	-	-	-	-
SL11	8.08E+01	1.78E+01	4.45E+00	5.26E+00	2.36E+00
Smooke	3.44E+01	8.72E+00	1.73E+00	2.25E+00	1.20E+00
Lu-sk17	4.56E+01	1.34E+01	3.53E+00	4.12E+00	2.09E+00
DRM19	1.17E+01	2.41E+00	5.05E-01	5.22E-01	1.90E-01
DRM22	5.91E+00	2.25E+00	6.48E-01	1.09E+00	4.11E-01
gfn26	9.60E+00	9.09E+01	2.21E+00	2.13E+00	2.38E+00
Lu-sk30	1.29E+00	1.05E+00	1.27E-01	6.81E-01	1.80E-01
GRI-Mech 1.2	4.97E+00	2.09E+00	5.11E-01	7.29E-01	1.15E-01
Leeds	-	-	-	-	-
GRI-Mech 2.11	5.02E+00	1.96E+00	1.59E-01	1.13E+00	2.20E-01
GRI-Mech 3.0	-	-	-	-	-

Table 2.15: CH_4 numerical RMSE values taking detailed GRI-Mech 3.0 calculations as values of reference (3-D configuration).

	CH_4				
Mechanism	VL1	VL2	VL3	HL1	HL2
1step	1.77E-02	2.10E-03	7.44E-06	9.18E-07	7.99E-06
2steps	1.11E-02	8.36E-04	1.06E-05	5.45E-06	6.39E-06
JL	8.40E-03	4.43E-08	3.43E-13	1.20E-13	1.17E-13
JL-mod	-	-	-	-	-
SL11	1.29E-02	6.14E-05	1.39E-10	4.52E-12	3.34E-12
Smooke	8.00E-03	1.35E-05	1.08E-09	4.98E-10	5.30E-10
Lu-sk17	7.99E-03	2.54E-07	1.99E-12	7.22E-13	7.02E-13
DRM19	4.37E-04	9.91E-07	8.03E-12	2.48E-12	2.84E-12
DRM22	2.56E-04	8.27E-08	1.28E-12	4.88E-13	5.46E-13
gfn26	5.23E-04	1.77E-07	5.07E-12	1.89E-12	2.14E-12
Lu-sk30	1.43E-04	7.05E-10	5.87E-13	2.63E-13	3.09E-13
GRI-Mech 1.2	2.90E-04	3.10E-08	1.57E-13	3.16E-14	2.63E-14
Leeds	-	-	-	-	-
GRI-Mech 2.11	3.08E-04	3.20E-08	2.29E-13	7.20E-14	7.28E-14
GRI-Mech 3.0	-	-	-	-	-

Table 2.16: O_2 numerical RMSE values taking detailed GRI-Mech 3.0 calculations as values of reference (3-D configuration).

	O_2				
Mechanism	VL1	VL2	VL3	HL1	HL2
1step	4.64E-03	2.22E-03	2.03E-03	8.39E-03	1.37E-03
2steps	1.16E-02	2.68E-03	1.14E-03	2.75E-04	5.42E-04
JL	1.11E-02	3.79E-03	1.38E-03	2.50E-04	1.94E-04
JL-mod	-	-	-	-	-
SL11	1.24E-02	2.40E-03	3.80E-04	5.68E-04	8.38E-04
Smooke	6.32E-03	8.80E-04	5.96E-05	4.51E-04	6.53E-05
Lu-sk17	8.09E-03	1.26E-03	1.20E-04	6.77E-04	2.44E-04
DRM19	5.37E-04	1.55E-04	1.21E-04	1.48E-04	1.89E-04
DRM22	5.53E-04	1.66E-04	1.98E-04	3.07E-04	1.57E-04
gfn26	8.19E-04	9.33E-03	1.81E-04	3.72E-04	6.63E-04
Lu-sk30	1.76E-04	1.42E-04	2.09E-05	2.54E-04	2.47E-04
GRI-Mech 1.2	3.51E-04	1.29E-04	1.89E-04	1.44E-04	3.04E-04
Leeds	-	-	-	-	-
GRI-Mech 2.11	3.47E-04	9.81E-05	1.49E-04	3.22E-04	3.90E-04
GRI-Mech 3.0	-	-	-	-	-

Table 2.17: CO_2 numerical RMSE values taking detailed GRI-Mech 3.0 calculations as values of reference (3-D configuration).

	CO_2				
Mechanism	VL1	VL2	VL3	HL1	HL2
1step	1.61E-02	1.37E-03	1.19E-03	4.30E-03	9.57E-04
2steps	9.26E-03	5.80E-03	1.32E-03	1.02E-03	1.21E-03
JL	1.64E-02	2.29E-03	6.90E-04	2.66E-04	1.66E-04
JL-mod	-	-	-	-	-
SL11	2.72E-03	2.69E-03	3.71E-04	3.89E-04	3.91E-04
Smooke	3.31E-03	5.49E-04	5.48E-05	2.70E-04	5.15E-05
Lu-sk17	1.71E-03	7.52E-04	1.22E-04	3.90E-04	9.64E-05
DRM19	3.71E-04	2.27E-04	6.49E-05	8.48E-05	1.00E-04
DRM22	3.10E-04	1.29E-04	8.44E-05	1.65E-04	8.96E-05
gfn26	4.98E-04	4.17E-03	7.07E-05	1.62E-04	3.51E-04
Lu-sk30	1.05E-04	6.27E-05	1.11E-05	1.36E-04	1.33E-04
GRI-Mech 1.2	5.54E-04	1.50E-04	7.08E-05	7.53E-05	1.65E-04
Leeds	-	-	-	-	-
GRI-Mech 2.11	5.85E-04	1.13E-04	5.57E-05	1.69E-04	2.30E-04
GRI-Mech 3.0	-	-	-	-	-

Table 2.18: CO numerical RMSE values taking detailed GRI-Mech 3.0 calculations as values of reference (3-D configuration).

	CO				
Mechanism	VL1	VL2	VL3	HL1	HL2
1step	-	-	-	-	-
2steps	8.98E-03	5.57E-03	1.42E-03	1.13E-03	1.26E-03
JL	9.60E-03	3.63E-04	1.67E-05	9.40E-06	1.01E-05
JL-mod	-	-	-	-	-
SL11	1.10E-02	1.09E-03	3.54E-05	9.55E-06	8.05E-06
Smooke	9.08E-03	1.59E-04	5.63E-06	4.58E-06	5.01E-06
Lu-sk17	5.53E-03	1.75E-04	2.34E-06	1.04E-06	1.12E-06
DRM19	2.45E-03	1.03E-04	4.08E-07	4.13E-07	7.29E-07
DRM22	3.66E-04	8.91E-05	1.38E-06	1.47E-06	1.95E-06
gfn26	7.38E-04	9.50E-05	5.91E-06	4.16E-06	5.03E-06
Lu-sk30	8.11E-05	9.91E-06	4.66E-06	3.57E-06	4.36E-06
GRI-Mech 1.2	3.19E-04	1.01E-04	1.39E-06	1.46E-06	1.96E-06
Leeds	-	-	-	-	-
GRI-Mech 2.11	3.50E-04	8.15E-05	7.24E-07	2.20E-07	3.42E-07
GRI-Mech 3.0	-	-	-	-	-

Chapter 3

Single methane flame burner

This chapter includes the experimental and computational analysis of temperature and carbon monoxide emissions from a single, partially premixed methane flame, perpendicularly impinging onto the bottom wall of a water pot. First, an introduction of the flame-wall interaction phenomena is presented. Then, the state of the art regarding this type of systems is reviewed, highlighting those studies which include pollutants emission data. After that, both the experimental and the computational setup prepared for this work are described, together with the conditions of the programmed tests. Later, experimental and numerical results are discussed, distributed in three different blocks: flow field (non-reactive and reactive), temperature, and carbon monoxide emissions. Finally, an statistical evaluation of the modeling is included, followed by a list of partial conclusions.

3.1 Introduction

Flame-wall interaction (FWI) is a common phenomenon in numerous real applications. The perturbation and quenching of combustion reactions induced by the impingement may lead to undesirable effects in pollutant emissions and heat exchange [13,15]. For example, in domestic gas cooking burners, this interaction is present since the flame interacts with solid bodies such as grills and cooking pots. Thus, pollutant emissions, mainly carbon

monoxide when typically using hydrocarbons as fuel, are increased [14]. At this point, a comprehensive study of CO behavior under FWI conditions is proposed. However, three main issues are related with this kind of analysis using domestic gas cooking burners: (1) their highly complex geometries [21–23]; (2) the difficulty of attaching the required devices without important flow perturbations to the normal performance [24]; and (3) the need to accurately describe chemical kinetics (skeletal or detailed chemistry) to obtain reliable CO data during the numerical calculations, which would entail huge computational times [94].

Therefore, simpler configurations are commonly used to analyze the chemistry and the FWI phenomena that take place during the combustion process. For this purpose, geometrically simpler burners with a single flame (Bunsen-type burner) perpendicularly impinging onto a wall have been frequently employed. This type of configurations can reproduce most of the relevant features and work in representative conditions of those present in domestic gas cooking burners. Furthermore, they afford a detailed definition of operating variables and boundary conditions, which is crucial to subsequently analyze the process through computational fluid dynamics (CFD) simulations.

3.2 Flame-wall interaction: state of the art

A great number of studies regarding the interaction between a single methane flame and a wall have been published. Most of them are focused on the experimental analysis of heat transfer and the influence of parameters such as burner internal geometry [95, 96], burner diameter [97–99], thermal power [100], equivalence ratio [101,102], and burner-to-plate spacing [38, 103, 104]. The effect of these parameters on flame stability was studied by Hsieh and Lin [105], while Hou and Ko [106] and Kuntikana and Prabhu [107] analyzed their combined effect with oblique angle on flame structure, temperature distribution and thermal efficiency. Moreover, Tajik et al. [108] included heat flux distribution under the effect of varying inlet gas temperature. Some of these works are supplemented with CFD

simulations to explain the distribution of the heat flux [98–100, 103, 108]. All the aforementioned studies show that those parameters have a significant influence on heat transfer rate and surely determine the final efficiency of the process. However, only a few investigations include the analysis of pollutant emissions in this type of configurations. Saha et al. [109] carried out some experiments with impinging rich methane and ethylene jet flames, analyzing the effect of Re number, equivalence ratio, and burner-to-plate separation distance on heat transfer and emissions. CO and NO_x concentrations were measured in the flue gas leaving the wall surface. The results show that the CO emission increases when burner-to-plate spacing is lowered, or Re number is increased, since in both situations the combustion do not reach completion within the wall jet region. Other studies [110, 111] carried out CO measurements with laser induced fluorescence (LIF) for variations in impinging methane/air flames at lean, stoichiometric, and rich conditions, comparing their findings to numerical predictions. Chien et al. [112] also utilized LIF to correlate CO emission with variations in the structure of nonpremixed methane/air flames and OH distribution, as a function of burner-to-plate distance. Li et al. [113, 114] and Mishra [115] included CO/NO_x emissions analyses in their studies of a premixed flame jet impinging on a flat wall, varying plate temperature, Re number, equivalence ratio, and nozzle to plate distance, but using liquefied petroleum gases (LPG) as fuel instead of methane.

In all the previous studies, pollutant measurements are performed in the vicinity of the flame, and local single-point data are reported. However, although relevant, these values may greatly differ from those downstream of the impingement zone, which are more interesting to draw conclusions for practical domestic gas burner configurations. According to the European Standard certification [11], the emissions' sample must be captured in the upper part of a hood, in the exhaust gas stream where there is no combustion process and species concentrations have reached a stable value. The present study addresses this issue through a similar configuration as the one used in certification tests of gas cooking burners.

Hence, the proposed analysis aims at providing a deeper insight in the CO formation and its interrelationship with relevant performance parameters in a FWI configuration. To do so, new experimental data are obtained and on-purpose validated CFD simulations are specifically carried out under the same physical conditions. The workbench, designed and constructed for this study, consists of a single, partially premixed methane flame, impinging perpendicularly onto the bottom of a pot filled with cooled water. Temperature and CO emissions are evaluated under certain ranges of burner-to-pot distance, thermal power, inside-pot water temperature, and degree of premixing. These ranges encompass values present in real gas cooking burners. Outcomes from the experiments include: temperature values of the internal and external pot walls, inside-pot water temperature, jet velocity field (non-reacting flow), spatial distribution of the flame temperature, and CO and CO_2 emission concentration in the exhaust gases at the top of the hood (as it is done in the certification tests). Once the experimental program is completed and used to validate the computational model, the analysis is mainly based on the numerical results to obtain a complete description of the phenomena. Thus, the main goal is the evaluation of the effect of the aforementioned variables on the carbon monoxide formation, in order to establish relationships between the resulting flame structure, CO emissions, and thermal efficiency of the burner. Conclusions on this respect may be useful to find optimal burner designs, maximizing thermal efficiency and/or minimizing pollutants.

3.3 Experimental setup and procedure

3.3.1 Workbench description

The experimental facility used in this work was designed to study partially premixed flames impinging on a cold wall under closely controlled conditions. A general view is shown in Figure 3.1 and the main elements are described hereinafter.

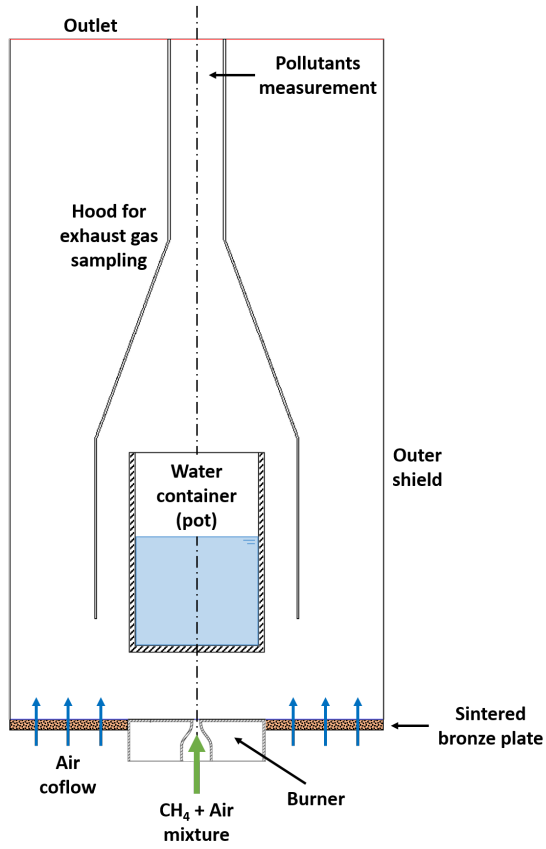

Figure 3.1: Schematic representation and main elements of the single flame burner experimental setup.

The burner:

The air-fuel mixture is injected through a convergent nozzle ending in a circular orifice of 5 mm diameter. The nozzle inner shape was designed to produce a very flat velocity profile at the exit and minimize turbulence intensity. Injector walls are surrounded by a cavity (100 mm diameter) within which cold water is recirculated to maintain a constant and low temperature (around 300 K), recorded by means of two wall thermocouples welded on the injector and the front wall respectively. These measurements are essential in order to know inlet gas and burner wall temperatures. A

premixer is included upstream to ensure homogeneity of the air-fuel mixture.

Outer shield and air co-flow:

To avoid flame perturbations due to laboratory air movements, the whole setup is protected by a cylindrical shield (280 mm diameter). Besides, a coaxial air flow is forced through a sintered bronze disk installed around the burner piece. The high pressure drop across the sintered element guarantees a flat velocity profile, which value is adjusted at 0.05 m/s in all the tests. The combination of the outer shield and the co-flow provides a controlled and known ambient around the burner, as required to specify boundary conditions for the numerical simulations.

The water pot:

The flame impinges on the bottom of a perfectly cylindrical water container, made in stainless steel, with a height of 150 mm, and 93 and 101 mm of inner and outer diameter respectively. Since the pot imposes a critical thermal boundary condition, the bottom is carefully instrumented to determine temperature and heat flux radial profiles (Figure 3.2). Ten thermocouples are inserted into the 5 mm thickness bottom wall, identified as S0-S4 (water, upper side) and F0-F4 (flame, bottom side). They are distributed at the same radial distances in order to obtain temperature profiles, local axial temperature gradient and, hence, local heat flux. Additional thermocouples are inserted into the side wall (SW) and in the water (W). The pot is closed with a lid, which is designed in such a way that the water condensed on its bottom side drops again into the pot, so that the vapor losses are very low and the level remains virtually constant during the experiments. Water temperature is also maintained constant throughout each test duration, so that data are collected for perfectly stable conditions. This is achieved by forcing the circulation of water through an outer loop with a diaphragm pump. Depending on the desired temperature, the loop can include a coil immersed in a cold water bath. By adjusting the length of the outer loop and optionally passing the water through the coil, water temperature can

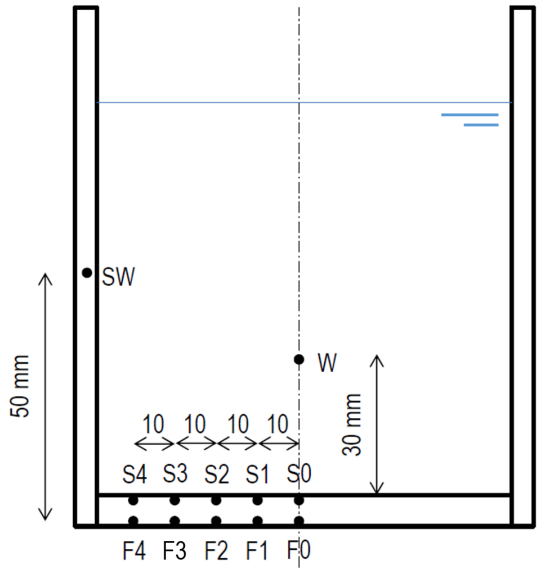

Figure 3.2: Scheme of the water pot with the location of the thermocouples embedded in the bottom wall (F* and S*), the side wall (SW), and inside the water (W).

be held sensibly constant at different set points. In particular, tests are performed at 308 K, 323 K, and 338 K. The water pot is supported on three rods welded on the top of the pot so as not to disturb the gas flow. This supporting system can be adjusted laterally as well as in height, in order to get the pot perfectly centered with respect to the injector and outer shield, and regulating the burner-to-pot distance as required for the various tests.

The hood:

Combustion products generated in the flame and flowing around the pot are collected in the upper part by a hood. It discharges through a cylindrical duct, where the gas sampling probe is installed. This probe consists of a stainless steel duct with several side orifices at selected points, to further ensure that the gas sample is representative of the average gas composition.

Support structure:

All the aforementioned components are assembled and supported on a mounting structure that includes all the necessary elements to hold them and finely adjust their relative position, as required for the conditions of the different tests.

3.3.2 Instrumentation and measurement techniques

The set of data collected in the tests is obtained with different instruments and techniques. A complete overview of the workbench is displayed in Figure 3.3.

- Local gas velocity components (under cold-flow conditions) is measured with constant-temperature hot wire anemometry (TSI, model IFA 300). Two-wire sensors are used to simultaneously obtain axial and radial velocity components, as well as their cross-correlation. These measurements typically present an uncertainty of ± 1% [116].

- Local gas temperatures are measured with a bare fine wire, S-type (Pt-Pt10%Rh) thermocouple, which is mounted on a 3-D traversing system to register between 1000 and 2000 mean temperature values across the flame, depending on the case. The sensing element consists of butt-welded 70 μm wires, supported on thicker (350 μm) wires of the same material. These are inserted into a two-bore alumina rod, which provides the required rigidity for accurate positioning in the flame. In-flame temperature measurements can be affected by conduction and radiation errors. The fine thermocouples used in this work have a length/diameter ratio >150, enough to make the conduction error negligible. As for the radiation error, the measurements are corrected by:

$$T_{gas} = T_{TC} + \frac{D_{wire} * \epsilon * \sigma * (T_{TC}^4 - T_{wall}^4)}{\kappa_{gas} * (0.35 + 0.65 * Re_{wire}^{0.45})} , \tag{3.1}$$

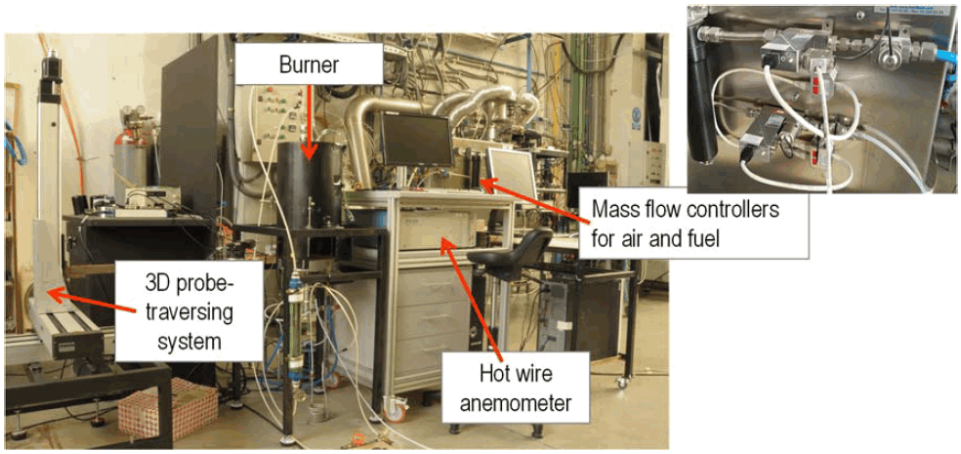

Figure 3.3: General view of the test workbench.

where T_{gas} is the real temperature of the gas, T_{TC} is the temperature measured by the thermocouple, and T_{wall} is the temperature of the surrounding cold walls (all of them in K); D_{wire} is the wire diameter (m); ϵ is the emissivity of the thermocouple; σ is the Stefan-Boltzmann constant (W/m^2*K^4); κ_{gas} is the thermal conductivity of the gas (W/m*K); and Re_{wire} is the Reynolds number calculated from the wire diameter and the density, viscosity, and velocity of the gas [117, 118]. Overall, the uncertainties due to the thermocouple material and the radiation correction are estimated to be around 10 K.

- Water, burner and pot wall temperatures are measured by stainless steel sheathed K-type thermocouples, which typically have an uncertainty of ± 2.2 K or ± 0.75%.

- Fuel, primary combustion air and secondary co-flow air mass flow rates are controlled and automatically regulated by three mass flow meters of the thermal type, supplied by the Bronkhorst company. They are connected in closed-loop to a control valve through PID (proportional, integral, derivative) regulators in order to ensure good accuracy and avoid oscillations or drifts during the tests. Since the flow rates are above 20% of the measurement range in all the tests, the accuracy is

always better than 1%, as defined by the supplier. This also applies to any derived parameter, like power, velocity at the injector outlet, or primary aeration.

- The gas sample collected at the hood outlet is sent by means of PTFE (Polytetrafluoroethylene) tubing to a a set of individual on-line gas analyzers (non-dispersive infrared (NDIR), manufactured by Emerson), where O_2, CO_2, and CO concentrations are measured on a dry basis. Associated uncertainty in the results of CO is mainly due to the reproducibility of the whole test and measurement process.

- A computer-controlled three-dimensional traversing system is employed to obtain two-dimensional maps of temperature and velocity, comprising between one and two thousand local measurements, depending on the case, performed at different axial and radial coordinates. After programming the measurement grid and setting the origin of coordinates with respect to a reference point, this device automatically displaces the tip of the sensor to the selected points with very good accuracy ($\pm$ 0.02 mm).

- A color video camera is placed next to the flame zone in order to record direct imaging of the flames.

In all the cases, the test is performed in duplicate, with an associated maximum standard deviation of 2 K in registered wall temperatures and a 5% in carbon monoxide measurements.

3.3.3 Operating conditions

Discrete values of the studied parameters are chosen to cover operating ranges that produce similar flow features to those present in real gas cooking burners. Flame thermal power ($\dot{P}$) is varied from 250 to 500 W, corresponding to Re numbers roughly between 700 and 1400. Primary aeration, defined by the the air-fuel equivalence ratio (lambda, λ, see Equation 1.1), ranges between 0.35 and 0.65. Burner-to-pot distance, fixed

at 20, 50 and 80 mm, is represented by the H/d ratio (4, 10 and 16), where H is the distance between the injector and the pot bottom wall, and d is the injector inner diameter. Finally, inside-pot water temperature (T_{water}) is modified between 308 and 338 K. Conditions for the baseline case (BC) are: $\dot{P}$=375 W, λ=0.5, H/d=10, and T_{water}=323 K. The test program for reacting cases is designed to perform parametric studies about this central case and includes a total of 15 different test conditions, shown in Table 3.1. In all these cases the objective is to characterize the main global parameters such as thermal conditions at the pot wall and CO emissions (denoted with **X**). In some selected tests, a detailed temperature field characterization is also performed (**O**).

Table 3.1: Experimental matrix with tested conditions.

Power [W]	H/d	Water Temperature [K]				
		308	323			338
		Primary aeration (λ)				
		0.5	0.35	0.5	0.65	0.5
250	4			X		
	10		X	X O	X	
	16			X		
375	4			X O		
	10	X	X O	X O	X O	X
	16			X O		
500	4			X		
	10			X O		
	16			X		

X – Pot temperatures and emissions
O – Temperature field

The flow field is also explored in non-reacting conditions. The characterization of the isothermal jet captures the essential features of the phenomenon (jet development, velocity decay rate, stagnation near the pot wall). For this exploration, the velocity field is measured when injecting only

air through the nozzle, with H/d=10 burner-to-pot distance and a mean velocity-magnitude of 7 m/s at the injector outlet. This value is higher than the fuel injection speed in the reacting cases and also in gas cooking burner ports (2-5 m/s), but was deemed adequate for the purpose of this analysis in order to avoid the increased uncertainties with hot wire anemometry for low velocities [116].

3.4 Computational setup and procedure

In parallel with the experimental study, CFD simulations are carried out to numerically describe all the phenomena occurring in the system. For this purpose, continuity, momentum, energy, and chemical species transport equations are solved in a steady-state regime using the software ANSYS Fluent [90].

3.4.1 Computational domain and mesh

Given the cylindrical geometry of the setup, a two-dimensional, axisymmetric domain is adopted. The nozzle and the burner inner volumes are not included in the domain, setting directly the boundary condition values at the fuel inlet (injector outlet), burner wall, and air co-flow inlet.

Based on previous experience with these type of configurations, the domain is discretized into ≈119 thousand cells for the baseline case (H/d=10), with finer resolution on the flame zone, specially in the vicinity of the injector outlet (where chemical reaction starts) and a gradual inflation zone to accurately capture the boundary layer at the hot gas / solid bottom pot wall (Figure 3.4).

In the meshing process, the influence of the mesh resolution on the results is checked. Different cases are performed, using the same settings and convergence criteria, as shown in Table 3.2 for the H/d=10 case. Four critical variables are monitored: the averaged temperature of the solid pot, and the temperature, CO_2 and CO mole fraction in the exhaust gases stream at the top of the hood. The agreement between the results obtained with the base

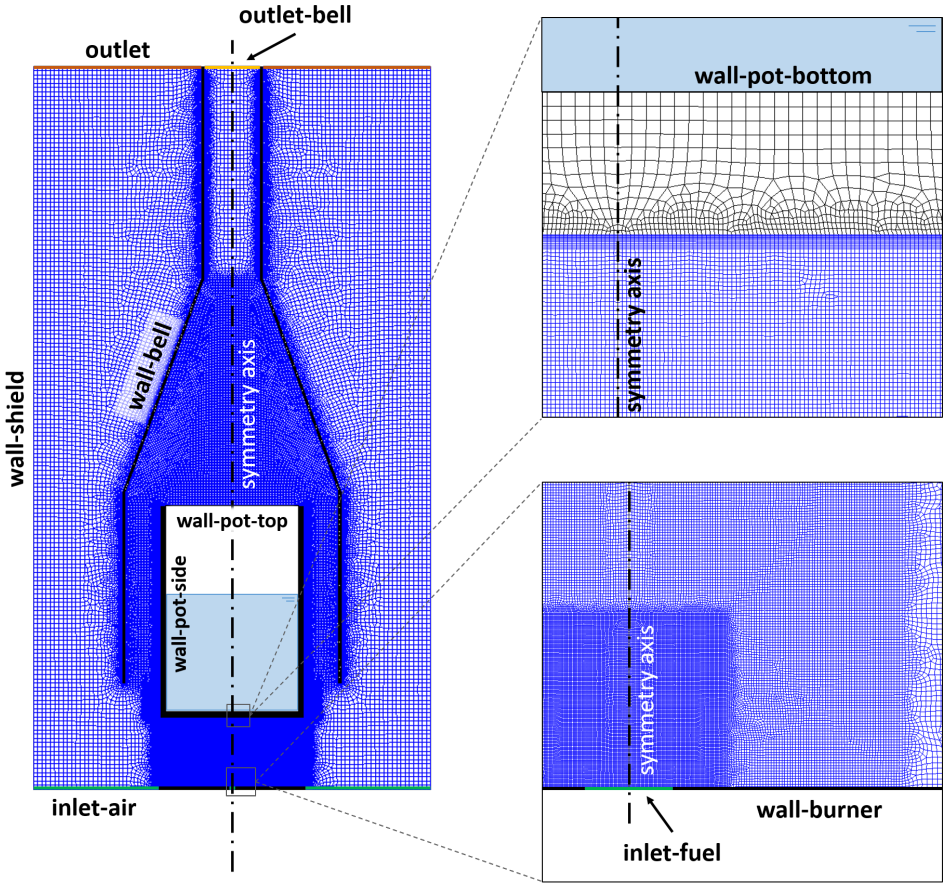

Figure 3.4: Two-dimensional axisymmetric mesh of the setup with identification of the main zones and boundaries of the computational domain.

Table 3.2: Results of the refinement study of the mesh for the H/d=10 case.

Mesh	Coarser	Base	Finer
Cell number	29713	118852	475408
Cell size (near pot wall resolution, mm)	0.062	0.031	0.016
CPU time (16 cores, s/iteration)	0.76	2.60	8.06
Averaged pot temperature (K)	328.65	328.48	328.48
Temperature (outlet-bell, K)	336.47	332.36	332.48
CO_2 mole fraction (outlet-bell, %)	1.176	1.205	1.210
CO mole fraction (outlet-bell, ppm)	48.01	156.99	157.65

and the refined mesh shows the suitability of the original mesh resolution. Same criteria for the rest of the burner-to-pot distance H/d=4 and H/d=16 cases are followed, resulting in 84 and 154 thousand cells respectively.

3.4.2 Numerical models

The experimental configuration was designed to feed a laminar jet through the injector (Re between 700 and 1400). However, tests revealed that in most of the cases, starting from a very low turbulence intensity, the amplitude of velocity fluctuations starts to grow in the jet after a few millimeters. A transition turbulence model (four-equation Transition SST (shear stress transport) k-omega [119,120]) is therefore selected to properly capture the decay rate in jet velocity. Despite using this turbulence closure, the combustion is Arrhenius-rate governed (Laminar Finite Rate) by Direct Integration of the chemical kinetics in the Stiff Chemistry Solver of the code, and none turbulence-chemistry interaction is considered.

Net production rate of each chemical species is calculated by adding the specification of gas-phase reactions, thermodynamic and transport properties data contained in special formatted files (Chemkin format). In order to obtain the most reliable results for the chemical species description, the detailed chemistry for methane combustion is considered by employing the GRI-Mech 3.0 mechanism [48].

The mixture is considered to be a multicomponent ideal gas where

density depends only on temperature and composition. Kinetic theory is invoked for transport properties such as viscosity, thermal conductivity and mass diffusivity. Radiation is considered by means of the coupled Discrete-Ordinate Model (DOM) [121]. For the Species Model option, the effect of enthalpy transport due to species diffusion in the energy equation (Diffusion Energy Source) is explicitly considered whereas multicomponent diffusion is enabled. Coupled Algorithm for pressure-velocity coupling with PRESTO! (PREssure STaggering Option) scheme for pressure interpolation is selected, whereas second order upwind spatial discretization is applied to the rest of transport variables. A complete overview of the governing equations and their properties can be found in the Appendix I.

3.4.3 Boundary conditions

Specific boundary conditions for the model are summed up in Table 3.3. The temperatures measured at the injector outlet and burner wall are very stable throughout the experimental tests, in the range 300±1 K.

Table 3.3: Specific boundary conditions set in the numerical simulation of the flame.

Zone	**Type**	**Thermal condition**	**Other**
inlet-fuel	velocity-inlet	Inlet $T = 300$ K	Exp. velocity profile $\lambda = 0.35/0.5/0.65$
inlet-air	velocity-inlet	Inlet $T = 300$ K	$v_{inlet} = 0.05$ m/s
wall-burner	wall	Fixed $T = 300$ K	
wall-shield	wall	Adiabatic	
wall-pot-bottom	wall	Exp. radial temperature profile	
wall-pot-side (water)	wall	Fixed $T = 308/323/338$ K	
wall-pot-side (air)	wall	Convection (air)	HTC[a]= 15 W/m^{2}K $T_\infty = 308/323/338$ K
wall-pot-top	wall	Convection (air)	HTC[a]= 15 W/m^{2}K $T_\infty = 308/323/338$ K
wall-bell	wall	Conjugate heat transfer	
outlet / outlet-bell	pressure-outlet	Backflow $T = 300$ K	$P_{gauge} = 0$ Pa

[a] Heat transfer coefficient

Therefore, a constant value of 300 K is set for the injected fuel and the burner wall temperatures. The radial velocity profile at the injector outlet is imposed as boundary condition for the fuel jet, together with the corresponding air and fuel concentrations in each case (λ=0.35, 0.5 or 0.65). Water inside the pot is not explicitly included in the computational domain. Instead, the interpolated temperature profile from measurements (S0-S4) is allocated in the pot water-side bottom wall. At the pot side wall, the temperature value is obtained from the thermocouple inserted in that location (SW), and matches with water temperature (308, 323 or 338 K). For internal wall zones in contact with air, convective heat transfer boundary conditions are applied. The burner, the bell, and the pot are constructed of stainless steel, so a value for internal emissivity of ϵ=0.4 [122] is considered.

3.5 Results and discussion

3.5.1 Non-reacting flow characterization

Previous to simulate the reacting cases, the jet is characterized under cold-flow conditions. For this purpose, the velocity-magnitude profile measured along the centerline is compared to those obtained when simulating the non-reacting case enabling the different viscosity models: laminar, turbulence two-equation k-epsilon, turbulence three-equation transition k-kl-omega, and turbulence four-equation transition SST k-omega. Figure 3.5 shows that the laminar approach is completely inaccurate for these conditions.

Among the turbulence models, transition SST k-omega clearly shows the best agreement, with a slight deviation at the beginning of the decay zone (axial position $\approx$ 0.027 m). The good coincidence between numerical and experimental results is further confirmed by the two-dimensional maps shown in Figure 3.6a (experimental values are graphically interpolated). In addition, Figure 3.6b compares normalized contours of root-mean-square velocity (v_{rms}), which is representative of the turbulent fluctuations of the velocity magnitude [123].

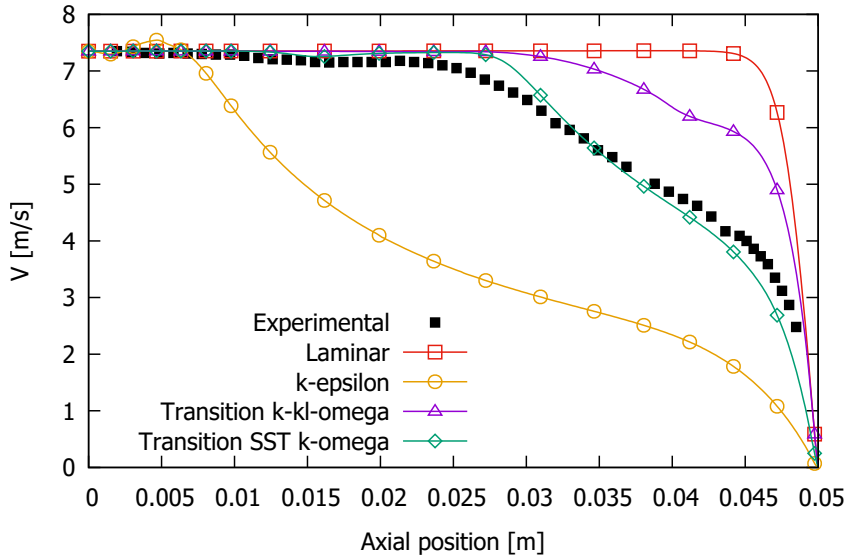

Figure 3.5: Comparison between experimental and computationally obtained velocity-magnitude profiles along the centerline in the non-reacting case.

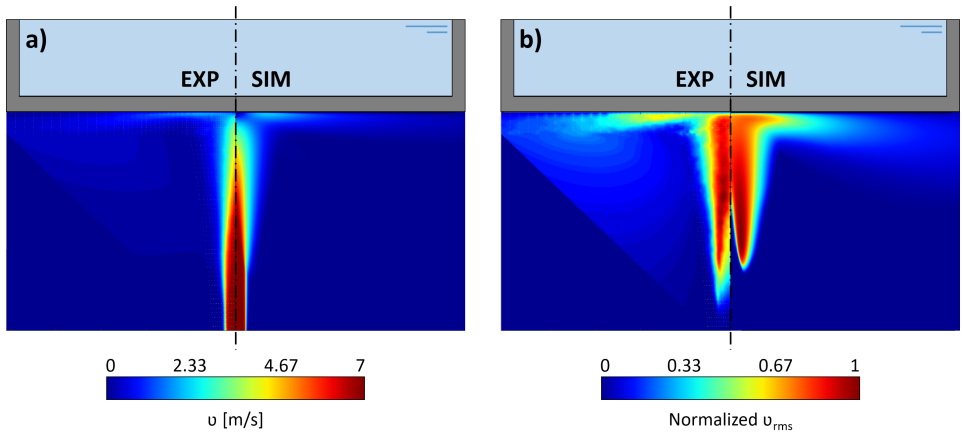

Figure 3.6: Experimental and transition SST k-omega computational comparison of velocity module (a) and normalized root-mean-square velocity (b) fields.

It can be observed that turbulence starts to grow only a few millimeters downstream the injector. The transition SST k-omega turbulence model includes a free-stream correlation to relaminarize the flow when turbulent fluctuations are negligible, so it also shows to be valid in the cases when the mean velocity magnitude, and thus Reynolds number, are lower [119, 120]. Therefore, it is selected to calculate the flow field in all the reacting flow calculations.

3.5.2 Reacting flow characterization

The jet velocity-magnitude in the reacting cases is slightly lower (2-5 m/s, depending on the $\dot{P}$) than the observed in the non-reacting case ($\approx$ 7 m/s). Despite the lack of experimental measurements of velocity components for the combustion cases, Figure 3.7a shows the axial velocity decay rate inside the flame for the constant baseline case conditions (H/d=10, λ=0.5, T_{water}=323 K) and the three analyzed $\dot{P}$ cases.

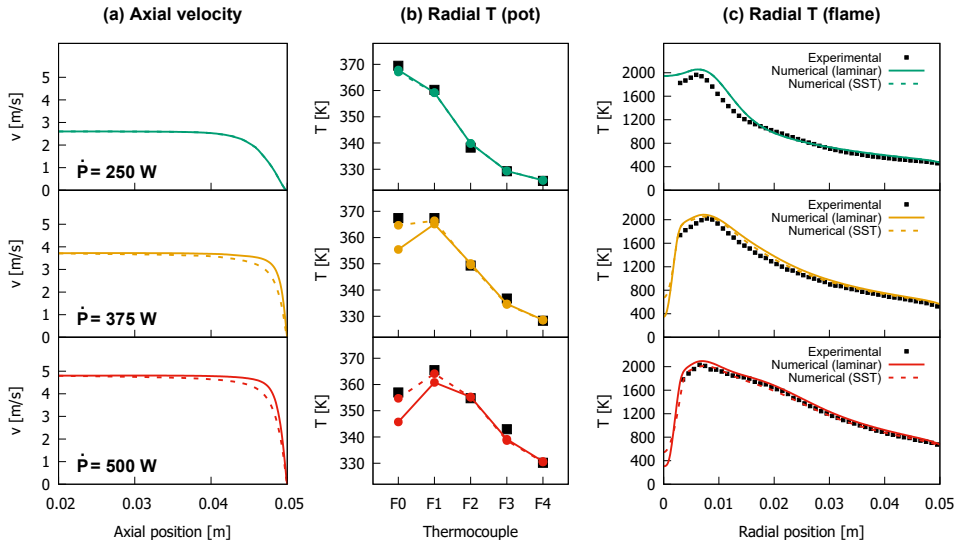

Figure 3.7: Characterization of the velocity-magnitude along the centerline of the flame jet (a), temperature at the pot bottom wall (b), and flow field temperature near (3 mm) the pot bottom wall (c).

It can be observed that there is no difference between the laminar and the turbulence model predictions for the lower $\dot{P}$=250 W case. This fact confirms the capabilities of the transition SST k-omega turbulence model to relaminarize the flow when there are no relevant turbulent fluctuations. However, slight differences can be observed for the medium and higher $\dot{P}$ cases. The analysis of the radial pot temperatures shown in Figure 3.7b determines that the predictions using the SST k-omega turbulence model agree better with measurements and therefore corroborates a more accurate flow field and conjugated heat transfer prediction for the flame-wall interface, mainly in the flame impingement zone. In the rest of the flame field, the differences between laminar and turbulent predictions are negligible as shown in Figure 3.7c, where the radial profiles of the flow temperature at 3mm below the pot wall show a very good agreement between both numerical predictions and measurements. This fact brings out the suitability of the finite rate chemistry approach without needing a turbulence-chemistry interaction model.

3.5.3 Temperature characterization

An accurate numerical description of temperature values is essential to obtain reliable CO emission data. Once the reacting cases are experimentally and computationally carried out, pot wall temperatures in the flame side (F0-F4) are compared in Figure 3.8, for different thermal power and burner-to-pot distance, with constant λ=0.5 and T_{water}=323 K. It can be seen that F-side temperature values are properly captured in all the cases, with a maximum deviation of $\pm$5 K.

To further evaluate the agreement between predictions and measurements, flame temperatures are analyzed and compared in Figure 3.9. Experimental and computational (with detailed chemistry) temperature fields are presented for the constant baseline case conditions (H/d=10, λ=0.5, T_{water}=323 K) and the three different $\dot{P}$ cases. A significant deviation was observed in the inner core, inside the conical premixed flame. In this zone, no reaction or heat release occurs and, hence, the gas should

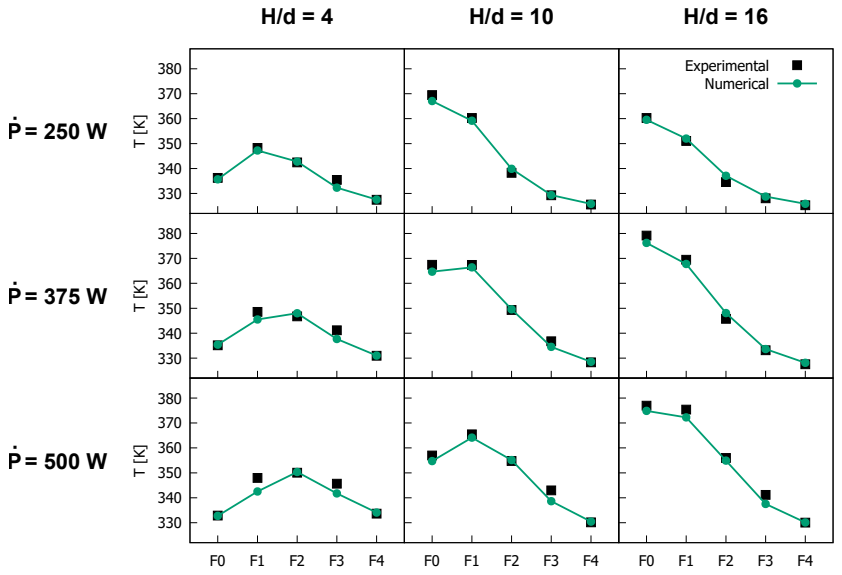

Figure 3.8: Measured and predicted temperature profiles on the F-side of the pot wall for different thermal power and burner-to-pot distance, at λ=0.5 and T_{water}=323 K.

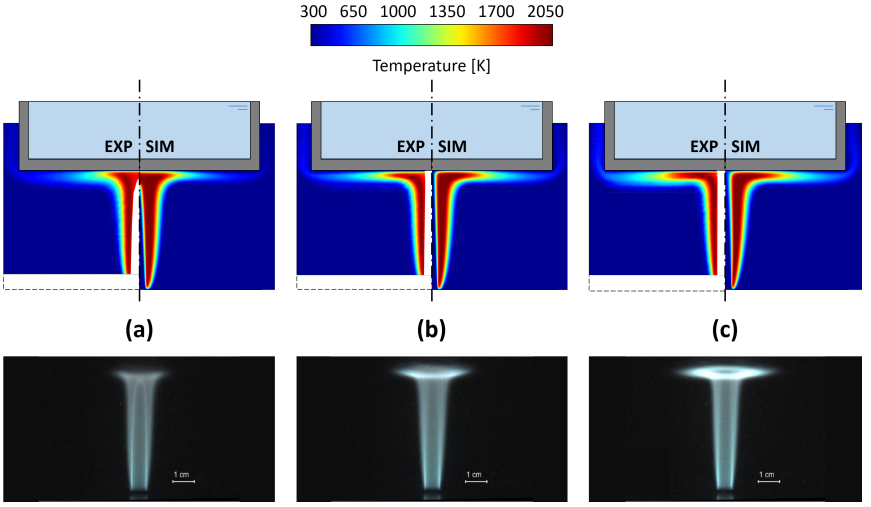

Figure 3.9: Experimental and numerical temperature fields comparison for baseline case conditions and: (a) $\dot{P}$=250 W; (b) $\dot{P}$=375 W; (c) $\dot{P}$=500 W. Associated direct imaging of the flames, recorded with the video camera (visible range), are presented below.

be at low temperature, as shown in the computational contours. However, higher temperatures (1000-1500 K) were experimentally measured in that zone. This was due to an experimental artifact: the heat conduction along the thermocouple wires together with the catalytic properties of platinum induce oxidation reactions around the wires, causing significant overheating of the wires and, hence, overestimating the actual gas temperature inside the premixed flame cone. Therefore, experimental values are not a valid reference in this zone, so they are omitted from the comparison. This circumstance does not occur in the diffusion flame, where the only significant error source is due to radiative heat transfer and, as it has been indicated above, is estimated to be around 10 K.

Apart from this experimental issue, it can be generally seen a good agreement between measurements and computational temperature fields. The initial part is practically the same in the three cases, indicating that this zone is not affected by the thermal power. Once the flame reaches the pot, the remaining amount of fuel reacts in the form of a wall flame, which becomes larger as $\dot{P}$ is raised. This increment gradually displaces the high temperatures away from the pot center, as it can be observed in the H/d=4 and H/d=10 cases of Figure 3.8. The agreement between experimental and numerical temperature fields is reinforced by the radial profiles comparison shown in Figure 3.7c.

Another important fact is related to the inner premixed flame cone. For the $\dot{P}$=250 W case, it is perfectly defined, ending at some distance from the pot wall, as it can be seen in the computational contour and the flame image of Figure 3.9a. For higher $\dot{P}$, the injection velocity increases and so does the height of the conical flame. As a result, the cold core reaches the pot wall so that the premixed flame does not exhibit a vertex but the core impinges and spreads on the cold surface for $\dot{P}$=375 and 500 W. This effect is clearly visible both in the calculated temperature maps and in the flame photographs, and explains the lower temperature registered at the F0 with respect to the F1 thermocouple in the tests with higher thermal power and/or shorter burner-to-pot distance, as shown in Figure 3.8. Finally, flame

temperatures close to the wall are reduced due to the significant quenching effect produced by the cold wall, which may affect the final oxidation steps of certain chemical species.

3.5.4 CO emissions

Regarding emissions, CO, CO_2 and O_2 dry concentrations are measured in the exhaust gases stream. Then, CO is air-free corrected (0% oxygen). This value, known as CO Air Free (COAF), can be calculated by Equation 2.1. As explained in section 2.2.3 from Chapter 2, COAF is the parameter used to asses carbon monoxide emissions according to the European Standard certification [11] for domestic gas cooking burners, with a threshold value in the range 1000-1500 ppm, depending on the type of test.

Effect of inside-pot water temperature

The temperature of the water inside the pot is modified by decreasing and increasing 15 K from the reference value of 323 K (constant $\dot{P}$=375 W, H/d=10, λ=0.5), in order to evaluate the effect of the wall temperature on CO emissions.

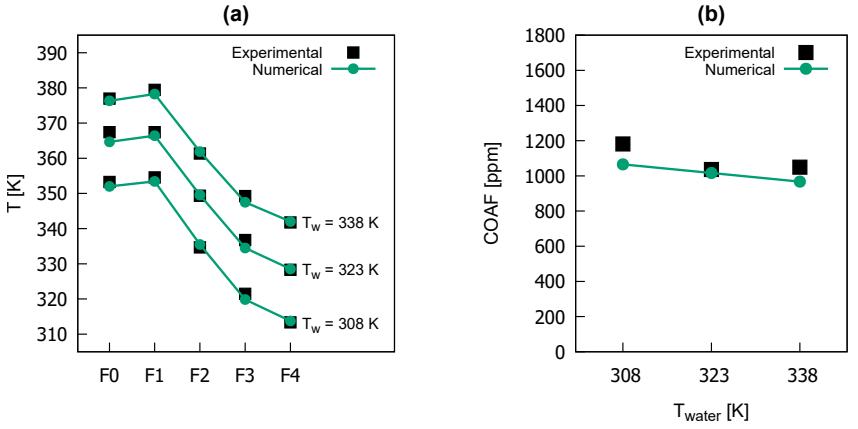

Figure 3.10: Temperature profiles on the F-side of the pot wall (a) and COAF evolution (b) for different inside-pot water temperatures (constant $\dot{P}$=375 W, H/d=10, λ=0.5).

As shown in Figure 3.10a, the increment in the inside-pot water temperature produces an analogous displacement in the radial temperature profile of the pot wall (flame side). Figure 3.10b shows that COAF steadily decreases as the wall becomes hotter, which seems consistent with a slight reduction of the quenching effect produced by the wall. A good agreement between measurements and numerical CO values can be observed.

Effect of primary aeration

Primary aeration is modified in the $\dot{P}$=250 and 375 W cases, with two additional tests about the baseline value (λ=0.35, 0.5 and 0.65), and keeping constant H/d=10 and T_{water}=323 K. As seen in Figure 3.11, COAF decreases for both $\dot{P}$ as more primary air is supplied. This is an expected behavior and consistent with the higher availability of primary oxygen in the partially premixed stream, enhancing the oxidation of CO to CO_2. The agreement of measurements with GRI-Mech 3.0 is good, although, for the lowest λ=0.35, the numerical approach shows a noticeable COAF underprediction; this could be related to a mismatching in the capture of the flow pattern between the secondary air and the flame front, which leads to different physical conditions for relevant combustion reactions.

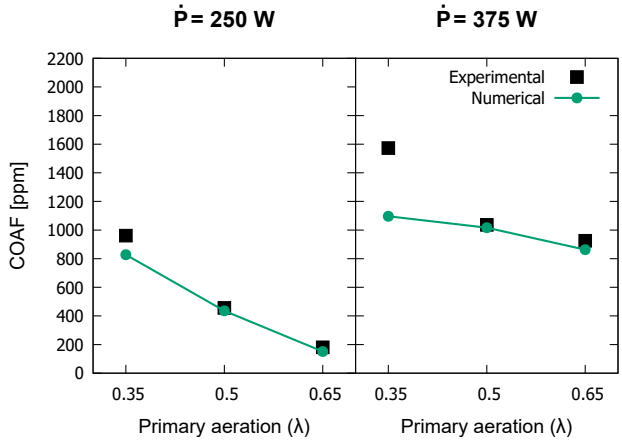

Figure 3.11: Effect of primary aeration (λ) in COAF values for $\dot{P}$=250 and 375 W (constant H/d=10, T_{water}=323 K).

Effect of flame thermal power and burner-to-pot distance

Evolution in COAF values may be analyzed either by fixing a burner-to-pot distance H/d, as directly separately shown in Figure 3.12, or by comparing points with the same thermal power $\dot{P}$. In all the cases, the rest of reference conditions are kept constant (λ=0.5 and T_{water}=323 K).

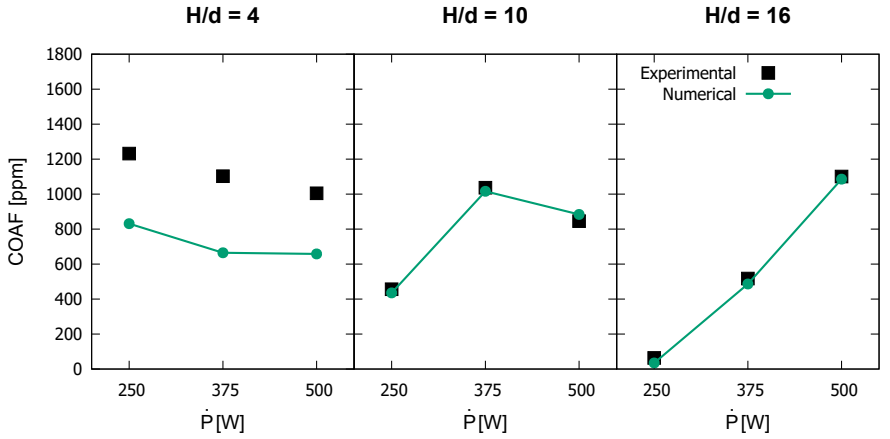

Figure 3.12: Effect of thermal power on COAF values at different burner-to-pot distance (constant λ=0.5, T_{water}=323 K).

For the H/d=16 cases, COAF grows sharply with increasing $\dot{P}$. This could be seen as the usual trend [109, 113] and a consequence of a larger fraction of the reactions taking place in a wall flame (Figure 3.9), with significant quenching effects in the layers closer to the wall. For the shortest burner-to-pot distance (H/d=4), the opposite trend is observed; this might be due to an enhanced cooling of the flame as $\dot{P}$ is decreased, resulting in higher residual CO concentrations. At the intermediate distance (H/d=10), the COAF displays a maximum for $\dot{P}$=375 W, which indicates different dominant effects at each side.

If results are analyzed for fixed $\dot{P}$ and variable H/d, similar trends can be observed. For $\dot{P}$=250 W, CO emissions decay as the wall is progressively located away from the injector. The significant quenching effect of the cold wall on the oxidation reactions for H/d=4 produces the highest CO emission;

on the other hand, the flame barely impacts on the pot for H/d=16, which suggests that most of the carbon compounds have already been oxidized to CO_2, leaving sparse residual CO. Different trends are observed for the medium and the high thermal power. As the pot is moved away from the burner, a peak in the numerical COAF at H/d=10 can be observed for fixed $\dot{P}$=375 W, while a steady rise is noticed at $\dot{P}$=500 W. This latter increment in COAF values together with the one observed when changing H/d from 4 to 10 at $\dot{P}$=375 W are due to the enhancing of the reactions of hydrocarbon radicals towards CO rather than the oxidation ones from CO to CO_2. These assorted trends in CO emissions when varying either $\dot{P}$ or H/d are further analyzed and detailed in the Chapter 4 of this thesis.

Regarding the comparison between measurements and calculations, a good agreement in COAF prediction can be seen in the H/d=10 and H/d=16 cases; nevertheless, a constant deviation is observed in the H/d=4 ones. This discrepancy, together with the one observed for the lowest λ configuration at $\dot{P}$=375 W (Figure 3.11), is attributable to the combination of two factors. Firstly, the ratio between the length of the flame and the burner-to-pot distance in these cases is high enough to produce flow fluctuations that can increase the uncertainties of the experimental measurements. Secondly, these ratio may affect the numerical description of the mixing rates given by the interactions between the hot gases from the flame front and the co-flow air stream.

3.5.5 Statistical evaluation of the modeling

In order to quantify a global accuracy of the numerical approach, the weighted standard deviation is calculated, separately for temperature and COAF values, by

$$\sigma_w = \sqrt{\frac{1}{N-1}\sum_{i=1}^{N}\left(\frac{y_i - \hat{y}_i}{y_i}\right)^2}, \tag{3.2}$$

where y_i and $\hat{y}_i$ are the experimental and simulated pot wall temperature

(K) or COAF (ppm) values respectively, and N is the total number of sampling points (75 for temperature, 15 for COAF). The global error is 0.5% and 9.1% from the temperature and COAF results respectively, which is in agreement with findings shown in Chapter 2.

3.6 Conclusions

A single, partially premixed methane flame configuration (Bunsen-like burner), impinging perpendicularly onto the bottom wall of a water pot, is designed and constructed. Subsequently, temperature and CO emissions are evaluated under certain ranges of flame thermal power, burner-to-pot distance, primary aeration and inside-pot water temperature, under representative conditions of domestic gas cooking burners. CFD simulations representing the setup are also carried out, with skeletal and detailed chemistry. The following conclusions can be drawn from this study:

1. The numerical approach is able to capture all the relevant phenomena occurring in the flame: the velocity decay in the jet, the flame shape with the inner premixed cone and the diffusion zone, pot wall temperature and its distribution, and pollutants emission.

2. The increase of the inside-pot water temperature produces an analogous rise on the pot wall temperature. Consequently, the quenching effect on the flame diminishes, which implies a reduction in CO emissions.

3. If the primary aeration of the burner is raised, the higher availability of oxygen in the partially premixed stream enhances the oxidation reactions, such as those where CO evolves towards CO_2, which is translated into final lower COAF values.

4. When the burner-to-pot distance or the flame thermal power is modified, non-monotonic trends in CO emissions are observed. This behavior may be related to differences in the flame structure and the

inner premixed flame cone. A comprehensive analysis is included in the Chapter 4 of this thesis.

As a general conclusion, it can be stated that CO production is slightly influenced by the temperature of the solid parts that are in contact with the flame, but it is more strongly affected by the resulting structure of the flame produced by that impingement. A further detailed study may come up with conclusions of great relevance in the design of domestic gas cooking burners. For that, the reader is referred to the Chapter 4.

Chapter 4

Flame-wall interaction phenomena

This chapter presents an extensive analysis of the flame-wall interaction phenomena and its influence on the flame structure and the carbon monoxide emissions. For this purpose, and starting from the results shown in section 3.5.4, extra numerical calculations are carried out in order to obtain a more detailed evolution of CO emissions at intermediate values of flame thermal power. A strong relationship between the internal structure of the flame and carbon monoxide is detected. In addition, the oxidizer consumption and the heat released from the flame are used to define the completeness of the combustion reaction. Finally, a spatial definition of the flame zones where CO chemically reacts is included, followed by an analysis of the CO chemical reaction rates inside the flame, which eventually lead to the net formation of this pollutant. Main conclusions drawn from the study are listed at the end of the chapter.

This analysis aims at providing a comprehensive study of the evolution of carbon monoxide in this type of configurations, evaluating how, where, and how much is produced and consumed of this species inside the flame, for different values of the flame thermal power.

4.1 COAF and flame thermal power evolution

From Chapter 3, non-monotonic trends in CO emissions are observed when burner-to-pot distance or flame thermal power is modified. Likely, the most explicit situation occurs at H/d=10 conditions of Figure 3.12, where COAF exhibits an increase from 250 W to 375 W, and then, a decrease from 375 W to 500 W. It is clear that, at some intermediate power values, a change in the trend is produced by the resulting interaction of the flame with the pot wall.

In order to deeply investigate the observed COAF trends from the aforementioned figure, additional simulations are carried out with the H/d=10 configuration and extra values of $\dot{P}$ in the range 150-600 W, obtaining a more detailed COAF evolution line. In these cases, a convection boundary condition is specified at the pot water-side bottom wall, with a heat transfer coefficient of 800 W/m^{2}K and a free-stream temperature of 323 K. The rest of the boundary conditions are as previously specified.

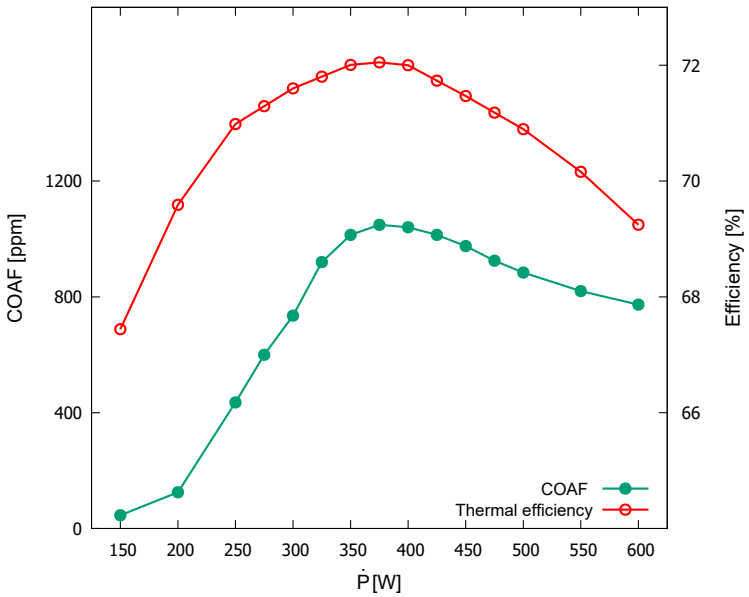

Figure 4.1: Detailed COAF and thermal efficiency evolution at different $\dot{P}$ (constant H/d=10, λ=0.5, T_{water}=323 K).

The results in Figure 4.1 show a maximum COAF value for $\dot{P}$=375 W. The evolution of the thermal efficiency of the burner is also included, which is directly calculated as a ratio between the surface integral of the heat flux across the pot walls and the flame thermal power, computed from the gross calorific value of the fuel (see Equation 2.3). It can be seen that this parameter follows the same trend as the COAF. Thus, for this type of configurations, there is a coincident operating point where maximum thermal efficiency always gives the maximum CO emissions. This is a relevant finding because it brings up reachable design points in both performance and emission thresholds.

4.2 Inner premixed flame cone

Naturally, as $\dot{P}$ changes, the structure of the flame is modified due to its interaction with the pot wall. This structure, represented by means of the temperature distribution, is displayed for each case in Figure 4.2.

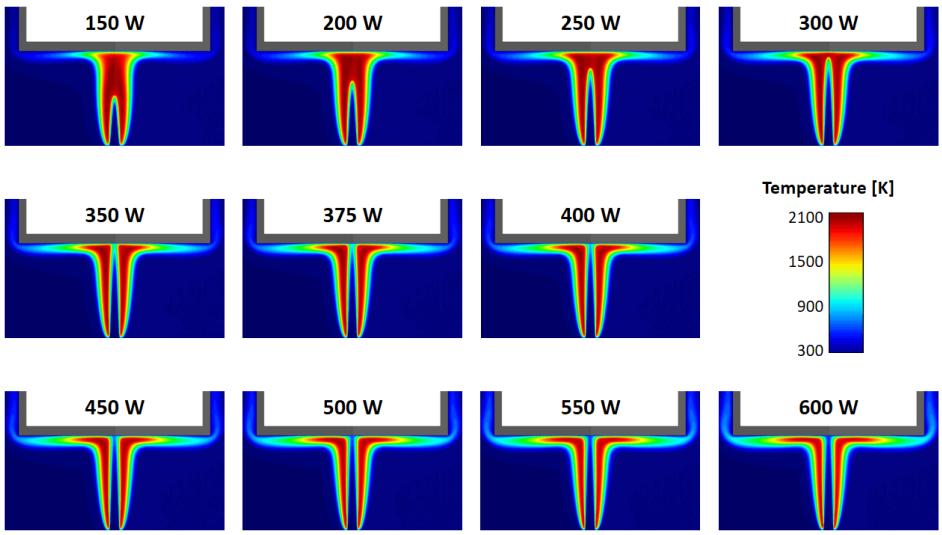

Figure 4.2: Computational temperature contours at different $\dot{P}$ (constant H/d=10, λ=0.5, T_{water}=323 K).

It can be seen that the highest temperatures of the flame are gradually displaced from the central axis by the lower temperature of the inner premixed cone as $\dot{P}$ increases. This cone reaches the bottom wall of the pot in the range of 350-400 W, in line with the maximum values of COAF and thermal efficiency observed in Figure 4.1.

In order to better track a boundary of the conical premixed flame, the consideration of the CH_4 oxidation pathway to CH_3 is taken into account [124]. The chemical reaction pathways of methane combustion are further detailed in Appendix 4.A. Therefore, a threshold criteria to consider the spatial starting of the combustion reaction, and thus the location of a boundary for the premixed cone, is established in this study as 10% of the maximum CH_3 concentration, represented by the iso-lines drawn in Figure 4.3.

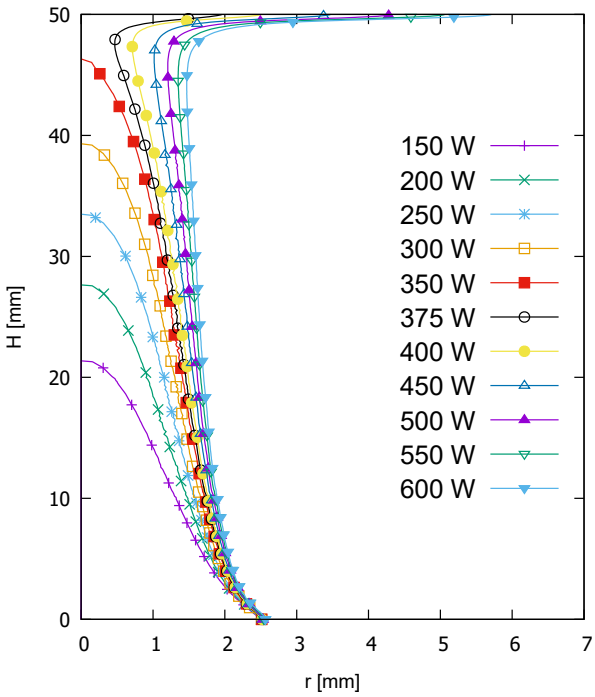

Figure 4.3: Limit of the conical premixed flame, represented by CH_3 concentration, at different $\dot{P}$ (constant H/d=10, λ=0.5, T_{water}=323 K).

The results visually confirm a direct relationship between the evolution of the inner premixed flame cone and both the CO emissions and thermal efficiency of the burner. As $\dot{P}$ increases, COAF and efficiency rise as long as the premixed cone is not affected by the wall. Once the flame is long enough and the rupture of the cone is produced due to its impingement with the pot ($\dot{P}$=375 W), COAF and efficiency values reach their maximum, with a subsequent smoother decrease if $\dot{P}$ keeps being raised.

This also explains the effect of flame thermal power at other burner-to-pot distances shown in Figure 3.12. For H/d=4 cases, COAF decreases because the premixed cone is broken in the three cases. On the other hand, COAF increases with $\dot{P}$ for the H/d=16 cases: the pot is far enough and the breakage of the cone does not occur in none of the three cases. In general, this situation would be always observed in similar situations as long as the pot approaches and perturbs the flame.

4.3 Reaction completeness of the combustion process

The global effect from the flame-wall interaction on the chemical reactions can be assessed by the definition of two parameters to evaluate the reaction completeness of the combustion. On the one hand, the oxidizer mass balance gives the amount of O_2 consumed in each configuration. Although λ is kept constant in these cases, the total mass quantity injected in the partially premixed stream depends on the $\dot{P}$. For this reason, the consumption value needs to be normalized by the CH_4 inlet mass flow. By stoichiometry, an ideal value of 4 kg of O_2 consumed per each kg of CH_4 supplied would represent the complete combustion. Then, the reaction completeness is lower as this consumption value moves away from 4 kg O_2 / kg CH_4. On the other hand, the ratio between the integration of the heat released from the whole flame and the supplied heat power input can be used as another definition of the reaction completeness.

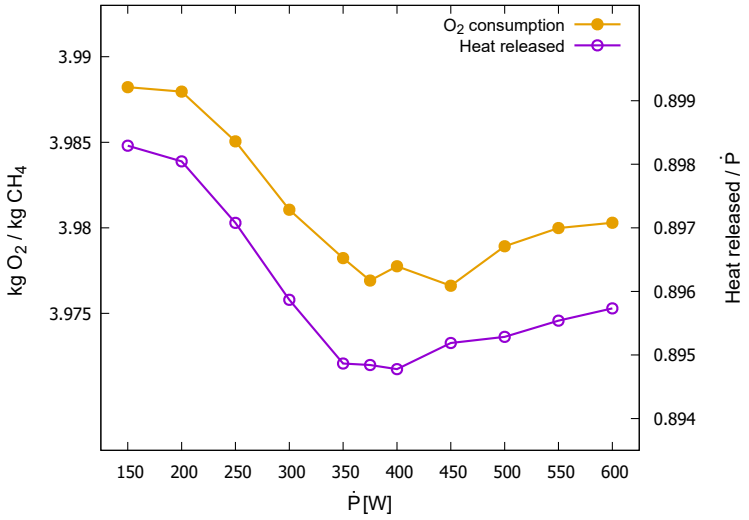

Figure 4.4: Assessment of the combustion reaction completeness from the consumed O_2 and the heat released from the flames (normalized with the CH_4 inlet mass flow and the thermal power respectively).

It can be observed in Figure 4.4 that both definitions show an alike behavior, with reverse trends to the COAF one observed in Figure 4.1. This fact confirms that chemical reactions are naturally affected by the evolution of the flame structure as $\dot{P}$ changes, increasing the effects of the flame-wall interactions. Once the inner premixed flame cone reaches the pot wall, its breakage leads to a progressively lower quenching effect, radially spreading the primary mixture towards the pot lateral wall and enhancing the progress of the combustion reaction.

4.4 Carbon monoxide evolution in premixed and diffusion conditions

At this point, it is straightforward to assert that the structure of the flame resulting from its interaction with the pot wall is the key to the two different behaviors observed, divided by the rupture of the inner premixed flame cone. In order to evaluate how the CO formation rates are affected by the

changes in the flame structure, a spatial definition of the CO-reaction zones is established. To do so, an additional conservation equation is solved for a passive scalar to individually track the two inlet streams, evolving from a value of 1 at the partially premixed fuel inlet to 0 at the air co-flow inlet (Figure 4.5a). The required steps for its definition in the CFD code is detailed in Appendix 4.B. The local combination of this transported scalar and the concentration of O_2 (Figure 4.5b) can be used to identify the oxidizer that comes from the fuel stream (primary O_2, Figure 4.5c) and the air co-flow inlet (secondary O_2, Figure 4.5d).

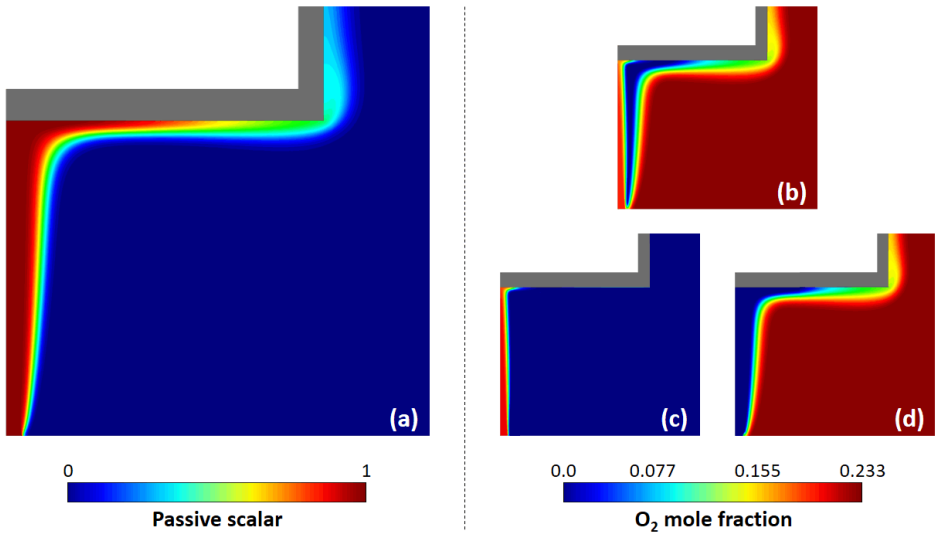

Figure 4.5: Distribution of the passive scalar (a) and the concentration of O_2 in the flame (b), distinguishing between the primary oxygen (c) and the secondary oxygen (d). Case conditions: $\dot{P}$=375 W, H/d=10, λ=0.5, T_{water}=323 K.

Considering only the regions of the flame where the CO chemically evolves, either by production or consumption (i.e., where the CO net reaction rate $\neq 0$), it is possible to define two different zones:

1. The CO-reacting premixed zone, as a result of the spatial combination of the regions where the CO net reaction rate $\neq 0$ and where the

concentration of primary $O_2 > 0$. Namely, the evolution of CO in this zone is due to the presence of oxidizer coming from the partially premixed fuel stream.

2. The CO-reacting diffusion zone, defined by the spatial coincidence of the regions where the CO net reaction rate $\neq 0$ and where the concentration of secondary $O_2 > 0$. Likewise, here CO evolves due to the oxidizer that comes from the air co-flow stream.

Both zones are displayed at the top of the Figure 4.6 for each $\dot{P}$ case. For the lowest $\dot{P}$ values, the structure is similar to a free flame configuration, although naturally the hot gases need to run over the bottom and lateral pot walls by buoyancy; once the CO-reacting premixed zone reaches the pot, both regions propagate along the wall.

In the gap between the zones, the CO does not chemically react but is only transported by convection and diffusion. The highest concentrations of CO are located in this gap, as can be observed at the bottom row of Figure 4.6, where the corresponding CO volumetric concentration throughout the flame is shown. This means that most of the CO production occurs in the CO-reacting premixed zone, whilst its consumption predominantly takes place in the CO-reacting diffusion one. This fact is confirmed by the independent evaluation of the CO net formation inside both zones for each $\dot{P}$, normalized by the corresponding CH_4 inlet mass flow. As can be seen in Figure 4.7a, the CO-reacting premixed zone is predominantly a CO production region (net positive values), whilst the CO-reacting diffusion zone is primarily CO-consuming (net negative values). From these curves, it can be concluded that both zones, and the evolution of CO-related reactions, are affected by the presence of the pot wall, with a stronger effect as the flame grows and approaches the pot.

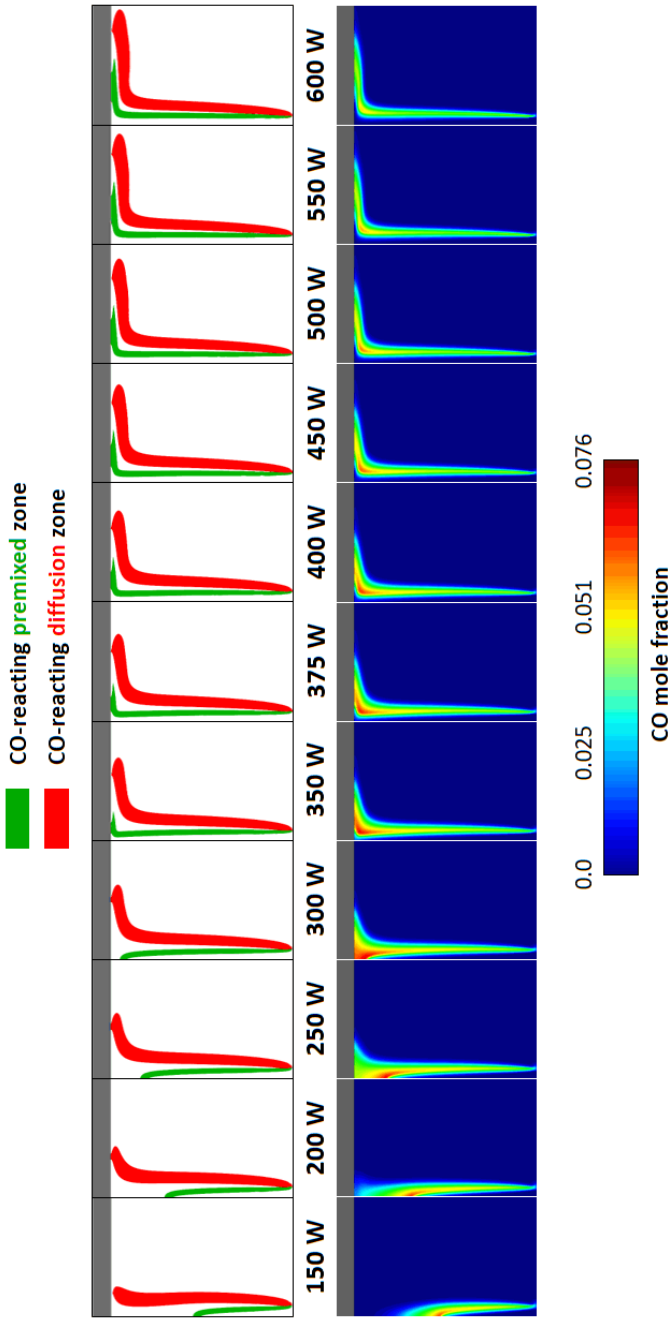

Figure 4.6: Evolution of the CO-reacting premixed and diffusion zones (top) and the corresponding volumetric concentration of CO (bottom) at different $\dot{P}$.

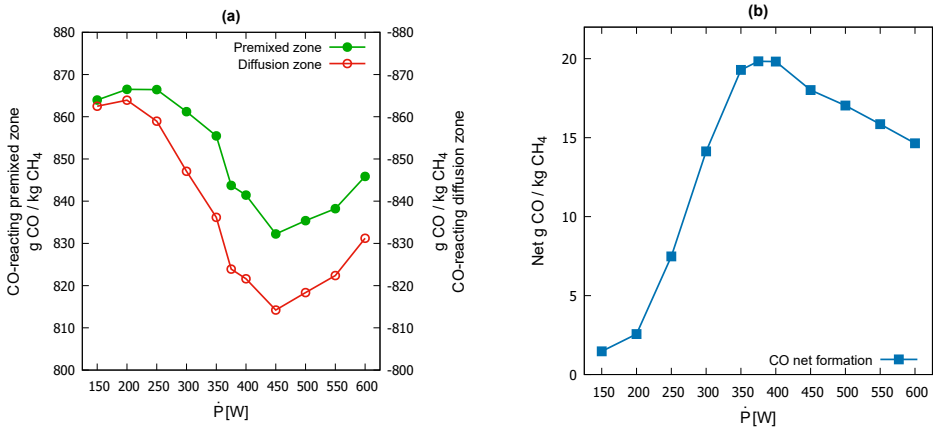

Figure 4.7: CO net formation at the CO-reacting premixed and diffusion zones (a) and the combination of both regions (b) at each $\dot{P}$.

A recovery in the growing of both the production in the premixed zone and the consumption in the diffusion zone can be observed from 450W on. The difference between every pair of values at each $\dot{P}$ equals to the net CO formation in the flame, shown in Figure 4.7b. These values are naturally in agreement with the COAF results previously observed in Figure 4.1. The maximum CO emission value occurs near a position where the largest difference between production and consumption occurs. From this point, the CO-reacting premixed zone starts to proportionally improve its radial expansion towards the lateral pot wall (Figure 4.6), which corroborates that the evolution of this region is intrinsically related to the development of the net CO emissions.

To clarify the correlation between the evolution of the zones from Figure 4.6 and CO emissions, their two-dimensional areas are also quantified and shown in Figure 4.8a. A linear growing can be observed for the size of the CO-reacting diffusion zone; nevertheless, the area growth rate of the CO-reacting premixed zone slows down from near $\dot{P}$=375 W onwards, the identified condition for the breakage of the inner premixed flame cone. Consequently, the ratio between the size of both zones (premixed over diffusion), shown in Figure 4.8b, tends to stabilize from that condition. This

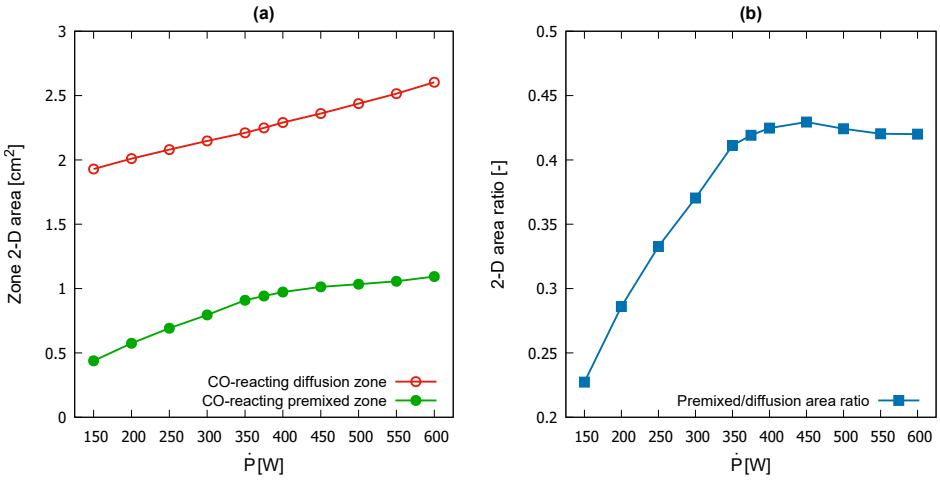

Figure 4.8: Two-dimensional areas of the CO-reacting premixed and diffusion zones (a) and the ratio between them (b) at each $\dot{P}$.

behavior agrees with the COAF trend from Figure 4.1. Then, the constrains for the evolution of the CO-reacting premixed zone due to the presence of the wall are responsible for the whole flame structure, modifying the local conditions (flow, temperature, species concentration) that drive the global CO net formation in the flame.

4.5 Effect on main CO chemical reactions

The weight of each CO-related chemical reaction on the global CO formation is evaluated and shown in this section for the three main $\dot{P}$ cases: 250, 375, and 500 W. The GRI-Mech 3.0 mechanism contains 61 chemical reactions (from the total of 325) for the CO kinetics description. The rate of each reaction (in kmol m^{-3} s^{-1}) can be normalized to represent the grams of CO produced per each kilogram of CH_4 entering the system[1]. By the volume integration of those values, the total amount of CO produced or consumed by any chemical reaction in a certain zone can be determined.

[1] This conversion is made by the multiplication of the reaction rate by the CO molecular weight, the corresponding cell volume, and the CH_4 inlet mass flow.

This evaluation can be made in the CO-reacting zones previously defined in section 4.4 and displayed in the top row of Figure 4.6. The 61 CO chemical reaction rates in the whole computational domain are shown in Appendix 4.C. The ten most important CO chemical reactions occurring in the CO-reacting premixed zone (pale green background) and the CO-reacting diffusion zone (pale red background) are shown in Figure 4.9 and Figure 4.10 respectively.

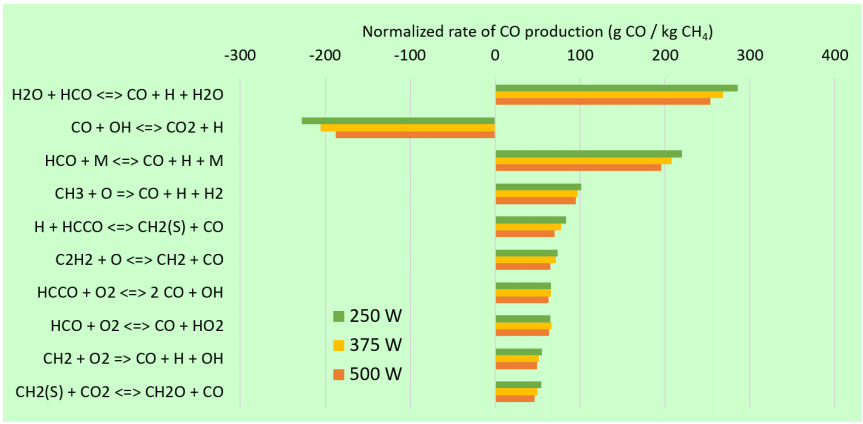

Figure 4.9: Normalized rates of the main CO chemical reactions in the CO-reacting premixed zone, for $\dot{P}$=250, 375, and 500 W.

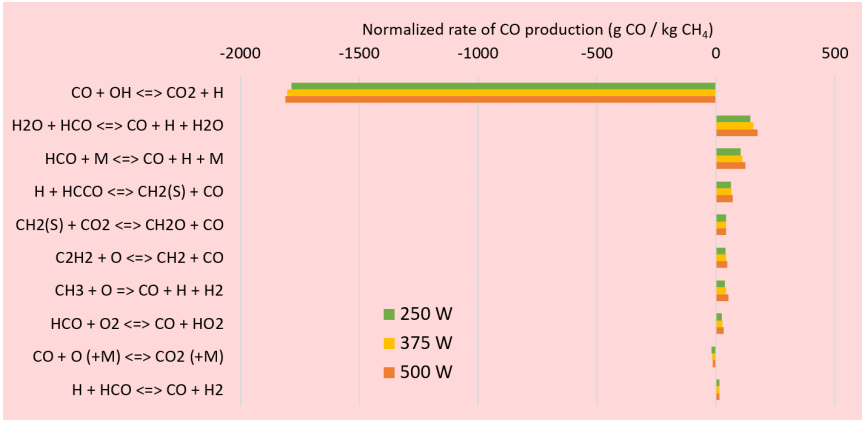

Figure 4.10: Normalized rates of the main CO chemical reactions in the CO-reacting diffusion zone, for $\dot{P}$=250, 375, and 500 W.

It can be observed that most of the chemical reactions occurring in the CO-reacting premixed zone are producing CO; on the contrary, CO is barely generated in the CO-reacting diffusion zone, but predominantly consumed and oxidized to CO_2. These results reinforce the previously mentioned finding about the predominance in the CO evolution in both premixed and diffusion zone (Figure 4.7a).

From all the CO chemical reactions, the CO consumption is clearly driven by its oxidation to CO_2 in the presence of the radical OH (reaction no.99 from the GRI-Mech 3.0 mechanism), with a great importance in both analyzed zones. Nevertheless, the generation of CO is distributed in a larger number of chemical reactions, where the radical HCO arises as the most significant intermediate C-species for the carbon monoxide formation.

These consumption and production main reactions are in agreement with those determined in a one-dimensional study of the chemical reaction pathways of methane combustion (see Appendix 4.A). However, this simple geometry is unable to accurately include multidimensional phenomena such as the flame impingement and the corresponding heat extraction due to the presence of a cold wall. It is a relevant fact to explain the weak points of those strategies which pre-calculate and storage the combustion reaction states using these 1-D flames such as the FGM model. The accurate evolution of radicals OH and HCO are essential to equally predict the CO evolution.

When $\dot{P}$ is modified, it can be observed that there are slight differences between the main production and consumption reactions, independently of the reaction zone. The higher intensity of the chemical reactions at low $\dot{P}$ in the CO-reacting premixed zone, with respect to the larger $\dot{P}$ cases, may be related to a lesser interaction of this region with the wall (Figure 4.6), allowing a greater completeness of the chemical reactions in this zone. Differences are even smaller in the CO-reacting diffusion zone, where a slightly higher intensity of the reactions is observed when the thermal power is larger. This fact can be also related to the evolution of this zone: as the flame grows, the CO-reacting premixed zone displaces the diffusion one, which moves away from the wall (Figure 4.6); therefore, the quenching

effect produced by the wall is reduced and the completeness of the chemical reactions achieves a higher grade.

As previously revealed in the integration of the reaction rates of CO in section 4.4, the global production of this pollutant is a consequence of the combination of the local conditions, shaped by the flow field, which alters the temperature field and the chemical species concentrations, leading to the corresponding reaction rates. A global integration of all these factors produces the final CO concentration measured at the top of the hood.

4.6 Conclusions

The influence of the flame-wall interaction phenomena on the flame structure and the carbon monoxide emissions is evaluated in this chapter. To do so, additional CFD simulations are carried out in order to obtain a more detailed evolution of CO emissions at intermediate values of flame thermal power. The following conclusions can be extracted from this extensive analysis:

1. The combination of the flame structure and CO emissions reveals a strong relationship between the inner premixed flame cone and CO production: for constant conditions and increasing flame thermal power, COAF rises as long as the cone is not affected by the wall. Once the flame is long enough and the rupture of the cone is produced due to its impingement with the pot ($\dot{P}$=375 W), COAF reaches its maximum value, with a subsequent smoother decrease if $\dot{P}$ keeps being raised. In general, this situation would be always observed in similar situations as long as the flame approaches the wall and is perturbed.

2. The thermal efficiency of the burner shows the same behavior as the CO emissions. Thus, for this type of configurations, there is a coincident operating point where the maximum thermal efficiency always gives the maximum CO emissions. This fact points out reachable design guidelines in both performance and emission thresholds, which shall be used in the development process of gas burners.

3. The reaction completeness of the combustion, determined either by the total consumption of O_2 or by the heat released from the whole flame, is in accordance with the CO behavior. The higher the combustion completeness is, the lower net quantity of carbon monoxide produced in the flame, and vice versa.

4. The study of the premixed and diffusion zones of the flame where carbon monoxide chemically reacts manifests that the final value of CO emissions is strongly driven by the flame structure resulting from its interaction with the wall. More precisely, it is mainly the propagation of the CO-reacting premixed zone which is constrained by the presence of the pot, leading to local conditions (flow, temperature, species concentration) that alter the CO net formation.

5. There are small differences between the main CO chemical reactions occurring inside the flame when the flame thermal power is modified. Then, it can be stated that the final emissions of carbon monoxide are a consequence of different local conditions, shaped by the flow field, temperature and chemical species concentration, which lead to the corresponding reaction rates.

Some of these conclusions are of great relevance for the design of domestic gas cooking burners. If a high value of burner thermal efficiency is sought, the conical premixed flame should be as close as possible to the pot bottom wall, by modifying either the burner thermal power or the distance from the burner ports to the pot. However, attention should be drawn to CO emissions, which will be also maximum in this operating scenario.

4.A Chemical reaction pathways of methane combustion

This appendix includes a preliminary study of the main chemical reaction pathways of methane combustion. This analysis has been possible thanks to a national research stay in the Numerical Fluid Dynamics Group (*gfm*), at the University of Zaragoza (Spain), which is a research group mainly dedicated to numerical modeling of fluid flow and energy.

The aim of this work is to determine which are the main species and chemical reactions involved in methane combustion, focusing on those that are key in the chemical description of carbon monoxide. To do so, the software ANSYS Chemkin-Pro [78] is employed to solve a simple, one-dimensional model. The chosen configuration is a burner-stabilized, laminar, premixed flame, which is often used to study chemical kinetics in a combustion environment. Such flames are effectively one-dimensional and can be made very steady, facilitating detailed experimental measurements of temperature and species profiles. The main characteristics of the selected model setup are listed below:

- Model: Premixed Laminar Burner-stabilized Flame
- Fuel: 100% CH_4
- Mechanism: GRI-Mech 3.0 (detailed chemistry for methane combustion)
- Pressure: 1 atm
- Ending axial position: 1 cm
- Inlet velocity: 10 cm/s
- Inlet temperature: 300 K
- Mixture composition: λ=Φ=1 (stoichiometric conditions)

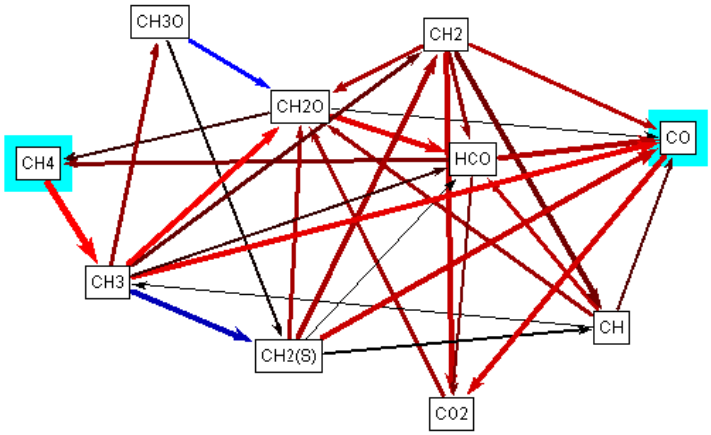

Figure 4.11: Main C-species participating in methane combustion.

Once the model is solved, the main chemical reaction pathways that lead to the formation of CO from CH_4 can be obtained with an extension of the software, the Reaction Path Analyzer. Figure 4.11 displays the main C-species that take part in the combustion process. The main pathways are:

- $CH_4 \rightarrow CH_3 \rightarrow CH_2O \rightarrow HCO \rightarrow CO$
- $CH_4 \rightarrow CH_3 \rightarrow CO$
- $CH_4 \rightarrow CH_3 \rightarrow CH_2(s) \rightarrow CH_2 \rightarrow CO$
- $CH_4 \rightarrow CH_3 \rightarrow CH_2(s) \rightarrow CO$

These results reinforce the selection of CH_3 as the optimal species to track the spatial starting of the combustion reaction when the fuel is pure methane. In addition, it can be outlined that species such as CH_2O, $CH_2(s)$, CH_2, and HCO are of great significance in the description of this combustion process.

From this calculation, the most important chemical reactions for the evolution of carbon monoxide can be also determined (Figure 4.12). These values are obtained in the axial position of the 1-D domain where the heat production is maximum.

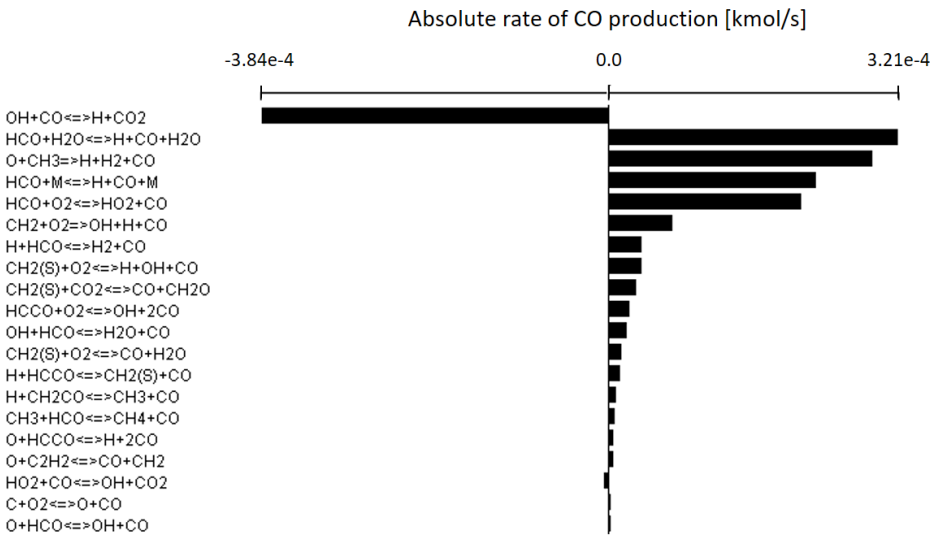

Figure 4.12: Normalized reaction rates of CO production in methane combustion from the one-dimensional flame

It can be observed that the CO is predominantly consumed by a unique reaction:

- OH + CO $\Leftrightarrow$ H + CO_2 (reaction no.99 from GRI-Mech 3.0)

On the contrary, the CO production is distributed in a higher number of chemical reactions, being the most important:

- HCO + H_2O $\Leftrightarrow$ H + CO + H_2O (reaction no.166 from GRI-Mech 3.0)
- O + CH_3 $\Rightarrow$ H + H_2 + CO (reaction no.284 from GRI-Mech 3.0)
- HCO + M $\Leftrightarrow$ H + CO + M (reaction no.167 from GRI-Mech 3.0)
- HCO + O_2 $\Leftrightarrow$ HO_2 + CO (reaction no.168 from GRI-Mech 3.0)

4.B Passive transported scalar

The definition of a passive transported scalar in ANSYS Fluent allows the tracking of any stream that enters the system. This marker is going to follow the flow coming from the corresponding inlet of boundary condition. To do so, an additional transport equation needs to be solved to capture all the relevant phenomena that the stream suffers: transient, convection, diffusion, etc. The procedure can be summarized in the following steps:

1. Enable a User-Defined Scalar (UDS) for all the fluid zones.
2. Define the boundary conditions of the scalar (γ). In this case:
   - Fuel and primary air stream $\rightarrow$ Scalar marker $\gamma = 1$.
   - Secondary air stream $\rightarrow$ Scalar marker $\gamma = 0$.
3. Define the diffusivity of the scalar as the mixture diffusivity. To do so, a User-Defined Function (UDF) is needed:

```
#include "udf.h"

DEFINE_DIFFUSIVITY(mean_diff,c,t,i)
{
        /* Schmidt number */
        #define Sch_t 0.7;
        float D_lam,D_tur,D_eff;
        D_lam = C_MU_L(c,t);
        D_tur = C_MU_T(c,t) / Sch_t;
        D_eff = D_lam + D_tur;
        return C_R(c,t) * D_eff;
}
```

   This UDF subroutine needs to be compiled and loaded by the code. Then, it must be referred in the corresponding UDS settings (*Materials* $\rightarrow$ *Mixture* $\rightarrow$ *UDS Diffusivity* $\rightarrow$ *Edit* $\rightarrow$ *user-defined* $\rightarrow$ *«name of the UDF»*).

4. In the Methods tab, enable the Second Order Upwind for the spatial discretization of the UDS.

5. Run the simulation. If the simulation had previously reached a convergence state, the equations for the solution of all the variables, except the added UDS, can be disabled.

The UDS allows the visualization of the distribution of primary and secondary air:

- UDS = 1 $\rightarrow$ 100% primary air, 0% secondary air.
- UDS = 0 $\rightarrow$ 0% primary air, 100% secondary air.

Then, given the local mass fraction of O_2 (Y_{O_2}), the corresponding fractions that come from the primary and the secondary streams can be determined by:

- $(Y_{O_2})_{prim} = Y_{O_2} * \gamma$
- $(Y_{O_2})_{sec} = Y_{O_2} * (1 - \gamma)$

4.C Normalized rates of CO per chemical reaction

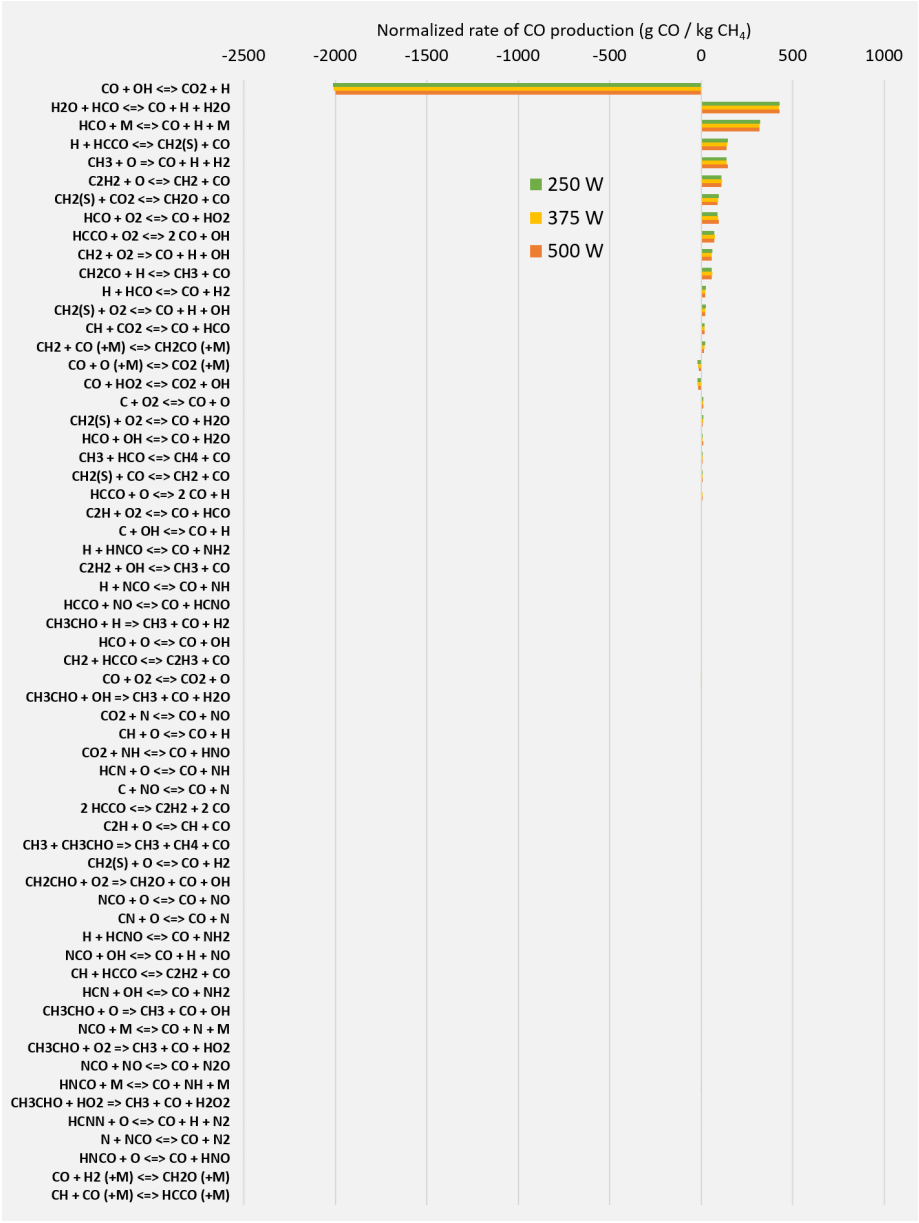

Figure 4.13: Normalized rates of CO per chemical reaction in the whole domain, for $\dot{P}$=250, 375, and 500 W.

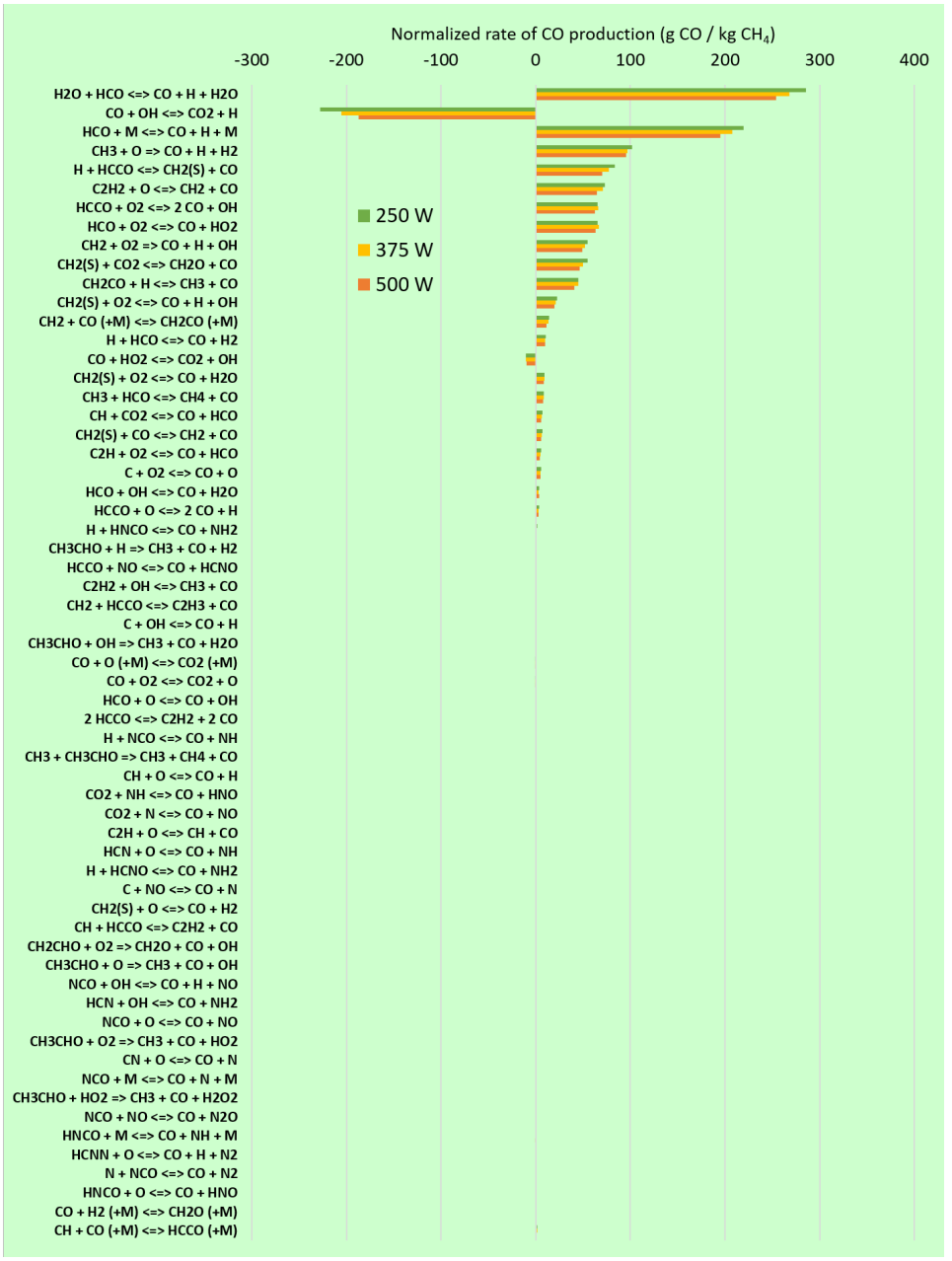

Figure 4.14: Normalized rates of CO per chemical reaction in the CO-reacting premixed zone, for $\dot{P}$=250, 375, and 500 W.

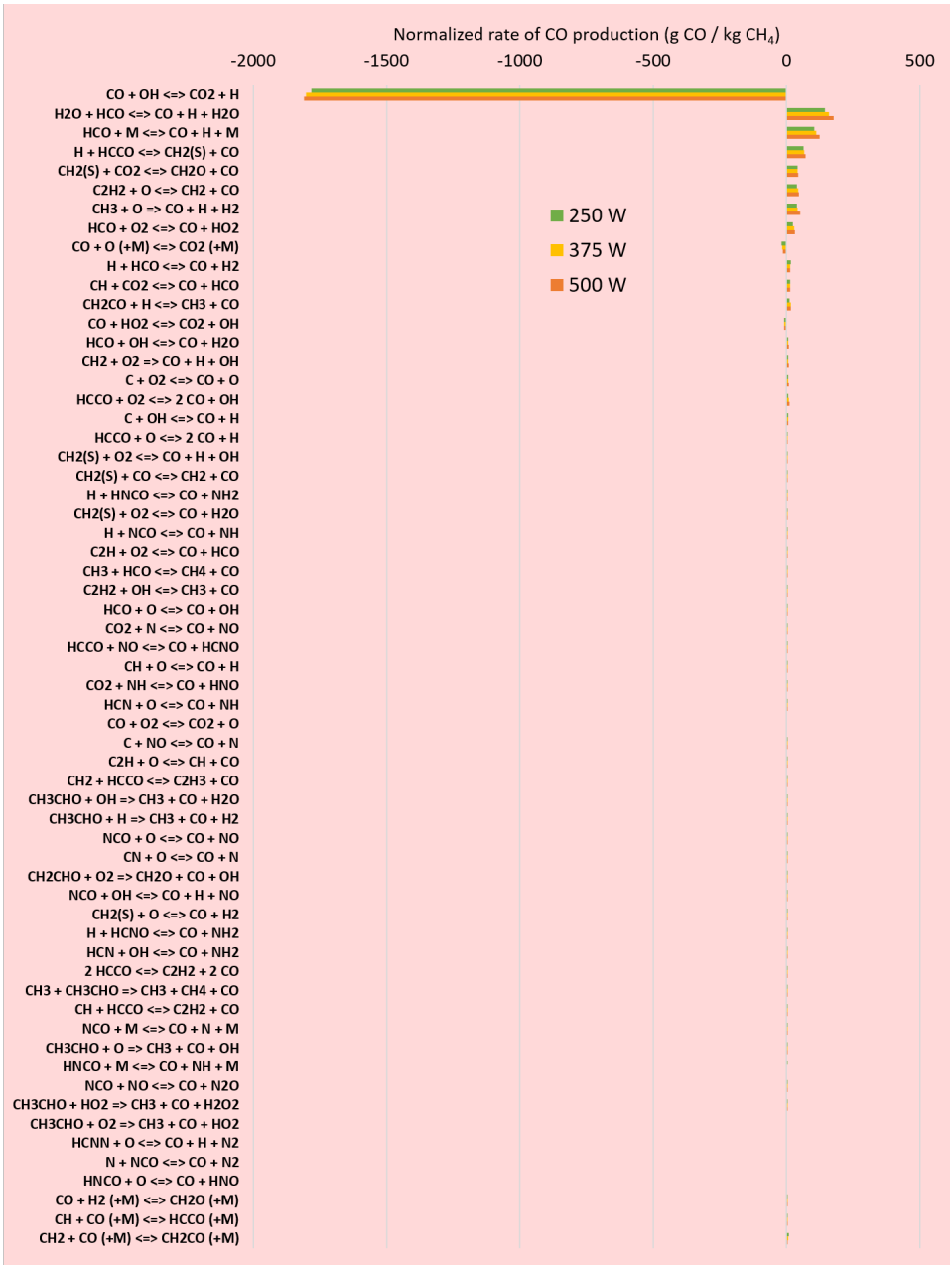

Figure 4.15: Normalized rates of CO per chemical reaction in the CO-reacting diffusion zone, for $\dot{P}$=250, 375, and 500 W.

Chapter 5

Concluding remarks

5.1 Conclusions

In this thesis, the methane combustion process is studied in depth by means of experimental and numerical analyses, focusing on the formation of carbon monoxide. The main goal of this research is to contribute in the comprehension of the main phenomena which are behind the formation of this pollutant during the combustion in a domestic gas cooking burner. In order to fulfill this objective, this work has been structured in three distinct parts that comprise: (i) the analysis of the state of the art of methane combustion chemistry models; (ii) the experimental and numerical evaluation of the carbon monoxide formation in a single methane flame burner; and (iii) the study of the relationships among the flame-wall interaction phenomena, the carbon monoxide emissions, and the thermal efficiency of the burner. The main conclusions drawn from this research are listed below:

- The numerical performance of the global, skeletal and detailed chemical reaction mechanisms for methane-air combustion simulation has been evaluated in three different configurations. The results show that global mechanisms should be only used for the description of the heat transfer processes; if an accurate prediction of chemical species

such as the CO is sought, skeletal mechanisms such as Smooke, Lu-sk17 or Lu-sk30 are good options to surrogate detailed chemistry. Naturally, the selection of the optimal mechanism is going to depend on the availability of computational resources and the required accuracy.

- A new skeletal mechanism has been created within the framework of this thesis. The SL11 mechanism was obtained after a reduction and an optimization process, and shows reasonably good results with a great speed-up of the calculations with respect to detailed chemistry. This mechanism is currently being used in simulations of domestic gas cooking burners which require lower computational times than those obtained with other skeletal and frequently employed options such as the Smooke mechanism.

- After the design and the validation of a new experimental facility, consisting of a single partially premixed methane flame impinging perpendicularly onto the bottom wall of a water pot, the influence of the modification of parameters of interest on the CO emissions has been evaluated in order to identify the main trends of the flame-wall interaction phenomena:

  - The increase of the inside-pot water temperature produces an analogous rise on the pot wall temperature, diminishing the quenching effect that the wall produces on the flame, which implies a reduction in CO emissions.
  - If the primary aeration of the burner is raised, the higher availability of oxygen in the partially premixed stream enhances the oxidation reactions, such as those where CO evolves towards CO_2, which is translated into final lower CO emissions.
  - When the burner-to-pot distance or the flame thermal power is modified, non-monotonic trends in CO emissions have been observed. This behavior is related to the modification of the flame structure resulting from its interaction with the wall.

  - The CO production is slightly influenced by the temperature of the solid parts that are in contact with the flame, but it is more strongly affected by the resulting structure of the flame produced by that impingement.

- By means of extending the computational analysis of the CO emissions for different values of the flame thermal power, a strong relationship between the internal structure of the flame and the carbon monoxide production has been revealed: CO emissions rise with an increase of $\dot{P}$ as long as the inner premixed flame cone is not affected by the wall; once the flame is long enough and the rupture of this cone is produced due to its impingement with the pot, CO emissions reach the maximum value, with a subsequent smoother decrease if $\dot{P}$ keeps being raised. The thermal efficiency of the burner shows the same behavior. Therefore, for this type of configurations, there is a coincident operating point where the maximum thermal efficiency is linked to the maximum CO emissions, which must be taken into account during the design of a new gas burner.

- The study of the premixed and diffusion zones of the flame where carbon monoxide chemically reacts confirms that the final value of CO emissions is strongly driven by the flame structure resulting from its interaction with the wall. More precisely, it is mainly the propagation of the CO-reacting premixed zone (where CO reacts with oxygen coming from the partially premixed stream) which is constrained by the presence of the pot. The analysis of the CO chemical reactions occurring inside the flame reinforces the conclusion that the final emissions of this pollutant are a consequence of the combination of the local conditions (flow, temperature, species concentration) determined by the flame structure, modifying the reaction rates and subsequently the CO net formation.

On the whole, these conclusions are of great relevance for the development of domestic gas cooking burners, pointing out reachable design

guidelines in both performance and emission thresholds.

5.2 Future research

The developments and results presented in this thesis are part of an ongoing work, which is expected to have a continuity in time. There are still challenges ahead and some future trends can be defined to continue with the research of this thesis. Further developments envisaged for the future include the following:

- Extend the analysis of carbon monoxide emissions with the single flame burner configuration utilizing other hydrocarbons frequently used as fuel in domestic gas cooking burners, such as propane or butane.

- Given that the flames in a domestic cooking burner do not impinge perpendicularly to the pot, there is a proposal to modify the distribution of the single flame burner configuration, leaning the burner or the pot in order to obtain an oblique flame and evaluate the effect of the impingement angle on the final CO emissions.

- Analyze the evolution of CO emissions and thermal efficiency with a real domestic gas cooking burner. To do so, the definition of a set of experimental tests in the laboratory and CFD calculations is proposed, covering wide ranges of the burner thermal power and the pan support height. The relationship between the results and the changes in the structure of the flames, constrained by the presence of solid parts such as the pot or the pan support, could be determined and compared to the findings of this thesis.

- Considering the actual concerns about the global warming, fossil fuels are being gradually replaced by using renewable sources. Regarding the decarbonization of domestic gas cooking burners, there is a strategy to surrogate hydrocarbon fuels by green gases such as hydrogen. Therefore, it is planned to extend the evaluation of this

thesis to fuel mixtures composed by different proportions of methane and hydrogen.

- Related to the previous proposal, and looking ahead to the utilization of other type of fuels in a domestic gas cooking burner, other pollutants that may arise should be taken into account. This is the case of the nitrogen oxides, which gain importance if the fuel contains hydrogen, for instance. Then, a complete review and performance evaluation of the available NOx chemistry models is also planned.

Conclusiones y trabajo futuro

Conclusiones

Esta tesis analiza en profundidad el proceso de combustión del metano mediante análisis experimentales y numéricos, centrándose en la formación del monóxido de carbono. El objetivo principal de esta investigación es contribuir a la comprensión de los principales fenómenos que están detrás de la formación de este contaminante durante la combustión en un quemador doméstico de gas. Para cumplir con este objetivo, este trabajo se ha estructurado en tres partes distintas que comprenden: (i) el análisis del estado del arte de los modelos cinéticos para la combustión del metano; (ii) la evaluación experimental y numérica de la formación de monóxido de carbono en un quemador de una única llama de metano; y (iii) el estudio de las relaciones entre los fenómenos de interacción llama-pared, las emisiones de monóxido de carbono y la eficiencia térmica del quemador. A continuación se enumeran las principales conclusiones extraídas de esta investigación:

- El comportamiento numérico de los mecanismos de reacción química globales, *skeletal* y detallados para la simulación de la combustión de metano se ha evaluado mediante tres configuraciones diferentes. Los resultados muestran que los mecanismos globales sólo deben utilizarse para la descripción de los procesos de transferencia de calor; si se busca una buena predicción de las especies químicas como el CO, los mecanismos *skeletal* como Smooke, Lu-sk17 o Lu-sk30 son buenas opciones para sustituir a la química detallada. Naturalmente, la

selección del mecanismo óptimo va a depender de la disponibilidad de recursos computacionales así como de la precisión requerida.

- En el marco de esta tesis se ha creado un nuevo mecanismo *skeletal*. El mecanismo SL11 se obtuvo tras un proceso de reducción y optimización, y muestra resultados razonablemente buenos con una gran aceleración de los cálculos con respecto a la química detallada. Este mecanismo se está utilizando actualmente en simulaciones de quemadores domésticos de cocción a gas que requieren tiempos de cálculo inferiores a los obtenidos con otras opciones frecuentemente empleadas como el mecanismo de Smooke.

- Después del diseño y la validación de un nuevo sistema experimental, que consiste en una llama de metano sencilla, parcialmente premezclada, que impacta perpendicularmente en la pared inferior de un recipiente lleno de agua, la influencia de la modificación de parámetros de interés en las emisiones de CO se ha evaluado con el objetivo de identificar las principales tendencias que provocan los fenómenos de interacción llama-pared:

  - El aumento de la temperatura del agua en el interior del recipiente provoca un incremento análogo de la temperatura de la pared, disminuyendo el efecto *quenching* que la pared produce en la llama, lo cual se traduce en una reducción de las emisiones de CO.
  - Si la aireación primaria del quemador aumenta, la mayor disponibilidad de oxígeno en la corriente parcialmente premezclada favorece las reacciones de oxidación, tales como esas en las que el CO evoluciona hacia CO_2, lo cual provoca menores emisiones de CO.
  - Cuando la distancia del quemador al recipiente o la potencia térmica de la llama se modifica, se han observado tendencias variables. Este comportamiento se relaciona con la modificación

de la estructura de la llama, resultante de su interacción con la pared.

- La producción de CO está ligeramente influenciada por la temperatura de las partes sólidas que están en contacto con la llama, pero se ve más afectada por la estructura resultante de la llama producida por ese impacto.

- Mediante la extensión del análisis computacional de las emisiones de CO para diferentes valores de potencia térmica de la llama, se ha revelado una fuerte relación entre la estructura interna de la llama y la producción de monóxido de carbono: las emisiones de CO aumentan con la potencia siempre y cuando el cono de premezcla interior de la llama no se vea afectado por la pared; una vez que la llama es lo suficientemente larga y se produce la ruptura de este cono debido a su impacto con el recipiente, las emisiones de CO alcanzan su valor máximo, con una ligera disminución posterior si la potencia sigue aumentando. La eficiencia térmica del quemador muestra el mismo comportamiento. Por lo tanto, para este tipo de configuraciones, existe una condición de funcionamiento en la que la máxima eficiencia térmica está ligada a las máximas emisiones de CO, lo cual debe tenerse en cuenta durante el diseño de un nuevo quemador de gas.

- El estudio de las zonas de premezcla y difusión de la llama donde el monóxido de carbono reacciona químicamente confirma que el valor final de las emisiones de CO está estrechamente relacionado con la estructura de la llama resultante de su interacción con la pared. Más concretamente, está principalmente ligado a la propagación de la zona de premezcla para el CO (donde el CO reacciona con el oxígeno procedente de la corriente parcialmente premezclada), que está limitada por la presencia del recipiente. El análisis de las reacciones químicas del CO que se producen en el interior de la llama refuerza la conclusión de que las emisiones finales de ese contaminante son consecuencia de la combinación de las condiciones

locales (flujo, temperatura, concentración de especies) determinadas por la estructura de la llama, que modifican las velocidades de reacción y, por consiguiente, la formación neta de CO.

En general, estas conclusiones son de gran relevancia para el desarrollo de los quemadores domésticos de cocción a gas, identificando pautas de diseño alcanzables relacionadas con el rendimiento y con los limites de emisión de contaminantes.

Trabajo futuro

Los avances y resultados presentados en esta tesis son parte de un trabajo en curso, que se espera que tenga continuidad en el futuro. Se pueden definir algunos retos y tendencias futuras para continuar con la investigación que ha dado lugar a esta tesis. Entre las actividades previstas para el futuro figuran las siguientes:

- Extender el análisis de las emisiones de monóxido de carbono con la configuración del quemador de llama única estudiando la combustión de otros hidrocarburos que se usan frecuentemente como combustible en los quemadores domésticos de cocción a gas, como el propano o el butano.

- Dado que las llamas de un quemador doméstico de gas no inciden de manera perpendicular al recipiente, se propone modificar la distribución del quemador de llama única, inclinando bien el quemador o bien el recipiente para obtener una llama oblicua y evaluar así el efecto del ángulo de incidencia en las emisiones finales de CO.

- Analizar la evolución de las emisiones de CO y la eficiencia térmica de un quemador real como los que forman parte de las cocinas de gas. Para ello, se propone la definición de un conjunto de pruebas experimentales en el laboratorio y cálculos computacionales mediante CFD, que abarquen amplios rangos de potencia térmica del quemador

y de altura de las parrillas. Con ello, se podría determinar la relación entre los resultados y los cambios en la estructura de las llamas, afectada por la presencia de partes sólidas como el recipiente o la parrilla, y comparar posteriormente con las tendencias mostradas en esta tesis.

- Considerando las preocupaciones actuales sobre el calentamiento global, los combustibles fósiles están siendo reemplazados gradualmente por el uso de fuentes renovables. En lo que respecta a la descarbonización de los quemadores de cocción a gas, existe una estrategia para sustituir los combustibles basados en hidrocarburos por gases limpios como el hidrógeno. Por lo tanto, se prevé ampliar este estudio mediante la utilización de mezclas compuestas por diferentes proporciones de metano e hidrógeno.

- En relación con la propuesta anterior, y de cara a la utilización de otro tipo de combustibles en un quemador doméstico de cocción a gas, hay que tener en cuenta nuevos contaminantes que puedan surgir. Es el caso de los óxidos de nitrógeno, que adquieren importancia si el combustible contiene hidrógeno, por ejemplo. Por lo tanto, también se plantea una revisión completa y una evaluación del comportamiento numérico de los modelos cinéticos para la predicción de NOx disponibles.

Appendix I

Mathematical model

I.1 Governing equations

The evolution of a mixed-gas system is governed by the flow dynamics, the chemical reactions and the turbulence modeling. The set of transport equations represent the conservation of mass, momentum, energy and chemical species. These governing equations are briefly described in this section. For more in-depth scientific detail, the reader may consult for example [125] or the software's corresponding manual ([78] for the 1-D configuration, [90] for 2-D and 3-D calculations).

The conservation equation for a generic variable ϕ (velocity components, enthalpy, energy, mass fractions...) that governs the fluid flow is

$$\frac{\partial(\rho\phi)}{\partial t} + \nabla \cdot (\rho\phi\vec{v}) - \nabla \cdot (\Gamma_\phi \nabla\phi) = S_\phi \ , \tag{I.1}$$

where ∇ is a vector differential operator $(\frac{\partial}{\partial x}, \frac{\partial}{\partial y}, \frac{\partial}{\partial z})$, ρ is the fluid density, $\vec{v} = (u, v, w)$ is the velocity vector, Γ_ϕ the diffusion coefficient and S_ϕ the source term. Both the fluid density and the diffusion coefficient are fluid properties. This conservation equation is also known as the transport equation. Hence, the first term is the temporal variation of ϕ, the second one is the convective term and the third one is the diffusive term.

Navier-Stokes equations

Mass and momentum conservation are described by the well-known Navier-Stokes equations. The PDE of the mass conservation is the so-called continuity equation,

$$\frac{\partial \rho}{\partial t} + \nabla \cdot (\rho \vec{v}) = 0 \ , \tag{I.2}$$

where ρ and $\vec{v}$ are the density and the velocity vector of the mixture respectively. Usually, in most of the combustion problems, the density is calculated using the ideal gas law as

$$\rho = \frac{P\overline{M}}{RT} \ , \tag{I.3}$$

with R being the universal gas constant, P the total pressure, T the temperature and $\overline{M}$ the average molecular weight of the mixture, defined as

$$\overline{M} = \left(\sum_{\alpha=1}^{N_\alpha} \frac{Y_\alpha}{M_\alpha} \right)^{-1} \ , \tag{I.4}$$

where Y_α and M_α are the mass fraction and the molecular weight of the species α respectively.

On the other hand, the momentum conservation is derived from the Newton's Second Law, and it is described by

$$\frac{\partial}{\partial t}(\rho \vec{v}) + \nabla \cdot (\rho \vec{v}\vec{v}) = -\nabla P + \nabla \cdot \tau + \rho f \ , \tag{I.5}$$

where f are the body forces acting on the fluid and τ is the viscous stress tensor related with the surface forces. In this type of problems, gravitational acceleration (g) is the only body force that has to be taken into account.

Since the mixture of gases can be considered as a Newtonian fluid, the

stress tensor is expressed as

$$\tau = \mu\left(\nabla\vec{v} + (\nabla\vec{v})'\right) - \frac{2}{3}\mu(\nabla\cdot\vec{v})I \ , \tag{I.6}$$

with μ being the dynamic viscosity and I the identity tensor.

Chemical species conservation

In a mixture of N_α species, the mass fraction of a single chemical species is defined by

$$Y_\alpha = \frac{m_\alpha}{m_T} \ , \tag{I.7}$$

where m_α is the mass of the species α and m_T is the total mass of the mixture. In terms of the mass fraction, the species conservation for a single species is described by

$$\frac{\partial}{\partial t}(\rho Y_\alpha) + \nabla\cdot(\rho\vec{v}Y_\alpha) = -\nabla\cdot J_\alpha + S_\alpha, \qquad \alpha = 1, ..., N_\alpha \ , \tag{I.8}$$

where J_α and S_α are the diffusive flux and the net formation rate of the species α respectively. The diffusive flux, J_α, has three components: the gradient of species, the gradient of temperature (Soret effect), and the gradient of pressure. The effect of temperature and pressure gradients is usually neglected in combustion fluxes [126]. Therefore, J_α only considers the mass diffusion due to the gradient of species, according to the Fick's Law. In terms of the Schmidt number, S_c, the diffusive flux of a species can be written as

$$J_\alpha = -\Gamma_\alpha\nabla Y_\alpha = -\frac{\mu}{S_{c_\alpha}}\nabla Y_\alpha \ , \tag{I.9}$$

where the Schmidt number of the species α, S_{c_α}, is defined by

$$S_{c_\alpha} = \frac{\mu}{D_\alpha \rho} \ , \tag{I.10}$$

being D_α the diffusion coefficient of the species α.

Energy conservation

Total energy in a fluid volume is, in general, the sum of internal energy u, kinetic energy k, and potential energy p:

$$e = u + k + p \ . \tag{I.11}$$

By introducing the relationship between internal energy u and enthalpy H, described as

$$u = \frac{H + PV}{m_T} \ , \tag{I.12}$$

where V is the total volume of the mixture, the conservation equation for the energy can be described with the following enthalpy transport equation:

$$\frac{\partial}{\partial t}(\rho h) + \nabla \cdot (\rho v h) = \frac{\partial P}{\partial t} + v \cdot \nabla P - \nabla \cdot J_h + \Phi_v + S_h \ . \tag{I.13}$$

Enthalpy h can be defined in terms of the specific enthalpy h_α of each species α, as:

$$h = \sum_{\alpha=1}^{N_\alpha} Y_\alpha h_\alpha \tag{I.14}$$

$$h_\alpha = h_\alpha^0 + \int_{T_0}^{T} C_{p,\alpha}(T) dT \ , \tag{I.15}$$

where $C_{p,\alpha}$ is the specific heat at constant pressure of species α and h^0_α the specific enthalpy of formation at the reference temperature, T_0.

Pressure terms in Eq. I.13 can be neglected in the context of this thesis because they are only relevant when large pressure gradients are present (e.g. detonation problems [126]). Besides, the term Φ_v, which represents the viscous dissipation, can be also neglected. Hence, Eq. I.13 is simplified as:

$$\frac{\partial}{\partial t}(\rho h) + \nabla \cdot (\rho \vec{v} h) = -\nabla \cdot J_h + S_h \ , \tag{I.16}$$

where J_h represents the heat diffusive flux and S_h accounts for any additional volumetric source term of enthalpy. The heat diffusive flux, J_h, has also three components: the gradient of temperature (Fourier's Law), the gradient of concentrations (Dufour effect) and the last one related with the diffusive flux of the chemical species. In combustion problems, the last two terms are often neglected [126]. Thus, the term J_h is expressed by the Fourier's Law as

$$J_h = -\kappa \nabla T \ , \tag{I.17}$$

being κ the thermal conductivity of the mixture.

I.2 Solution method

The computational fluid dynamics (CFD) uses numerical analysis to solve and analyze the governing equations of a fluid problem by means of its discretization. One of the most used methods to discretize the equations is the finite volume method (FVM).

The first phase of the FVM is the discretization of the spatial domain and time. It consists in dividing the fluid domain into as many control volumes as necessary for its correct resolution. Thereafter the differential governing equations are integrated over each control volume (cells).

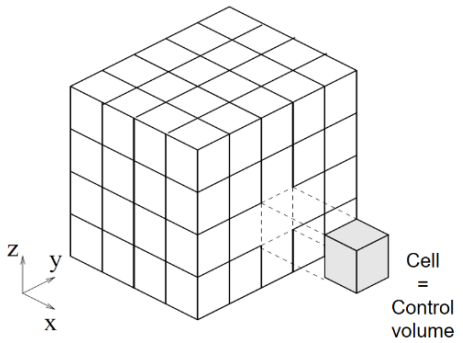

Figure I.1: Scheme of a discretized domain with an structured mesh of control finite volumes.

Continuing with the generic conservation equation for a variable ϕ (Equation I.1), the integral form for an arbitrary control volume V, limited by a surface A, is

$$\int_V \frac{\partial(\rho\phi)}{\partial t} dV + \oint \rho\phi\vec{v} \cdot \overrightarrow{dA} - \oint \Gamma_\phi \nabla\phi \cdot \overrightarrow{dA} = \int_V S_\phi dV \ . \tag{I.18}$$

The above equation turns into a spatial discretized form mainly in terms

of the faces of a volume V (subscript f) as

$$\frac{\partial(\rho\phi)}{\partial t}dV + \sum_f \rho_f \phi_f \vec{v}_f \cdot \overrightarrow{A_f} = \sum_f \Gamma_\phi (\nabla\phi)_f \cdot \overrightarrow{A_f} + S_\phi V \ . \tag{I.19}$$

In this study, the simulations are only in steady state regime, so Equation I.19 is simplified since the first term is equal to zero. The resultant equation is

$$\sum_f \rho_f \phi_f \vec{v}_f \cdot \overrightarrow{A_f} = \sum_f \Gamma_\phi (\nabla\phi)_f \cdot \overrightarrow{A_f} + S_\phi V \ . \tag{I.20}$$

In order to calculate the variable values at the control volume faces, an interpolation scheme is necessary. In general, the face value ϕ_f is calculated as

$$\phi_f = \phi + \nabla\phi \cdot \vec{r} \ , \tag{I.21}$$

where $\vec{r}$ is the displacement vector from the upstream cell centroid to the face centroid. The combination of Equation I.20 and Equation I.20 results in the expression that calculates the variable values in a certain cell P depending on the value in the neighboring cells (subscript nb), which is

$$a_P \phi = \sum_{nb} a_{nb} \phi_{nb} + b \ , \tag{I.22}$$

where a_P and a_{nb} are the linearized coefficients for ϕ and ϕ_{nb} respectively. The number of neighboring cells that has influence in the calculus of a cell P depends on the grid topology. However, excluding the boundary cells, the number of cells is usually equal to the number of cell faces.

Therefore, the governing equations are discretized using Equation I.22. The result of this discretization is a set of algebraic equations with a sparse coefficient matrix. Finally, they are solved using iterative methods.

Appendix II

Scientific contributions

In this appendix are listed the publications, the contributions presented at conferences, both internal (at BSH Home Appliances) and international, and the patents arisen during the predoctoral period.

II.1 Papers published in indexed journals

- **S. Laguillo**, J.S. Ochoa, A. Ortiz. "Chemical Reaction Mechanisms Assessment for Simulation of Methane Combustion in Domestic Gas Cooking Burners", *Energy & Fuels*, vol. 33, no. 9, pp. 9171-9183, 2019. https://doi.org/10.1021/acs.energyfuels.9b01598. Impact Factor (2019): 3.421, Q2.

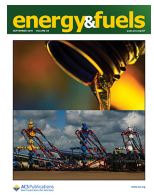

- **S. Laguillo**, J.S. Ochoa, A. Ortiz. "CO emissions and temperature analysis from an experimental and numerical study of partially premixed methane flames impinging onto a cooking pot". *Submitted (July 2020).*

II.2 Contributions to scientific meetings and conferences

- **S. Laguillo**. "Chemical reaction mechanisms for combustion simulation in gas burners", *BSH Simulation User Meeting 2016 (internal congress)*, 27-29th September, 2016, Santander (Spain). *Oral presentation.*

- J.S. Ochoa, **S. Laguillo**, C. Rueda, A. Cavada. "The simulation's 5-W questions", *BSH Gas Days (internal congress)*, 7-8th November, 2016, Santander (Spain). *Oral presentation.*

- J.S. Ochoa, **S. Laguillo**, C. Rueda, A. Cavada. "Accurate simulation of domestic gas burners: progress and challenges in BSH Santander", *5th Symposium on Fluid Dynamics (BOSCH internal congress)*, 10-11th October, 2017, Renningen (Germany). *Oral presentation.*

- **S. Laguillo**, J.S. Ochoa, A. Ortiz. "Numerical modelling of chemical reactions describing combustion in gas cooking burners", *VII Jornada en Santander de los Grupos de Investigación que colaboran con BSH Electrodomésticos España S.A. (internal congress)*, 13th September, 2018, Santander (Spain). *Oral presentation.*

- **S. Laguillo**, J.S. Ochoa, A. Ortiz. "Numerical simulation of a methane flame impinging onto a cooking pot", *11th Mediterranean Combustion Symposium*, 16-20th June, 2019, Tenerife (Spain). *Poster presentation.*

- **S. Laguillo**, J.S. Ochoa. "Toward decarbonization of domestic gas cooking burners by using renewable green gases", *6th Symposium on Fluid Dynamics (BOSCH internal congress)*, 12-13th February, 2020, Renningen (Germany). *Poster presentation.*

- **S. Laguillo**, J.S. Ochoa, A. Ortiz. "CO emissions in a single-flame burner impinging onto a cooking pot", *VIII Jornada en Santander de los Grupos de Investigación que colaboran con BSH Electrodomésticos*

España S.A. (internal congress), 12th February, 2020, Santander (Spain). *Oral presentation.*

II.3 Patents

- C. Aguado, J. Ballester, **S. Laguillo**, J.S. Ochoa, A. Pina, C. Rueda, D. Serrano, E. Tizné. "Gas burner for a gas hob". Application No. 20151949.3 - 1008, *issued 14th April 2020.*

Nomenclature

Roman Symbols

A	frequency factor, [depending on the reaction order]
C_p	specific heat, [J kg^{-1} K^{-1}]
d	injector inner diameter, [m]
D_α	diffusion coefficient of the species α, [m^2 s^{-1}]
D_{wire}	wire diameter, [m]
e	total energy, [J kg^{-1}]
E_a	activation energy for a reaction, [cal mol^{-1}, J mol^{-1}]
f	body forces vector, [m s^{-2}]
g	gravitational acceleration, [m s^{-2}]
H	height, [m]; enthalpy, [J]
h	enthalpy, [J kg^{-1}]
h_s	gross calorific value, [J kg^{-1}]
h_α	specific enthalpy for the species α, [J kg^{-1}]
h^0_α	specific enthalpy of formation for the species α at T_0, [J mol^{-1}]
I	identity tensor, [-]

J_α	diffusive flux of the species α, [kg m^{-2} s^{-1}]
J_h	heat diffusive flux, [W m^{-2} s^{-1}]
k	kinetic energy, [J kg^{-1}]
k_f	reaction rate coefficient, [depending on the reaction order]
$\dot{m}$	mass flow rate, [kg s^{-1}]
$\overline{M}$	average molecular weight of the mixture, [kg kmol^{-1}]
m_e	equivalent mass of the pan filled, [kg]
m_T	total mass of the mixture, [kg]
M_α	molecular weight of the species α, [kg kmol^{-1}]
m_α	mass of the species α, [kg]
N	number of sampling points
N_α	number of chemical species
P	pressure, [Pa]
p	potential energy, [J kg^{-1}]
$\dot{P}$	flame thermal power, [W]
P_{gauge}	gauge pressure, [Pa]
Q	power load, [W]
q	heat flux, [W m^{-2}]
R	universal gas constant, [cal mol^{-1} K^{-1}, J mol^{-1} K^{-1}]
Re	Reynolds number, [-]
S_α	net formation of the species α, [kg m^{-3} s^{-1}]
S_c	Schmidt number, [-]

S_h	Volumetric source of enthalpy, [J m^{-3}]
T	temperature, [K]
t	time, [s]
T_0	reference temperature, [K]
T_∞	bulk temperature, [K]
T_{TC}	temperature measured by the thermocouple, [K]
u	internal energy, [J kg^{-1}]
V	total volume of the mixture, [m^3]
v	velocity magnitude, [m s^{-1}]
$\vec{v}$	flow velocity vector, [m s^{-1}]
V_c	volume of dry gas consumed, [m^3]
v_{rms}	root-mean-square velocity, [m s^{-1}]
x	axial distance, [m]
$\hat{y}_i$	predicted value
y_i	reference/experimental value
Y_α	mass fraction of the species α, [-]

Greek Symbols

β	temperature exponent, [-]
ϵ	emissivity, [-]
η	thermal efficiency, [%]
κ	thermal conductivity, [W m^{-1} K^{-1}]
λ	primary aeration, [-]
μ	dynamic viscosity, [kg m^{-1} s^{-1}]
ρ	density, [kg m^{-3}]
σ	Stefan-Boltzmann constant, [W m^{-2} K^{-4}]
σ_w	weighted standard deviation, [-]
τ	viscous stress tensor, [s^{-1}]
ϕ	generic variable
Φ	equivalence ratio, [-]
Φ_v	viscous dissipation term, [W m^{-3}]
ω	specific turbulence dissipation, [s^{-1}]

Subscripts

M	measured (referred to combustion products)
N	neutral (referred to combustion products)

Abbreviations and acronyms

AFR	Air-Fuel Ratio
BC	Baseline Case
CAD	Computer-Aided Design
CFD	Computational Fluid Dynamics
COAF	CO Air Free
DOM	Discrete-Ordinate Model
DRG	Directed Relation Graph
FGM	Flamelet Generated Manifold
FWI	Flame-Wall Interaction
GGs	Greenhouse Gases
GRI	Gas Research Institute
HTC	Heat Transfer Coefficient
LFS	Laminar Flame Speed
LIF	Laser Induced Fluorescence
LPG	Liquefied Petroleum Gas
NDIR	Non-Dispersive InfraRed
NG	Natural Gas
PID	Proportional, Integral, Derivative
PRESTO	PREssure STaggering Option
PTFE	PolyTetraFluoroEthylene
QSS	Quasi-Steady State

RMSE	Root Mean Square Error
SST	Shear Stress Transport
SW	Side Wall
UDF	User-Defined Function
UDS	User-Defined Scalar

References

[1] S. Faramawy, T. Zaki, and A.-E. Sakr, "Natural gas origin, composition, and processing: A review," *J. Nat. Gas Sci. Eng.*, vol. 34, pp. 34 – 54, 2016.

[2] "International Energy Agency (IEA), World Energy Outlook 2019, Paris." `https://www.iea.org/reports/world-energy-outlook-2019`. *Accessed: 2020/07/04.*

[3] BP, "Statistical Review of Global Energy (2019)." `https://www.bp.com/en/global/corporate/energy-economics/statistical-review-of-world-energy.html`. *Accessed: 2020/07/06.*

[4] "U.S. Energy Information Administration (EIA), Natural Gas Explained: Use of Natural Gas (2018)." `https://www.eia.gov/energyexplained/index.php?page=natural_gas_use`. *Accessed: 2020/07/04.*

[5] "Eurostat: Statistics Explained, Energy consumption in households (March 2018)." `http://ec.europa.eu/eurostat/statistics-explained/index.php/Energy_consumption_in_households`. *Accessed: 2018/07/19.*

[6] "U.S. Energy Information Administration (EIA), Annual Energy Outlook 2020." `https://www.eia.gov/outlooks/aeo/`. *Accessed: 2020/07/04.*

[7] "International Energy Agency (IEA), CO2 Emissions from Fuel Combustion 2018, Paris." https://www.oecd-ilibrary.org/energy/co2-emissions-from-fuel-combustion-2018_co2_fuel-2018-en. *Accessed: 2020/07/04.*

[8] A. Basile, F. Dalena, and C. Rossi, "Preface," in *Bioenergy Systems for the Future* (F. Dalena, A. Basile, and C. Rossi, eds.), pp. XV – XVII, Woodhead Publishing, 2017.

[9] D. Penney, V. Benignus, S. Kephalopoulos, D. Kotzias, M. Kleinman, and A. Verrier, "Carbon monoxide," in *WHO Guidelines for Indoor Air Quality: Selected Pollutants*, ch. 2, pp. 55–101, Geneva: World Health Organization, 2010. https://www.ncbi.nlm.nih.gov/books/NBK138710, *Accessed: 2020/07/07.*

[10] P. Vanezis, "Forensic aspects of asphixia and drowning," in *Essential Forensic Medicine* (Vanezis, Peter, ed.), p. 158, John Wiley & Sons Ltd., 2020.

[11] European Standard, EN 30-1-1:2009-10: Domestic cooking appliances burning gas - Part 1-1: Safety - General, October 2009.

[12] European Standard, EN 30-2-1:1998+A1:2003+A2:2005: Domestic cooking appliances burning gas - Part 2-1: Rational use of energy - General, August 2005.

[13] Z. Wei, H. Zhen, C. Leung, C. Cheung, and Z. Huang, "Effects of H2 addition on the formation and emissions of CO/NO2/NOx in the laminar premixed biogas-hydrogen flame undergoing the flame-wall interaction," *Fuel*, vol. 259, p. 116257, 2020.

[14] R. Palulli, M. Talei, and R. L. Gordon, "Unsteady flame–wall interaction: Impact on CO emission and wall heat flux," *Combust. Flame*, vol. 207, pp. 406 – 416, 2019.

[15] U. Makmool, S. Jugjai, and S. Tia, "Structures and performances of laminar impinging multiple premixed LPG–air flames," *Fuel*, vol. 112, pp. 254 – 262, 2013.

[16] S. Rao, *The Finite Element Method in Engineering*. Elsevier Science, 2011.

[17] S. Mazumder, "Chapter 6 - The Finite Volume Method (FVM)," in *Numerical Methods for Partial Differential Equations* (S. Mazumder, ed.), pp. 277 – 338, Academic Press, 2016.

[18] BSH Home Appliances Group: Internal report, 2019.

[19] J. Blazek, *Computational Fluid Dynamics: Principles and Applications: Third Edition*. Elsevier, Jan. 2001.

[20] T. Lu and C. K. Law, "Toward accommodating realistic fuel chemistry in large-scale computations," *Prog. Energy Combust. Sci.*, vol. 35, no. 2, pp. 192 – 215, 2009.

[21] P. Boggavarapu, B. Ray, and R. Ravikrishna, "Thermal Efficiency of LPG and PNG-fired burners: Experimental and numerical studies," *Fuel*, vol. 116, pp. 709 – 715, 2014.

[22] H. Li, T. Wong, C. Leung, and S. Probert, "Thermal performances and CO emissions of gas-fired cooker-top burners," *Appl. Energy*, vol. 83, no. 12, pp. 1326 – 1338, 2006.

[23] H. Zhen, C. Leung, and T. Wong, "Improvement of domestic cooking flames by utilizing swirling flows," *Fuel*, vol. 119, pp. 153 – 156, 2014.

[24] U. Makmool, S. Jugjai, S. Tia, Y. Laoonual, P. Vallikul, and B. Fungtammasan, "Laser-based investigations of flow fields and OH distributions in impinging flames of domestic cooker-top burners," *Fuel*, vol. 90, no. 3, pp. 1024 – 1035, 2011.

[25] C. Westbrook and F. Dryer, "Simplified reaction mechanisms for the oxidation of hydrocarbon fuels in flames," *Combust. Sci. Technol.*, vol. 27, no. 1-2, pp. 31 – 43, 1981.

[26] W. Jones and R. Lindstedt, "Global reaction schemes for hydrocarbon combustion," *Combust. Flame*, vol. 73, no. 3, pp. 233 – 249, 1988.

[27] C. Montañés, *Development of the Flamelet-Generated Manifold model for the simulation of partially-premixed, non-adiabatic, laminar flames.* PhD thesis, Departamento de Ciencia y Tecnología de Materiales y Fluidos - Universidad de Zaragoza, November 2015.

[28] P. J. Ashman, R. Junus, J. F. Stubington, and G. D. Sergeant, "The effects of load height on the emissions from a natural gas-fired domestic cooktop burner," *Combust. Sci. Technol.*, vol. 103, no. 1-6, pp. 283–298, 1994.

[29] R. Junus, J. F. Stubington, and G. D. Sergeant, "The effects of design factors on emissions from natural gas cooktop burners," *Int. J. Environ. Stud.*, vol. 45, no. 2, pp. 101–121, 1994.

[30] J. Stubington, G. Sergeant, R. Junus, G. Beashel, T. Murphy, P. Ashman, and I. Tas, "Methodology for the simultaneous measurement of emissions and efficiency for natural gas-fired cooktop burners," *Int. J. Environ. Stud.*, vol. 48, no. 2, pp. 117–133, 1995.

[31] R. Junus, J. E. Vierkant, J. F. Stubington, G. D. Sergeant, and I. Tas, "The effects of the design of the cap of a natural gas-fired cooktop burner on flame stability," *Int. J. Energy Res.*, vol. 22, no. 2, pp. 175–184, 1998.

[32] R. Junus, J. F. Stubington, G. D. Sergeant, and I. Tas, "Emissions and efficiency of a prototype natural gas-fired domestic cooktop burner with insert," *Int. J. Environ. Stud.*, vol. 57, no. 2, pp. 189–205, 2000.

[33] Y.-C. Ko and T.-H. Lin, "Emissions and efficiency of a domestic gas stove burning natural gases with various compositions," *Energy Convers. Manag.*, vol. 44, no. 19, pp. 3001 – 3014, 2003.

[34] H. Li, T. Wong, C. Leung, and S. Probert, "Thermal performances and co emissions of gas-fired cooker-top burners," *Appl. Energy*, vol. 83, no. 12, pp. 1326 – 1338, 2006.

[35] Y. Zhang, C. Qin, H. Xing, and P. Liu, "Experimental research on performance response of domestic gas cookers to variable natural gas constituents," *J. Nat. Gas Sci. Eng.*, vol. 10, pp. 41 – 50, 2013.

[36] *Influence of Renewable Gas Addition to Natural Gas on the Combustion Performance of Cooktop Burners*, vol. Volume 8A: Heat Transfer and Thermal Engineering of *ASME International Mechanical Engineering Congress and Exposition*, 11 2018. V08AT10A012.

[37] Z. Chen, Y. Zhang, C. Qin, and P. Duan, "Combustion performance of domestic gas cookers with swirling strip-port and normal round-port on various natural gas compositions," *Case Stud. Therm. Eng.*, vol. 13, p. 100366, 2019.

[38] S.-S. Hou and Y.-C. Ko, "Effects of heating height on flame appearance, temperature field and efficiency of an impinging laminar jet flame used in domestic gas stoves," *Energy Convers. Manag.*, vol. 45, no. 9, pp. 1583 – 1595, 2004.

[39] S.-S. Hou, C.-Y. Lee, and T.-H. Lin, "Efficiency and emissions of a new domestic gas burner with a swirling flame," *Energy Convers. Manag.*, vol. 48, no. 5, pp. 1401 – 1410, 2007.

[40] C. Lacour, D. Honoré, A. Boukhalfa, and R. Hauguel, "Stabilization Mechanisms of Laminar Partially Premixed Flames from Domestic-Like Burner," *Combust. Sci. Technol.*, vol. 180, no. 1, pp. 156–175, 2007.

[41] L. Gattei, *A study on the fluid dynamics of domestic gas burners*. PhD thesis, Alma Mater Studiorum - Universita' di Bologna, 2008.

[42] J. Bibrzycki, T. Poinsot, and A. Zajdel, "Investigation of laminar flame speed of CH4/N2/O2 and CH4/CO2/O2 mixtures using reduced chemical kinetic mechanisms," *Arch. Combust.*, vol. 30, no. 4, pp. 287 – 296, 2010.

[43] H. Yapici, N. Kayatas, B. Albayrak, and G. Bastürk, "Numerical calculation of local entropy generation in a methane–air burner," *Energy Convers. Manag.*, vol. 46, no. 11, pp. 1885 – 1919, 2005.

[44] I. B. Özdemir, "Simulation of turbulent combustion in a self-aerated domestic gas oven," *Appl. Therm. Eng.*, vol. 113, pp. 160 – 169, 2017.

[45] A. Larsson, N. Zettervall, T. Hurtig, E. J. K. Nilsson, A. Ehn, P. Petersson, M. Alden, J. Larfeldt, and C. Fureby, "Skeletal methane–air reaction mechanism for large eddy simulation of turbulent microwave-assisted combustion," *Energy Fuels*, vol. 31, no. 2, pp. 1904–1926, 2017.

[46] N. F. A. Cubero, C. Montañés, "A flamelet generated manifold model for partially premixed laminar flames," in *11th OpenFoam Workshop*, pp. 189–190, 2016.

[47] A. Cavada, "Optimization of the geometry of domestic gas burner injectors by using the design exploration process," Master's thesis, University of Cantabria, Feb. 2019. Thesis for: Master in Mathematics and Computation.

[48] G. Smith, D. Golden, M. Frenklach, N. Moriarty, B. Eiteneer, M. Goldenberg, C. Bowman, R. Hanson, S. Song, W. Gardiner Jr., V. Lissianski, and Z. Qin, "GRI-Mech Version 3.0 (1999)." available from: `http://combustion.berkeley.edu/gri-mech/version30/text30.html` (accessed August 19, 2019).

[49] J. Andersen, C. Rasmussen, T. Giselsson, and P. Glarborg, "Global combustion mechanisms for use in CFD modeling under oxy-fuel conditions," *Energy Fuels*, vol. 23, no. 3, pp. 1379 – 1389, 2009.

[50] M. Smooke and V. Giovangigli, "Formulation of the premixed and nonpremixed test problems," in *Reduced Kinetic Mechanisms and Asymptotic Approximations for Methane-Air Flames* (M. Smooke, ed.), vol. 384 of *Lecture Notes in Physics*, pp. 61, 77, 201, Springer-Verlag, 1991.

[51] T. Lu, "Reduced mechanisms download (2018)." `http://spark.engr.uconn.edu/mechs/mechs.htm`. *Accessed: 2018/03/01.*

[52] R. Sankaran, E. Hawkes, J. Chen, T. Lu, and C. Law, "Structure of a spatially developing turbulent lean methane-air bunsen flame," *Proc. Combust. Inst.*, vol. 31, pp. 1291 – 1298, 2007.

[53] A. Kazakov and M. Frenklach, "Reduced reaction sets based on GRI-Mech 1.2 (1994)." `http://combustion.berkeley.edu/drm/`. *Accessed: 2018/03/01.*

[54] E. Gimeno-Escobedo, A. Cubero, J. S. Ochoa, and N. Fueyo, "A reduced mechanism for the prediction of methane-hydrogen flames in cooktop burners," *Int. J. Hydrog. Energy*, vol. 44, no. 49, pp. 27123 – 27140, 2019.

[55] T. Lu and C. Law, "A criterion based on computational singular perturbation for the identification of quasi steady state species: A reduced mechanism for methane oxidation with NO chemistry," *Combust. Flame*, vol. 154, no. 4, pp. 761 – 774, 2008.

[56] M. Frenklach, H. Wang, C.-L. Yu, M. Goldenberg, C. Bowman, R. Hanson, D. Davidson, E. Chang, G. Smith, D. Golden, W. Gardiner, and V. Lissianski, "GRI-Mech Version 1.2 (1994)." `http://combustion.berkeley.edu/gri-mech/new21/version12/text12.html`. *Accessed: 2018/03/01.*

[57] K. Hughes, T. Turányi, A. Clague, and M. Pilling, "Development and testing of a comprehensive chemical mechanism for the oxidation of methane," *Int. J. Chem. Kinet.*, vol. 33, no. 9, pp. 513 – 538, 2001.

[58] C. Bowman, R. Hanson, D. Davidson, W. Gardiner Jr., V. Lissianski, G. Smith, D. Golden, M. Frenklach, and M. Goldenberg, "GRI-Mech Version 2.11 (1995)." `http://combustion.berkeley.edu/gri-mech/new21/version21/text21.html`. *Accessed: 2018/03/01.*

[59] T. Turányi, "Sensitivity analysis of complex kinetic systems. Tools and applications," *J. Math. Chem.*, vol. 5, no. 3, pp. 203 – 248, 1990.

[60] H. Wang and M. Frenklach, "Detailed reduction of reaction mechanisms for flame modeling," *Combust. Flame*, vol. 87, no. 3, pp. 365 – 370, 1991.

[61] T. Lu and C. Law, "A directed relation graph method for mechanism reduction," *Proc. Combust. Inst.*, vol. 30, no. 1, pp. 1333 – 1341, 2005.

[62] P. Pepiot-Desjardins and H. Pitsch, "An efficient error-propagation-based reduction method for large chemical kinetic mechanisms," *Combust. Flame*, vol. 154, no. 1, pp. 67 – 81, 2008.

[63] W. Sun, Z. Chen, X. Gou, and Y. Ju, "A path flux analysis method for the reduction of detailed chemical kinetic mechanisms," *Combust. Flame*, vol. 157, no. 7, pp. 1298 – 1307, 2010.

[64] X. Zheng, T. Lu, and C. Law, "Experimental counterflow ignition temperatures and reaction mechanisms of 1,3-butadiene," *Proc. Combust. Inst.*, vol. 31, no. 1, pp. 367 – 375, 2007.

[65] K. E. Niemeyer, C.-J. Sung, and M. P. Raju, "Skeletal mechanism generation for surrogate fuels using directed relation graph with error propagation and sensitivity analysis," *Combust. Flame*, vol. 157, no. 9, pp. 1760 – 1770, 2010.

[66] Y. Li, C.-W. Zhou, K. P. Somers, K. Zhang, and H. J. Curran, "The oxidation of 2-butene: A high pressure ignition delay, kinetic modeling study and reactivity comparison with isobutene and 1-butene," *Proc. Combust. Inst.*, vol. 36, no. 1, pp. 403 – 411, 2017.

[67] H. Wang, X. You, A. V. Joshi, S. G. Davis, A. Laskin, F. Egolfopoulos, and C. K. Law, "USC Mech Version II. High-Temperature Combustion Reaction Model of H2/CO/C1-C4 Compounds.." `http://ignis.usc.edu/USC_Mech_II.htm`, May 2007. *Accessed: 2019/01/24.*

[68] ""Chemical-Kinetic Mechanisms for Combustion Applications", San Diego Mechanism web page, Mechanical and Aerospace Engineering (Combustion Research), University of California at San Diego (http://combustion.ucsd.edu)." *Accessed: 2019/01/24.*

[69] T. Turányi, A. Tomlin, and M. Pilling, "On the error of the quasi-steady-state approximation," *J. Phys. Chem.*, vol. 97, no. 1, pp. 163 – 172, 1993.

[70] C. Sung, C. Law, and J.-Y. Chen, "An augmented reduced mechanism for methane oxidation with comprehensive global parametric validation," *Symp. (Int.) Combust.*, vol. 27, pp. 295 – 304, 1998.

[71] T. Mendiara, M. U. Alzueta, A. Millera, and R. Bilbao, "An augmented reduced mechanism for methane combustion," *Energy Fuels*, vol. 18, no. 3, pp. 619–627, 2004.

[72] T. Jaravel, *Prediction of pollutants in gas turbines using Large Eddy Simulation.* PhD thesis, Institut National Polytechnique de Toulouse - Université de Toulouse, April 2016.

[73] B. Franzelli, E. Riber, L. Gicquel, and T. Poinsot, "Large Eddy Simulation of combustion instabilities in a lean partially premixed swirled flame," *Combust. Flame*, vol. 159, no. 2, pp. 621 – 637, 2012.

[74] "Sandia National Laboratories, International workshop on measurement and computation of turbulent nonpremixed

flames." `http://www.sandia.gov/TNF/chemistry.html`. *Accessed: 2018/03/22.*

[75] H. Jones, "Partially aerated burners," in *The application of combustion principles to domestic gas burner design* (H. Jones, ed.), p. 35, E. & F.N. Spon Ltd, 1989.

[76] S. Taylor, *Burning velocity and the influence of flame stretch.* PhD thesis, Department of Fuel and Energy - The University of Leeds, September 1991.

[77] C. Vagelopoulos, F. Egolfopoulos, and C. Law, "Further considerations on the determination of laminar flame speeds with the counterflow twin-flame technique," *Symp. (Int.) Combust.*, vol. 25, pp. 1341 – 1347, 1994.

[78] ANSYS, Inc., "ANSYS Chemkin-Pro Theory Manual, release 18.2," 2017.

[79] R. Santoro, H. Semerjian, and R. Dobbins, "Soot particle measurements in diffusion flames," *Combust. Flame*, vol. 51, pp. 203 – 218, 1983.

[80] C. McEnally and L. Pfefferle, "Aromatic and linear hydrocarbon concentration measurements in a non-premixed flame," *Combust. Sci. Technol.*, vol. 116-117, no. 1-6, pp. 183 – 209, 1996.

[81] C. McEnally, U. Köylü, L. Pfefferle, and D. Rosner, "Soot volume fraction and temperature measurements in laminar nonpremixed flames using thermocouples," *Combust. Flame*, vol. 109, no. 4, pp. 701 – 720, 1997.

[82] C. McEnally and L. Pfefferle, "Soot formation in methane/air nonpremixed flames doped with small quantities of C3 hydrocarbons," *Combust. Flame*, vol. 112, no. 4, pp. 545 – 558, 1998.

[83] C. McEnally and L. Pfefferle, "Species and soot concentration measurements in a methane/air nonpremixed flame doped with C4 hydrocarbons," *Combust. Flame*, vol. 115, no. 1, pp. 81 – 92, 1998.

[84] C. McEnally, A. Schaffer, M. Long, L. Pfefferle, M. Smooke, M. Colket, and R. Hall, "Computational and experimental study of soot formation in a coflow, laminar ethylene diffusion flame," *Symp. (Int.) Combust.*, vol. 27, pp. 1497 – 1505, 1998.

[85] C. McEnally and L. Pfefferle, "Flow time effects on hydrocarbon growth and soot formation in coflowing methane/air non-premixed flames," *Symp. (Int.) Combust.*, vol. 27, pp. 1539 – 1547, 1998.

[86] M. Smooke, C. McEnally, L. Pfefferle, R. Hall, and M. Colket, "Computational and experimental study of soot formation in a coflow, laminar diffusion flame," *Combust. Flame*, vol. 117, no. 1, pp. 117 – 139, 1999.

[87] C. McEnally and L. Pfefferle, "Comparison of non-fuel hydrocarbon concentrations measured in coflowing nonpremixed flames fueled with small hydrocarbons," *Combust. Flame*, vol. 117, no. 1, pp. 362 – 372, 1999.

[88] C. McEnally and L. Pfefferle, "Experimental study of nonfuel hydrocarbon concentrations in coflowing partially premixed methane/air flames," *Combust. Flame*, vol. 118, no. 4, pp. 619 – 632, 1999.

[89] B. Bennett, C. McEnally, L. Pfefferle, and M. Smooke, "Computational and experimental study of axisymmetric coflow partially premixed methane/air flames," *Combust. Flame*, vol. 123, no. 4, pp. 522 – 546, 2000.

[90] ANSYS, Inc., "ANSYS Fluent Theory and User's Guide, release 18.2," 2017.

[91] "About BSH, Company Portrait." `https://www.bsh-group.com/company/company-portrait`. *Accessed: 2020/07/05.*

[92] A. G. Barnston, "Correspondence among the correlation, RMSE, and Heidke forecast verification measures; refinement of the Heidke score," *Weather Forecast.*, vol. 7, no. 4, pp. 699–709, 1992.

[93] D. A. Sheen and H. Wang, "The method of uncertainty quantification and minimization using polynomial chaos expansions," *Combust. Flame*, vol. 158, no. 12, pp. 2358 – 2374, 2011.

[94] S. Laguillo, J. S. Ochoa, and A. Ortiz, "Chemical Reaction Mechanisms Assessment for Simulation of Methane Combustion in Domestic Gas Cooking Burners," *Energy Fuels*, vol. 33, no. 9, pp. 9171–9183, 2019.

[95] S. Chander and A. Ray, "Influence of Burner Geometry on Heat Transfer Characteristics of Methane/Air Flame Impinging on Flat Surface," *Exp. Heat Transf.*, vol. 19, no. 1, pp. 15 – 38, 2006.

[96] V. Hindasageri, R. P. Vedula, and S. V. Prabhu, "Heat transfer distribution for impinging methane–air premixed flame jets," *Appl. Therm. Eng.*, vol. 73, no. 1, pp. 461 – 473, 2014.

[97] *Investigation of Effect of Burner Diameter on Heat Transfer Characteristics of Methane/Air Flame Impinging on a Flat Surface*, vol. Heat Transfer: Volume 1 of *ASME 2005 Summer Heat Transfer Conference collocated with the ASME 2005 Pacific Rim Technical Conference and Exhibition on Integration and Packaging of MEMS, NEMS, and Electronic Systems*, July 2005.

[98] S. Chander and A. Ray, "An experimental and numerical study of stagnation point heat transfer for methane/air laminar flame impinging on a flat surface," *Int. J. Heat Mass Transf.*, vol. 51, no. 13, pp. 3595 – 3607, 2008.

[99] S. Chander and A. Ray, "Experimental and numerical study on the occurrence of off-stagnation peak in heat flux for laminar methane/air flame impinging on a flat surface," *Int. J. Heat Mass Transf.*, vol. 54, no. 5, pp. 1179 – 1186, 2011.

[100] M. Morad, A. Momeni, E. E. Fordoei, and M. Ashjaee, "Experimental and numerical study on heat transfer characteristics for methane/air flame impinging on a flat surface," *Int. J. Therm. Sci.*, vol. 110, pp. 229 – 240, 2016.

[101] S. Tuttle, B. Webb, and M. McQuay, "Convective heat transfer from a partially premixed impinging flame jet. Part I: Time-averaged results," *Int. J. Heat Mass Transf.*, vol. 48, no. 7, pp. 1236 – 1251, 2005.

[102] S. Tuttle, B. Webb, and M. McQuay, "Convective heat transfer from a partially premixed impinging flame jet. Part II: Time-resolved results," *Int. J. Heat Mass Transf.*, vol. 48, no. 7, pp. 1252 – 1266, 2005.

[103] V. C. Raj, P. Kuntikana, S. Sreedhara, and S. Prabhu, "Separation of heat transfer components from impinging methane diffusion flames," *Int. J. Heat Mass Transf.*, vol. 126, pp. 123 – 138, 2018.

[104] V. C. Raj, P. Kuntikana, S. Sreedhara, and S. Prabhu, "Heat transfer characteristics of impinging methane diffusion and partially premixed flames," *Int. J. Heat Mass Transf.*, vol. 129, pp. 873 – 893, 2019.

[105] W.-D. Hsieh and T.-H. Lin, "Methane flame stability in a jet impinging onto a wall," *Energy Convers. Manag.*, vol. 46, no. 5, pp. 727 – 739, 2005.

[106] S.-S. Hou and Y.-C. Ko, "Influence of oblique angle and heating height on flame structure, temperature field and efficiency of an impinging laminar jet flame," *Energy Convers. Manag.*, vol. 46, no. 6, pp. 941 – 958, 2005.

[107] P. Kuntikana and S. Prabhu, "Heat transfer characteristics of premixed methane–air flame jet impinging obliquely onto a flat surface," *Int. J. Heat Mass Transf.*, vol. 101, pp. 133 – 146, 2016.

[108] A. R. Tajik, P. Kuntikana, S. V. Prabhu, and V. Hindasageri, "Effect of preheated mixture on heat transfer characteristics of impinging methane–air premixed flame jet," *Int. J. Heat Mass Transf.*, vol. 86, pp. 550 – 562, 2015.

[109] C. Saha, R. Ganguly, and A. Datta, "Heat Transfer and Emission Characteristics of Impinging Rich Methane and Ethylene Jet Flames," *Exp. Heat Transf.*, vol. 21, no. 3, pp. 169 – 187, 2008.

[110] A. Singh, M. Mann, T. Kissel, J. Brübach, and A. Dreizler, "Simultaneous Measurements of Temperature and CO Concentration in Stagnation Stabilized Flames," *Flow Turbul. Combust.*, vol. 90, pp. 723–739, Jun 2013.

[111] M. Mann, C. Jainski, M. Euler, B. Böhm, and A. Dreizler, "Transient flame–wall interactions: Experimental analysis using spectroscopic temperature and CO concentration measurements," *Combust. Flame*, vol. 161, no. 9, pp. 2371 – 2386, 2014.

[112] Y.-C. Chien, D. Escofet-Martin, and D. Dunn-Rankin, "CO emission from an impinging non-premixed flame," *Combust. Flame*, vol. 174, pp. 16 – 24, 2016.

[113] H. Li, H. Zhen, C. Leung, and C. Cheung, "Effects of plate temperature on heat transfer and emissions of impinging flames," *Int. J. Heat Mass Transf.*, vol. 53, no. 19, pp. 4176 – 4184, 2010.

[114] H. Li, H. Zhen, C. Leung, and C. Cheung, "Nozzle effect on heat transfer and CO emission of impinging premixed flames," *Int. J. Heat Mass Transf.*, vol. 54, no. 1, pp. 625 – 635, 2011.

[115] D. Mishra, "Emission studies of impinging premixed flames," *Fuel*, vol. 83, no. 13, pp. 1743 – 1748, 2004.

[116] F. E. Jørgensen, "Uncertainty of CTA measurements," in *How to measure turbulence with hot-wire anemometers - a practical guide* (F. E. Jørgensen, ed.), pp. 40–44, Dantec Dynamics, 2002.

[117] C. Shaddix, "Correcting thermocouple measurements for radiation loss: A critical review," in *33rd National Heat Transfer Conference NHTC'99, Albuquerque, NM (US), 08/15 - 08/17*, pp. 1–10, 7 1999.

[118] M. P. Remacha, S. Jiménez, and J. Ballester, "Devolatilization of millimeter-sized biomass particles at high temperatures and heating rates. Part 1: Experimental methods and results," *Fuel*, vol. 234, pp. 757 – 769, 2018.

[119] F. R. Menter, R. B. Langtry, S. R. Likki, Y. B. Suzen, P. G. Huang, and S. Völker, "A Correlation-Based Transition Model Using Local Variables—Part I: Model Formulation," *J. Turbomach.*, vol. 128, pp. 413–422, 03 2004.

[120] F. R. Menter, R. Langtry, and S. Völker, "Transition Modelling for General Purpose CFD Codes," *Flow Turbul. Combust.*, vol. 77, pp. 277–303, Nov 2006.

[121] S. R. Mathur and J. Y. Murthy, "Coupled Ordinates Method for Multigrid Acceleration of Radiation Calculations," *J. Thermophys. Heat Transf.*, vol. 13, no. 4, pp. 467–473, 1999.

[122] J. Hameury, B. Hay, and J. R. Filtz, "Measurement of Total Hemispherical Emissivity Using a Calorimetric Technique," *Int. J. Thermophys.*, vol. 28, pp. 1607 – 1620, Oct 2007.

[123] S. B. Pope, *Turbulent Flows*. Cambridge University Press, 2000.

[124] J. Warnatz, "Rate coefficients in the C=H=O system," in *Combustion Chemistry* (Gardiner, W.C. Jr., ed.), pp. 197 – 360, Springer-Verlag, NY, 1984.

[125] T. Poinsot and D. Veynante, *Theoretical and Numerical Combustion: Second Edition*. Edwards, 2005.

[126] J. Warnatz, U. Maas, and R. Dibble, *Combustion: Physical and Chemical Fundamentals, Modeling and Simulation, Experiments, Pollutant Formation*. Springer-Verlag Berlin Heidelberg, 2006.